

Terahertz time-domain spectroscopy of carrier trapping in semiconductors

James Lloyd-Hughes

Department of Physics, University of Oxford.



Thesis submitted for the Degree of Doctor of Philosophy, in Trinity Term 2006.

Abstract

An investigation into the dynamics of charge carriers in a diverse range of semiconductors is reported, which utilised time-domain spectroscopy techniques in the terahertz (far-infrared) region of the electromagnetic spectrum.

Materials suitable for ultra-fast optoelectronic devices were examined by optical-pump terahertz-probe spectroscopy, and additionally using terahertz emission spectroscopy. The time-resolved conductivity of electrons in a semiconductor following photoexcitation exhibited a dynamical change that was described by the trapping of electrons on ultra-short (picosecond) timescales, and by diffusion on longer timescales. Sub-picosecond electron lifetimes (in semiconductor crystals damaged by bombardment with highly energetic ions) were observed to result in greater emitted terahertz power at high frequencies, a result that was reproduced quantitatively by a carrier dynamics simulation. In semi-insulating gallium arsenide, an increased electronic conductivity and terahertz emission were obtained by passivating the surface defect states. Electrons were observed to have lifetimes exceeding the period of high repetition rate lasers, somewhat limiting the generated terahertz power.

Furthermore, terahertz time-domain spectroscopy was used to monitor the trapping of holes in transistor devices made from semiconducting polymers, an effect that currently limits the commercial application of polymer electronic devices. A build-up of hole density was seen in the transistor's conductive channel on timescales of tens of minutes. The thermal removal of these trapped holes, and the influence of illumination by photons with above bandgap energy, was studied.

Publications

The following is a list of the publications, both published and in press, to which I have contributed during my DPhil, in chronological order.

1. **J. Lloyd-Hughes**, E. Castro-Camus, M. D. Fraser, C. Jagadish, and M. B. Johnston. *Carrier dynamics in ion-implanted GaAs studied by simulation and observation of terahertz emission*. Phys. Rev. B, **70** 235330, December 2004.
2. E. Castro-Camus, **J. Lloyd-Hughes**, and M. B. Johnston. *Three-dimensional carrier-dynamics simulation of terahertz emission from photoconductive switches*. Phys. Rev. B, **71** 195301, May 2005.
3. E. Castro-Camus, **J. Lloyd-Hughes**, M. B. Johnston, M. D. Fraser, H. H. Tan, and C. Jagadish. *Polarization-sensitive terahertz detection by multicontact photoconductive receivers*. Appl. Phys. Lett., **86** 254102, June 2005.
4. **J. Lloyd-Hughes**, E. Castro-Camus, M. D. Fraser, H. H. Tan, C. Jagadish, and M. B. Johnston. *Broadband terahertz emission from ion-implanted semiconductors*. To appear in Springer Proceedings in Physics (Proceedings of the 14th International Conference on Nonequilibrium Carrier Dynamics in Semiconductors), July 2005.
5. **J. Lloyd-Hughes**, E. Castro-Camus, and M. B. Johnston. *Simulation and optimisation of terahertz emission from InGaAs and InP photoconductive switches*. Sol. Stat. Comm., **136** 595, December 2005.
6. **J. Lloyd-Hughes**, E. Castro-Camus, M. D. Fraser, H. H. Tan, C. Jagadish, and M. B. Johnston. *Carrier dynamics in ion-implanted semiconductors studied by simulation and observation of terahertz emission*. Proc. SPIE **6118** 61180K, February 2006.
7. E. Castro-Camus, **J. Lloyd-Hughes**, M. D. Fraser, H. H. Tan, C. Jagadish, and M. B. Johnston. *Detecting the full polarization state of terahertz transients*. Proc. SPIE **6120** 61200Q, February 2006.
8. **J. Lloyd-Hughes**, T. Richards, H. Sirringhaus, E. Castro-Camus, L. M. Herz, and M. B. Johnston. *Charge trapping in polymer transistors probed by terahertz spectroscopy and scanning probe potentiometry*. Applied Physics Letters **89** 112101, September 2006.

9. G. Doucas, V. Blackmore, B. Ottewell, C. Perry, P. G. Huggard, **J. Lloyd-Hughes**, E. Castro-Camus, M.B. Johnston, M.F. Kimmitt, B. Redlich, and A. van der Meer. *Longitudinal electron bunch profile diagnostics at 45-50meV using coherent Smith-Purcell radiation*. Physical Review Special Topics: Accelerators and Beams **9** 092801, September 2006.
10. **J. Lloyd-Hughes**, S.K.E. Merchant, L. Fu, H. H. Tan, C. Jagadish, E. Castro-Camus, and M.B. Johnston. *Influence of surface passivation on ultrafast carrier dynamics and terahertz radiation generation in GaAs*. Submitted to Applied Physics Letters, 2006.
11. P.C. Upadhyay, W.H. Fan, A. Burnett, J. Cunningham, A.G. Davies, E. H. Linfield, **J. Lloyd-Hughes**, E. Castro-Camus, M. B. Johnston, and H. Beere. *Optimization of broadband terahertz (>6.0 THz) generation in asymmetrically-excited photoconductive antenna structures*. Submitted to Applied Physics Letters, 2006.

The following is a list of the conference talks and posters to which I have contributed, in reverse chronological order. The * denotes the presenter.

1. “*THz Emitters and Detectors Based on Ion Implanted III-V Semiconductors*” [Keynote Talk]. **J. Lloyd-Hughes**, E. Castro-Camus, S. Merchant, M. B. Johnston*; IRMMW-THz 2006, 18-22th September 2006, Shanghai, China.
2. “*Polymer Transistor Performance Monitored by Terahertz Spectroscopy*” [Talk]. **J. Lloyd-Hughes**, T. Richards, E. Castro-Camus, H. Sirringhaus, L. M. Herz, and M. B. Johnston*; IRMMW-THz 2006, 18-22th September 2006, Shanghai, China.
3. “*Probing the Electronic Properties of Organic Transistors with Terahertz Time-Domain Spectroscopy*” [Poster]. **J. Lloyd-Hughes**, T. Richards, E. Castro-Camus, H. Sirringhaus, L. M. Herz, and M. B. Johnston*; Gordon Research Conference on Electronic Processes in Organic Materials, 30 July - 4 August 2006, South Hadley, MA, USA.
4. “*Terahertz emission and lifetime measurements of ion-implanted semiconductors: experiment and simulation*” [Poster]. **J. Lloyd-Hughes**, E. Castro-Camus*, M.D. Fraser, L. Fu, H.H. Tan, C. Jagadish and M.B. Johnston; CLEO 2006, Los Angeles, USA, 21-26th May 2006.
5. “*Polarisation sensitive terahertz time-domain spectroscopy*” [Talk]. E. Castro-Camus*, **J. Lloyd-Hughes**, M.D. Fraser, L. Fu, H.H. Tan, C. Jagadish and M.B. Johnston; CLEO 2006, Los Angeles, USA, 21-26th May 2006.
6. “*Detecting the full polarisation state of terahertz transients*” [Invited Talk]. E. Castro-Camus, **J. Lloyd-Hughes***, M.D. Fraser, L. Fu, H.H. Tan, C. Jagadish and M.B. Johnston; Photonics West 2006, San Jose, USA, 20-26th January 2006.

7. “*Carrier dynamics in ion-implanted semiconductors studied by simulation and observation of terahertz emission*” [Invited Talk]. **J. Lloyd-Hughes***, E. Castro-Camus, M.D. Fraser, H.H. Tan, C. Jagadish and M.B. Johnston; Photonics West 2006, San Jose, California, 20-26th January 2006.
8. “*Broadband terahertz emission from ion-implanted semiconductors*” [Talk]. **J. Lloyd-Hughes***, E. Castro-Camus, M.D. Fraser, H.H. Tan, C. Jagadish and M.B. Johnston; 14th International Conference on Nonequilibrium Carrier Dynamics in Semiconductors (HCIS-14), Chicago, 24-29th July 2005.
9. “*Simulated terahertz emission from defect-laden semiconductors*” [Poster]. **J. Lloyd-Hughes***, E. Castro-Camus and M.B. Johnston; Physics 2005, Warwick, 10th-14th April 2005.
10. “*Terahertz emission from ion-implanted GaAs surfaces*” [Talk]. **J. Lloyd-Hughes***, E. Castro-Camus, M.D. Fraser, C. Jagadish and M.B. Johnston; EQUONT-3, Cambridge, 19th-23rd September 2004.
11. “*Carrier dynamics in ion-implanted GaAs studied by simulation and observation of terahertz emission*” [Talk]. **J. Lloyd-Hughes***, E. Castro-Camus, M.D. Fraser, C. Jagadish and M.B. Johnston; Basic Technology Meeting, UMIST, 15th September 2004.

Acknowledgements

I would like to thank a large range of people for their advice and support during my PhD. Principally, I gratefully thank my supervisor, Dr. Michael B. Johnston, for his invaluable guidance and enthusiastic instruction throughout the last three years. Additionally, I am indebted to my fellow group members and office-mates Enrique Castro-Camus, Suzannah Merchant, Patrick Parkinson and Ming-Hua Chang. I'd also like to express my gratitude to all the technical and support staff in the Clarendon (in particular Rob, George, Peter, Alan, Reg, Bill and John), and Paul and Darren in the Photofabrication Unit. I'd like to thank my family and friends for their fantastic support, encouragement, patience and general good banter! Finally, I'd like to acknowledge financial support from the EPSRC for a Department Training Award grant, and Jesus College for a Graduate Scholarship.

While the majority of the work reported throughout this thesis is my own, I would like to formally acknowledge the following collaborative undertakings. Firstly, the ion-implanted semiconductors investigated throughout Chapters 3 and 4 were created in the group of Prof. Chenupatti Jagadish, at the Department of Electronic Materials Engineering, part of the Australian National University, in Canberra. I am exceedingly grateful for the advice, samples and suggestions provided by Prof. Jagadish and a number of colleagues at ANU, including Dr. Lan Fu, Dr. Michael D. Fraser and Dr. H. Hoe Tan.

The waveguide array plates used as THz filters (Section 2.4.4) were provided by, and characterised for, the group of Dr. George Doucas (Sub-department of Particle Physics, University of Oxford). The measurements were taken with Victoria Blackmore, who I'd also like to thank for referring me to papers discussing the design of waveguide array plates.

The low-temperature grown GaAs samples (Section 3.4 and 4.5) were grown by two different groups: that of Prof. Mo Missous (University of Manchester), and that of Prof. Edmund H. Linfield (University of Leeds). I'd also like to thank Prof. Linfield for supplying the 0.2 mm-thick GaP electro-optic crystal used in Chapter 4. Further, I am grateful to Dr. Prashanth Upadhyा (University of Leeds) for an informative collaboration regarding the pump-fluence dependence of broadband terahertz emission.

The polymer field-effect transistor work (Chapter 5) was undertaken in collaboration with the Organic Semiconductors group of Dr. Laura M. Herz, also in the Clarendon Laboratory, and with the group of Prof. Henning Sirringhaus in the Optoelectronics Group at the Cavendish Laboratory, University of Cambridge. Tim Richards (Optoelectronics, Cambridge) fabricated the polymer transistors, supplied the I-V data in Figure 5.2b, and provided the scanning-probe potentiometry data of Figure 5.4.

Contents

1	Introduction	1
1.1	Terahertz radiation	1
1.2	Broadband terahertz spectroscopy	3
1.3	Applications of terahertz spectroscopy	4
1.3.1	A plethora of quasiparticles	5
1.3.2	Ultra-fast phenomena: Within a billionth of a blink	7
1.3.3	Internal imaging	10
1.3.4	Review articles	11
1.4	Overview of this thesis	11
2	Terahertz time-domain spectroscopy	14
2.1	Introduction	14
2.1.1	Principles of time-domain spectroscopy	15
2.2	Setup of THz-TDS experiment	16
2.2.1	Femtosecond lasers	17
2.2.2	Photoconductive generation of terahertz radiation	19
2.2.3	Electro-optic detection	21
2.2.4	Spectral resolution and bandwidth	23
2.3	Complex refractive index of a thick sample	25
2.3.1	Analytical expression for the complex refractive index	26
2.3.2	Dispersion relations	26
2.4	Examples of THz-TDS	27
2.4.1	Phonon-polariton dispersion	27
2.4.2	Rotational modes of water vapour	30
2.4.3	Free electron plasmas	33
2.4.4	Transmission through metallic waveguides	36
2.5	Summary	37
3	Carrier dynamics in damaged inorganic semiconductors	40
3.1	Ultrafast optoelectronics	40
3.1.1	Semi-insulating direct bandgap semiconductors	41
3.1.2	Low-temperature growth	42
3.1.3	Ion-implantation	43

3.1.4	Shockley-Read-Hall lifetime model	45
3.2	Time-resolved conductivity	46
3.2.1	Experimental setup	46
3.2.2	Calculating the conductivity	48
3.2.3	Comparison with other time-resolved techniques	51
3.3	Semi-insulating semiconductors	54
3.3.1	Photoexcitation dynamics	54
3.3.2	Surface states and diffusion	57
3.3.3	Temperature dependance of mobility	60
3.4	Low-temperature-grown GaAs	63
3.5	Ion-implanted InP	65
3.5.1	Activation energy for annealing traps	67
3.5.2	Defect concentration	67
3.5.3	Applicability of Shockley-Read-Hall model	68
3.6	Summary	70
4	Broadband generation of terahertz radiation	72
4.1	Overview	72
4.2	Modelling photoconductive THz emission	73
4.2.1	Phenomenological approach	73
4.2.2	Carrier dynamics simulation	75
4.3	THz radiation from semiconductor surfaces	77
4.4	Emission from ion-implanted semiconductors	82
4.4.1	Measured surface field terahertz emission	83
4.4.2	Scattering from neutral impurities	84
4.4.3	Carrier trapping at defects	88
4.4.4	Comparison of experiment and simulation	89
4.5	Long-lived carriers limit THz emission	92
4.6	Enhanced emission from passivated surfaces	98
4.6.1	Surface emitters	98
4.6.2	Photoconductive switches	100
4.7	Summary	100
5	Charge trapping in polymer transistors	102
5.1	Introduction	102
5.1.1	Semiconducting polymers	104
5.1.2	Polymer field-effect transistors	107
5.1.3	Trapping in polymer transistors	110
5.1.4	Scanning-probe potentiometry	113
5.2	Terahertz charge modulation spectroscopy	115
5.2.1	Setup of experiment	115
5.2.2	Measured THz transmission change	116
5.3	Modelling the THz transmission change	119

5.4	Hole trapping in the accumulation layer	122
5.5	Removal of trapped holes	125
5.5.1	Thermal detrapping	126
5.5.2	Above absorption-edge illumination	127
5.6	Dielectric breakdown of transistor	130
5.7	Summary	132
6	Conclusion	134
6.1	Future prospects	136
A	Electromagnetism	138
A.1	Linear electromagnetism	138
A.2	Charge density in an accumulation layer	140
Bibliography		143
Symbols		156

Chapter 1

Introduction

“Colours are not Qualifications of Light, derived from Refractions, or Reflections of natural Bodies (as ‘tis generally believed), but Original and connate properties, which in divers Rays are divers. Some Rays are disposed to exhibit a red colour and no other; some a yellow and no other, some a green and no other, and so of the rest.”

Isaac Newton, *Philosophical Transactions of the Royal Society*, 19 Feb. 1671.

1.1 Terahertz radiation

Our understanding of the interaction between light and matter has undergone numerous revolutions throughout the modern age, from Newton’s classical ray optics and Maxwell’s electromagnetism to the current quantum description. The development of new sources of electromagnetic radiation has provided much of the stimulus for progress: Tesla and Marconi’s early radios, Röntgen’s X-ray generator and Maiman’s laser have led to significant physical discoveries and new technology. Yet the vast majority of experiments and devices that employ electromagnetic radiation at frequencies above the microwave range, however, measure solely the intensity of light. In the last few decades it has become possible to determine directly the electric field of a pulse of electromagnetic radiation, via *time-domain spectroscopy* techniques. This addition

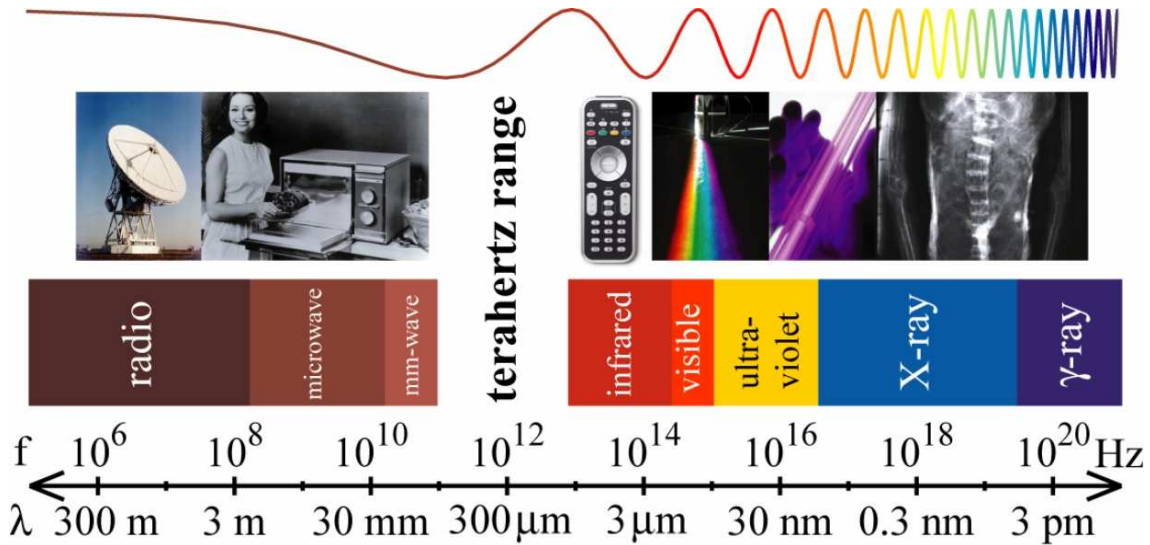


Figure 1.1: The electromagnetic spectrum, from radio waves to γ -rays. The terahertz (THz) range sits between microwave and infrared frequencies. ($1 \text{ THz} = 10^{12} \text{ Hz}$ in frequency, 0.3 mm in wavelength, 33 cm^{-1} wavenumbers, or 4.1 meV in energy).

to the experimenter’s toolkit is now providing invaluable insights into diverse aspects of the light-matter interaction, in a range of the electromagnetic spectrum that was previously little explored: the terahertz (THz) range ($1 \text{ THz} = 10^{12} \text{ Hz}$ in frequency, 0.3 mm in wavelength, 33 cm^{-1} wavenumbers, or 4.1 meV in energy).

Terahertz, or far-infrared, radiation is bordered by the microwave and infrared ranges of the electromagnetic spectrum, and spans the regime $0.1 - 10 \text{ THz}$, as Figure 1.1 illustrates. It has long been a challenge to produce and detect electromagnetic radiation at frequencies in the THz range[1]: high speed electronic devices can typically reach only as high as 100 GHz , while solid state sources based on electronic transitions in semiconductors lie at higher frequencies, descending down as far as the mid-infrared ($30 - 120 \text{ THz}$). Recent years have seen significant progress in the development of devices that can produce radiation at discrete frequencies in the THz range, including quantum cascade lasers, [2] Schottky diode multiplier chains, [3] molecular

gas lasers, [4] and p-type germanium lasers [5]. The detection of THz radiation was a major challenge for a long time: THz radiation lies in the noise background at room temperature, where thermal energies are of the order of $k_B T = 25.5 \text{ meV} = 6.2 \text{ THz}$. Cryogenically cooled bolometers can detect the intensity of THz radiation [6], but remain expensive to operate. In order to determine properties of a material using THz radiation, sources and detectors of THz radiation are required to operate over a broad range of frequencies, with a high sensitivity. This is achievable using time-domain spectroscopic techniques, which are outlined in Section 1.2, below. The remainder of this chapter consists of an overview of recent applications of terahertz time-domain spectroscopy (THz-TDS) within condensed matter physics, and beyond. Finally, an overview of this thesis, in which THz-TDS is utilised to investigate the trapping of charge carriers in semiconductors, is given in Section 1.4.

1.2 Broadband terahertz spectroscopy

In THz-TDS, pulses of electromagnetic radiation with durations of 1 ps (10^{-12} s) or less are generated and detected. These transients contain as few as one single cycle of the electric field, and therefore have frequency components over a broad range: either the THz or the mid-infrared regimes can be covered in their entirety, depending on the choice of emitter [7; 8]. In time-domain techniques the electric field of a pulse (rather than its intensity) is recorded as a function of its arrival time. The photoconductive generation of terahertz radiation, the principal method examined in this thesis, is described in detail in Section 2.2.2. Detecting the arrival time of an electric field pulse after it has interacted with a sample allows both the refractive index and absorption

coefficient (or equivalently the electrical conductivity) to be determined directly from experiment. This is not possible with traditional spectroscopic methods that measure the intensity of light, as discussed in Section 2.1.1. The wealth of studies that can be undertaken with THz-TDS is outlined in Section 1.3.

An additional advantage of working with pulses of electromagnetic radiation is that studies of materials on short timescales can be readily undertaken. For instance, a pulse of light can be used to trigger a process in a sample, such as the creation of charge carriers in a semiconductor. The frequency-dependent conductivity of a material can then be probed by a THz pulse, and tracked as a function of the arrival time of this ‘pump’ (trigger) pulse relative to the THz pulse. This technique, referred to as optical-pump THz-probe spectroscopy,¹ is exploited throughout Chapter 3, and has been used to investigate charge transport in a number of materials of contemporary scientific interest (Section 1.3.2).

1.3 Applications of terahertz spectroscopy

In order to place the research presented in this thesis in a broader context a few recent studies are reviewed here, beginning with applications of THz-TDS in solid state physics (Sections 1.3.1 and 1.3.2). Industrial applications of THz imaging are discussed subsequently in Section 1.3.3.

¹Sometimes called time-resolved THz spectroscopy [9], although this name is confusing since it can be interpreted as meaning the same as THz-TDS.

1.3.1 A plethora of quasiparticles

One of the intriguing aspects of contemporary condensed matter physics is that an accurate model of a material can often be obtained by ignoring the vast majority of its constituent particles, and treating the system as consisting of a few *quasiparticles*. These pseudo-particles have properties that differ only slightly from their constituents: for instance electrons (strictly quasi-electrons) in a large bandgap III-V semiconductor behave similarly to electrons in vacuum, but with a reduced ('effective') mass. Terahertz-frequency photons are effective in spectroscopic studies of quasiparticles, as a large number have typical energies around 1-10 meV (0.24-2.4 THz). A diverse range of phenomena can be studied via THz transmission (or reflection) spectroscopy in the time-domain, as the (non-exhaustive) list below indicates. Optical-pump THz-probe experiments are particularly valuable, and further examples of this technique are given in Section 1.3.2.

- *Electrons and holes* ('free carriers'). These can be injected thermally, electrically or by a photon exciting an electron (from the valence band to the conduction band in an inorganic semiconductor; from the HOMO to the LUMO level in an organic semiconductor). The response of electrons and holes to THz radiation can often be described as a plasma, with a peak in the conductivity at zero frequency (Section 2.4.3). An early use of THz-TDS was to investigate free carriers in doped semiconductors such as silicon [10] and GaAs [11], and subsequently it has been applied to the doped polymers [12] and MEH-PPV [13], and mixes of metallic and semiconducting carbon nanotubes [14; 15; 16].
- *Polarons*. An electron or a hole distorts its surroundings: the effect of this can be

described as another quasiparticle – the polaron – with an altered effective mass. Polaronic effects have been investigated via THz-TDS of lead [17], in which the electron-phonon coupling constant was determined. Additionally, polarons in TiO_2 were shown to be intermediate in size between those in organic conductors (strongly bound, small polarons), and those of III-V semiconductors (weak, large polarons) [18].

- *Excitons* are electron-hole pairs, bound by the Coulomb interaction. A number of examples of excitonic effects investigated via THz-TDS are given in Section 1.3.2. Additionally, the stimulated emission of THz radiation at 1.6 THz has been demonstrated in the transition between the 3p and 2s excitonic levels of bulk Cu_2O [19].
- *Polaritons* are propagating electromagnetic modes (photons) coupled with another quasiparticle. Examples include the study of TO-phonon polaritons in ferroelectrics [20], in which both the lower and upper branches of the dispersion curve were observed. Surface plasmon polaritons, which propagate along semiconductor interfaces, have been studied by THz-TDS of patterned gratings made on silicon [21] and InSb [22]. Additionally, polaritons of different quasiparticles can interact: for instance coupled plasmon-phonon-polaritons have been investigated in InP [23].
- *Cooper pairs.* Electron-electron pairs in superconductors are bound by the electron-phonon interaction, and are referred to as Cooper pairs. In Section 1.3.2 a variety of studies of superconducting materials with THz-TDS are briefly reviewed.

Recent examples of insights into aspects of solid-state physics, which were obtained from time-resolved conductivity measurements using THz-TDS, are now given.

1.3.2 Ultra-fast phenomena: Within a billionth of a blink

The knowledge of how charge carriers move through electrically conductive materials is essential for the successful creation of electronic devices. There is a relentless demand for ever faster technology, and the knowledge of the fundamental physics of how charges behave in materials (particularly semiconductors) on ultra-short timescales ($< 100 \text{ ps}$) is key to achieving this. To put such minuscule durations in context, the duration of one blink of a human eyelid is roughly 100 ms , one hundred billion times longer than 1 ps ! The timescales of a number of phenomena in semiconductor physics are shown in Figure 1.2. Optical-pump THz-probe spectroscopy provides an ideal method to investigate the conductivity of charge carriers on picosecond timescales: a few

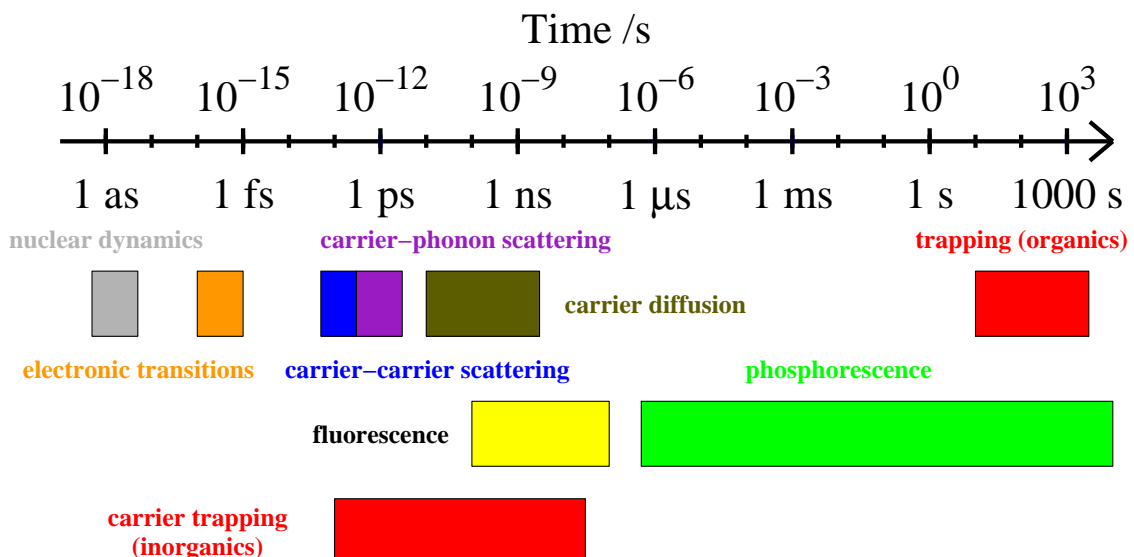


Figure 1.2: Timescales of various processes in semiconductor physics.

examples of its use are now discussed.

The formation of quasiparticles from an electron-hole plasma was observed for the first time, [24; 25] via optical-pump THz-probe spectroscopy with mid-infrared probe pulses. Collective phenomena such as Coulomb screening and scattering from an electron-hole plasma were found to arise after a time delay of the order of the inverse plasma frequency ($\sim 10^{-14}$ s). Before this time has elapsed a regime was observed in which the interaction between two point charges was described by the bare Coulomb potential only, as predicted by some quantum kinetic theories [26]. In a similar way the formation, relaxation and ionization of excitons in GaAs quantum wells have been studied [27], and it has been shown that a transient conducting state exists before the insulating (bound) excitonic state forms [28].

Terahertz spectroscopy has played an important role in characterising the properties of superconductors, which exhibit zero electrical resistance² below a critical temperature T_c . The measurement of the frequency-dependent complex conductivity $\sigma(\omega)$ of superconducting thin films at terahertz frequencies allows the non-contact determination of the superconducting energy gap 2Δ : for instance niobium has $2\Delta = 1.6$ meV [30], and for magnesium diboride $2\Delta \approx 5$ meV [31]. Additionally, $\sigma(\omega)$ can also provide information about the magnetic penetration depth, the surface impedance and the superfluid density [32]. Measuring the complex conductivity of YBCO, a high T_c superconductor, between 10 K and 120 K has revealed a peak in the real part of the conductivity $\mathbb{R}(\sigma)$ close to T_c (60 K), demonstrating that electron-electron (rather than electron-phonon) scattering dominates in cuprate superconductors [33]. Finally, time-resolved far-infrared studies have allowed the breaking and reformation of Cooper

²Strictly, the Meissner effect[29] – zero internal magnetic field – is a better criterion to identify superconductivity.

pairs to be tracked on picosecond timescales in lead [34], magnesium diboride [35] and $\text{Bi}_2\text{Sr}_2\text{CaCuO}_{8+\delta}$ [36].

The time-resolved conductivity measurements obtained from optical-pump THz-probe spectroscopy are also providing insights into charge transport in organic semiconductors, materials that could usher in a new age of flexible, printable electronics. Complex conductivity measurements of the semiconducting polymer MEH-PPV have enabled the relative fraction of excitons and free charge carriers to be determined following photoexcitation [37; 38]. Similar experiments carried out at low temperatures have revealed that electronic transport in pentacene crystals is band-like on picosecond timescales [39; 40; 41]: a decrease in the carrier mobility was observed with increasing temperature, similar to that observed in inorganic semiconductors, rather than exhibiting the increase typical of organic semiconductors (Section 5.1.1).

Broadband THz radiation is finding increasing application in determining the carrier dynamics of nano-scale and nano-structured materials. This is despite the relatively long wavelength ($\sim 300 \mu\text{m}$) of THz radiation in comparison with the typical dimensions of structures. Recently, the influence on photo-conductivity of quantum dots – three-dimensional quantum wells, created by a small volume of a semiconductor within a matrix of a different material – has been studied, for quantum dots made from InP [42], silicon [43] and CdSe [44; 45], for InGaAs quantum dot chains [46], and for ErAs nanoislands in GaAs [47]. Additionally, the dynamics of photoexcited carriers in a mixture of metallic and semiconducting single-walled carbon nanotubes was shown to be described by a combined Drude and Lorentz dielectric function [48].

1.3.3 Internal imaging

THz-TDS can be used to obtain images of objects in the far-infrared spectral range, most simply by translating the sample within a spectrometer and recording the transmitted electric field at each position. Imaging at THz frequencies presents a number of unique opportunities, with applications frequently cited in medical and security imaging. THz-TDS provides a way to image the interior of biological objects, which often cannot be done by any other non-destructive means. Demonstrative examples include imaging cavities in teeth [49], resolving the interior structure of sunflower seeds [50], the detection of skin cancer [51] and measurements of the depth of burned skin [52]. By recording the temporal structure of THz waveforms, three-dimensional images of objects containing regions of different refractive index can be formed [53]. Further potential applications include semiconductor quality control and package inspection.

Because terahertz radiation has a relatively long wavelength ($1\text{ THz} = 300\text{ }\mu\text{m}$) it might be thought that diffraction limits the spatial resolution of THz imaging systems to these length scales. However, ideas from near-field scanning optical microscopy can be applied to THz imaging, enabling sub-wavelength resolutions to be achieved [54; 55]. Indeed, the detection of the THz pulse reflected from a tungsten tip placed close to a sample has allowed a resolution of 150nm to be attained [56]. Such THz microscopy studies are already of value in the non-contact characterisation of electronic devices, for instance in probing the low concentrations of electrons within surface depletion layers [57].

1.3.4 Review articles

The large quantity of experimental work in the field of THz-TDS means that the summary above is far from exhaustive. The interested reader is therefore referred to the following reviews of THz-TDS and its applications. Nuss and Orenstein's 1998 review [33] provides useful background reading on THz pulse generation and detection using photoconductive switches, and gives a good summary of the uses of THz-TDS systems up until the end of the last millennium. The following four papers are more current: generating THz pulses via optical rectification is covered by Shan, Nahata and Heinz's review [58]; Schmuttenmaer's article [9] contains a comprehensive synopsis of THz emission and optical-pump THz-probe spectroscopy; Tani, Herrman and Sakai's paper [59] discusses imaging applications; and Beard, Turner and Schmuttenmaer's 2002 review [60] details far-infrared absorption and refractive index measurements of neat liquids as well as time-resolved studies of transient photoconductivity in both GaAs and low-temperature-grown GaAs.

1.4 Overview of this thesis

The overarching theme of this thesis is the investigation of the trapping of charge carriers in semiconductors, via spectroscopy in the terahertz frequency range. After the creation of a conducting electron within a semiconductor, by absorbing a photon of light or by electrical injection, it can move only for a finite time before becoming immobile or being destroyed (recombining). Mobile charge carriers change the conductivity of a material, thus altering the amount of terahertz radiation that can be transmitted through it. Obtaining information about how quickly charge carriers are

trapped is vital to understand electrical transport in semiconductors, materials which act as the foundation of modern electronic technology.

The principles and advantages of terahertz time-domain spectroscopy are considered in detail in Chapter 2. The extraction of the complex refractive index of a sample from time-domain data is outlined, and several experimental studies of spectroscopic features are reported, including the response of phonon-polaritons and free electron plasmas at THz frequencies. These results form a basis for much of the work reported later in this thesis.

In Chapter 3 the technique of optical-pump, THz-transient spectroscopy is introduced. The dynamics of the rise and decay in the conductivity of a photoexcited electron distribution are presented, and related to theory, for a variety of III-V semiconductors. Subsequently, the transient conductivity of ion-implanted and low-temperature-grown semiconductors is discussed: these materials are suitable for optoelectronic devices that operate on ultra-short timescales, since the electronic lifetime can be tailored to anywhere in the range from a few nanoseconds to less than a picosecond.

The carrier dynamics information gleaned from optical-pump THz-probe spectroscopy is employed during Chapter 4, in which a more complete description of THz emission from photoexcited semiconductors is given. A simple phenomenological model of THz emission is examined, before the use of a carrier dynamics simulation, which has greater predictive power, is introduced. Afterwards, a combined experimental and modelling approach is adopted to investigate carrier scattering and trapping in defect-laden semiconductors, such as ion-implanted GaAs and InP. Similarly, the influence of the passivation of surface defect states on THz emission is studied.

Departing from phenomena that occur on ultra-short timescales in inorganic semiconductors, Chapter 5 reports an investigation into the trapping of holes in polymer transistors (pFETs) using THz spectroscopy, which typically takes many minutes to occur. The influence of a change in charge density in the silicon gate on the THz radiation transmitted through a pFET is used to monitor the trapping of holes in the device's accumulation layer. This is a direct observation of an effect that substantially limits the long-term performance of pFETs, which are key components of a new breed of flexible electronic devices, such as displays and computers, made from polymers.

Chapter 2

Terahertz time-domain spectroscopy

“May it not be that every one of the infinitely small vibrations, striking common matter with a certain force, enters its substance, is held there by attraction, and augmented by succeeding vibrations, till the matter has received as much as their force can drive into it?”

Benjamin Franklin, *A Theory of Light and Heat*, 1784.

2.1 Introduction

The electromagnetic force is perhaps the best understood of the four fundamental physical forces, and is certainly the most widely exploited in modern society. How matter interacts with photons of light, for instance in coupling to the vibrations of a crystal, has provided numerous technological and scientific breakthroughs. In this chapter terahertz time-domain spectroscopy (THz-TDS) is introduced, a highly sensitive technique that can produce and detect light across the terahertz range. A discussion of the experimental generation and detection of pulsed THz radiation is given in Section 2.1. (A more detailed description of photoconductive THz emission is reserved until Chapter 4). The methods of extracting the complex refractive index of a sample are outlined (Section 2.3), and subsequently experimental examples

are presented of the use of THz-TDS in determining the properties of quasiparticles in semiconductors, and the interaction between THz radiation and metallic waveguide arrays (Section 2.4). First, however, the distinction between time-domain spectroscopy and traditional techniques that measure the intensity of light is explored.

2.1.1 Principles of time-domain spectroscopy

In conventional spectroscopy the mean intensity of electromagnetic radiation transmitted through or reflected from a sample is measured. The power density of an electromagnetic wave is given by its Poynting vector $\mathbf{I} = (\mathbf{E} \times \mathbf{H}^*)/2$. The electric field of a transverse plane wave propagating through a medium in the z direction is $\mathbf{E}(z, t) = \mathbf{E}_0 e^{i(kz - \omega t)}$, with a similar expression for the magnetic field (Appendix A.1 contains a definition of the various symbols). The mean intensity of the radiation is $I(\omega) \propto |\mathbf{E}_0|^2$, and therefore the full complex refractive index $\tilde{n} = n + i\kappa$ cannot be directly obtained from a measurement of the intensity only, as the time-dependence – the phase – of \mathbf{E} is lost. Traditionally, this problem is avoided via the Kramers-Kronig relations [61], which allow the real part of the refractive index n to be calculated from the imaginary part κ via:

$$n(\omega) = 1 + \frac{1}{\pi} P \int_{-\infty}^{+\infty} \frac{\kappa(\omega')}{\omega' - \omega} d\omega' \quad (2.1)$$

where the symbol P denotes the principal value of the contour integral. A similar expression allows one to calculate κ from n . The Kramers-Kronig relations assume knowledge of n or κ over a large frequency range, and become more unwieldy if spatial dispersion (a non-local response) is introduced [61].

Time-domain spectroscopy techniques circumvent the Kramers-Kronig relations, by

directly extracting $\tilde{n}(\omega)$ over a broad frequency range. This is achieved by measuring the electric field amplitude of a pulse of electromagnetic radiation as a function of its arrival time (phase).

2.2 Setup of THz-TDS experiment

The time-domain spectroscopy setup used throughout this work is shown in Figure 2.1, and is now described in overview, before a detailed description of the various components is given in Sections 2.2.1-2.2.3. A beam of ultrashort infrared pulses (<1 ps in duration) from a mode-locked laser (Section 2.2.1) was split into beam P1, used to generate a THz pulse (Section 2.2.2), and beam P3, used to detect the THz pulse (Section 2.2.3). P1 was incident on a THz source, typically a semiconductor crystal, and produced a pulse of THz radiation with an electric field as shown schematically in the inset to Figure 2.1. The emitted THz radiation was collected, collimated and focused onto a sample by a pair of off-axis parabolic mirrors. (The first parabolic mirror can be placed either in the ‘transmission’ geometry, as shown here, or alternatively P1 can be shone through a hole in the mirror and the ‘reflection’ geometry THz radiation collected [7], as the inset in Figure 2.1 illustrates). The electric field transmitted through the sample was collected by a second pair of parabolic mirrors, and focussed onto a THz detector. Temporal resolution was achieved by recording the THz electric field only during some time window, when the detector was switched on by a pulse in beam P3. The relative arrival time of the THz pulses generated by beam P1 and the detection beam P3 was altered by moving delay stage 1, allowing the electric field of the THz pulse to be recorded as a function of its arrival time. The com-

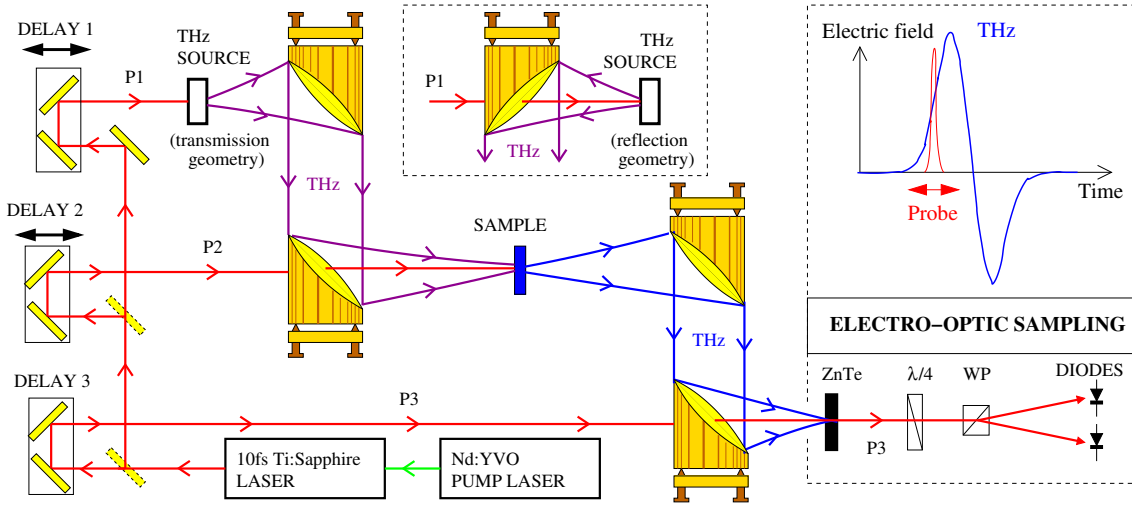


Figure 2.1: Schematic of the THz-TDS setup used in this work. Mirrors are represented by solid yellow boxes, and beam-splitters by dotted yellow boxes. Infrared pulses from a femtosecond laser (red lines) were incident on a THz source (beam P1). The THz radiation emitted (purple lines) was collected and focussed onto a sample by a pair of parabolic mirrors. The transmitted THz beam (blue) was focussed onto a ZnTe crystal, and altered the polarisation of probe beam P3 when they coincided temporally. Beam P2 was optionally used to photoexcite carriers in the sample.

plex refractive index (and conductivity) of the sample over the THz frequency range was extracted by comparing the electric fields recorded with and without the sample present (Section 2.3). An additional beam P2, split off from P1, was optionally used to photoexcite carriers in the sample, in order to examine the dynamical behaviour of their conductivity (via optical-pump THz-probe experiments, Section 3). To remove the influence of atmospheric water vapour, which can absorb THz radiation, the entire THz path was enclosed in a box that could be purged with nitrogen gas, or evacuated to a pressure of < 1 mbar.

2.2.1 Femtosecond lasers

The time-domain spectrometer described herein was driven by a Ti:Sapphire laser: a brief overview of the physics behind ultra-short pulse generation in Ti:Sapphire crystals

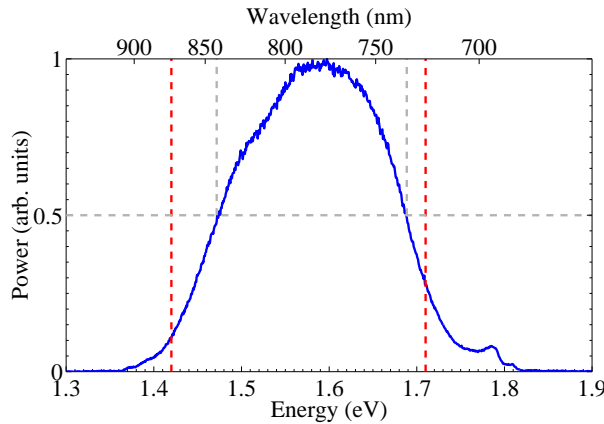


Figure 2.2: Spectrum of laser pulses output from the 10 fs FemtoSource Scientific Ti:Sapphire laser used in the work reported in this thesis, indicating its broad spectral width (the full-width at half-maximum is $\Delta\lambda = 108 \text{ nm}$). The dotted vertical lines at 1.42 eV and 1.71 eV show the Γ - and L-valley energy gaps for GaAs at room temperature and pressure; the other dotted lines indicate $\Delta\lambda$.

is given here, while a thorough review can be found in Spielmann *et al.* [62].

The electronic states of impurity atoms doped into a crystal are localised near specific lattice sites, in contrast to the delocalised electronic states in a semiconductor band. The electron-phonon interaction can couple these localised states to the lattice's spectrum of vibrational modes, producing continuous vibronic bands. For sapphire crystals doped with titanium ions this produces a broad absorption (and emission) spectrum. If the upper state is pumped efficiently from the ground state, a lasing medium with a large population inversion is created. Self mode-locking via the non-linear Kerr effect can be employed to produce a broadband pulse from the Ti:Sapphire crystal [63]. If the entire gain spectrum is utilised, pulse durations shorter than 10 fs can be obtained [63], corresponding to spectral widths exceeding 100 nm, as indicated in Figure 2.2.

The laser used in the majority of the work reported in this thesis was a FemtoSource Scientific Pro (Femtolasers Produktions GmbH.) [63], which output 10 fs duration

pulses at a 75 MHz repetition rate, with 500 mW average beam power (an energy per pulse of 7 nJ) centred at a wavelength of 790 nm (Figure 2.2). Chirped dielectric mirrors compensate for pulse dispersion within the laser cavity [63]. The Ti:Sapphire crystal was pumped at 4 W by a 532 nm Coherent Verdi laser, a frequency-doubled Nd:YAG laser that is itself pumped at 800 nm by a set of diode lasers. The only work reported in this thesis to not use this FemtoSource laser was the study of photoexcitation dynamics presented in Section 3.3.1, in which a regeneratively amplified Ti:Sapphire laser (Spectra Physics Spitfire Pro, 40 fs, 1 mJ pulse energy, 1 kHz repetition rate) was used.

2.2.2 Photoconductive generation of terahertz radiation

Various physical mechanisms exist for producing pulses of electromagnetic radiation with broad spectra covering the terahertz range, most of which are based on the excitation of a material with a ultrashort laser pulse. Conversion efficiencies are low: femtosecond optical lasers have pulse energies of 1 nJ to 1 mJ, but typical terahertz pulse energies are 1000 times smaller, in the range from $< 1 \text{ pJ}$ to $1 \mu\text{J}$ [64]. At high pump pulse energies (approaching 1 mJ), such as those available using amplified lasers, optical rectification in crystals such as ZnTe provides a good source of THz radiation [58; 64; 65]. Additionally, phase-matched difference frequency mixing can produce and detect pulses of radiation with spectra covering the entire mid-infrared (10-60 THz), but with lower power in the terahertz (0.1-10 THz) range [66].

For THz-TDS systems based on unamplified laser systems, however, photoconductive emitters provide the highest emitted powers. These sources are based on the ultrafast separation of photoexcited carriers in a semiconductor, forming a transient

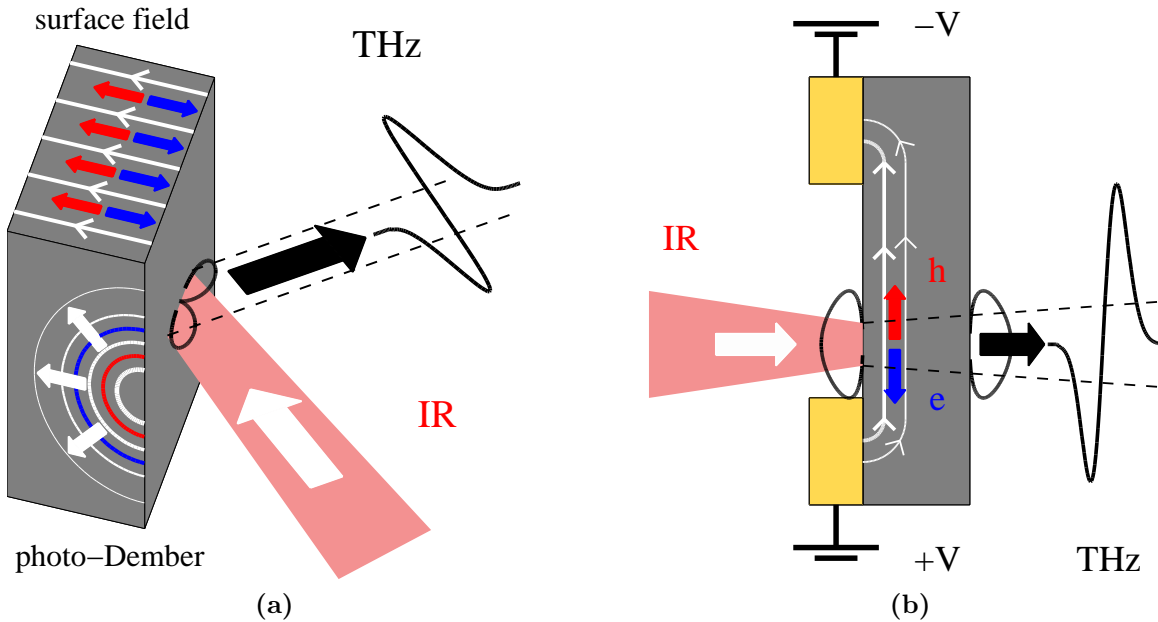


Figure 2.3: Photoconductive generation of THz radiation from (a) surface emitters and (b) photoconductive switches, after excitation by infra-red (IR) pulses. The two charge separation mechanisms in a surface emitter are shown in cross-section: on the side face the photo-Dember effect is illustrated for electrons (blue) and holes (red), while on the top face the surface depletion or accumulation layer (white lines, created by surface states) forms the radiating dipole. In a photoconductive switch the potential V applied to two metallic contacts (gold) creates a field (white lines) in the semiconductor that separates electrons (e) and holes (h). Photoexcitation near the anode creates a larger THz pulse [67]. The radiation patterns for both emitters are also shown (solid black line at the surface), after coupling into free-space [68].

dipole that radiates a pulse. Typically, the direct bandgap semiconductor gallium arsenide (GaAs) is used, owing to the proximity of its bandgap (1.42 eV at room temperature) to the peak gain of the Ti:Sapphire laser (around 800 nm, or 1.55 eV). The different mechanisms of charge separation are illustrated in Figure 2.3: it can be due to differing electron and hole mobilities (the photo-Dember effect), or may result from an electric field accelerating electrons and holes in opposite directions. In the latter case, the electric field can be internal, such as the depletion (or accumulation) field that exists near the surface of a semiconductor. THz radiation sources based on the

photoexcitation of a bare semiconductor [69] are referred to colloquially as *surface emitters* – the geometry of photoexcitation and emission are shown Figure 2.3a. Alternatively, the electric field can be applied laterally between metallic contacts placed on the semiconductor’s surface, and then the optical pulses are focussed onto the gap between contacts (Figure 2.3b). Such a device is called a *photoconductive switch*, alternatively known as the Auston switch, after its inventor [70]. In all these sources of THz radiation, the acceleration of charges produces a rapid rise in current flowing either away from the surface (surface emitters) or between contacts (photoconductive switches). This changing current emits a pulse of electromagnetic radiation according to Maxwell’s equations (Appendix A.1), typically with a duration of less than 1 ps. After accounting for the influence of the Fresnel transmission from the emitter into free-space, [68] the dipole formed has a distinct radiation pattern, shown in Figure 2.3 for both types of emitter. After a short time the field driving the separation of charges is screened by the dipole’s formation, and the ultrafast scattering, trapping and recombination of carriers begins to diminish and finally halt THz emission.

2.2.3 Electro-optic detection

THz radiation pulses can be detected by the reverse process to the photoconductive generation method just outlined: a THz electric field incident on a photoexcited carrier distribution generates a measurable current [71]. In this thesis, however, the well-established technique of electro-optic sampling [72; 73] was relied upon.

A typical electro-optic detection system is shown in Figure 2.1. The THz radiation from a sample is focussed onto an electro-optic crystal, such as ZnTe or GaP. When the probe beam P3 travels through the crystal at the same time as the THz pulse, its

plane of polarisation is rotated via the Pockels effect [74]. By subsequently separating orthogonal polarisation components with a Wollaston prism (WP), the intensity of the two components can be measured by a pair of photodiodes. The difference between the voltage on the two photodiodes is proportional to the THz electric field strength [75]. In order to obtain a high signal-to-noise ratio, the emitted THz electric field is modulated, either by applying an alternating voltage to a photoconductive switch, or by mechanically chopping the emitter's pump beam. The change in voltage across the photodiodes is then recorded via a lock-in amplifier referenced to the modulation frequency of the emitter. If delay stage 1 (Figure 2.1) is moved, the THz electric field can be mapped out as a function of time before and after the arrival of the sampling pulse in beam P3. To sample over a large frequency range a thin ($\sim 20\mu\text{m}$) crystal is required, in order to minimise the effect of the mismatch between the group velocities of the IR and THz beams. A free-standing thin crystal introduces internal reflections into the detected time-domain electric field, however, and therefore thick optically inactive substrates can be attached to enhance the spectrometer's frequency resolution, which discussed in the following section.

An alternative option to electro-optic sampling and photoconductive detection is the use of a pair of linked Ti:Sapphire femtosecond lasers, with a fixed repetition rate difference, and asynchronous optical sampling [76]. While the time-resolution of this method is currently limited to $\sim 230\text{ fs}$ by jitter in the time-base of the electronics, it has the advantage of not requiring a mechanical delay line, and higher scan rates (1 kHz) are available [76].

2.2.4 Spectral resolution and bandwidth

The usefulness and quality of spectral information obtainable from THz-TDS can be described by three characteristics: the frequency resolution, the bandwidth and the dynamic range (signal-to-noise ratio) of the spectrum. Since the resolution Δf is related to the length of the time domain window Δt by $\Delta f = 1/\Delta t$, it is desirable to have as large a Δt as possible. This is often necessary in order to measure accurately the (narrow) spectral line widths of molecular vibrational modes. In time-domain measurements internal reflections are resolvable from the sample, the THz emitter and the detector: an example is given in Figure 2.4. While the multiple internal reflections within the spectrometer can be accounted for, precise knowledge of the complex refractive indices of the various optical components is required. In practise it is simpler to window out multiple internal reflections in the time domain, which is achieved simply by using thick components. The time delay between two internal reflections in a component of thickness T is $\Delta t = 2nT/c$. Experimentally, 3 mm-thick semi-insulating GaAs photoconductive switches were used, and 20 μm - or 200 μm -thick (110) ZnTe crystals on 6 mm thick (100) ZnTe substrates as detectors. This produces a spectrometer with a minimum frequency resolution $\Delta f = c/(2nT) = 14 \text{ GHz}$, limited by the GaAs ($n = 3.5$) emitter. This resolution is comparable to the $\sim 10 \text{ GHz}$ laser linewidth of quantum cascade lasers [2].

Nyquist's criterion tells us that the maximum measurable frequency is half the inverse of the step size δt in time, or $f_{\max} = 1/(2\delta t)$. The pulse duration provides an approximate upper limit of $f_{\max} = 50 \text{ THz}$ for a 10 fs laser. However, since the step size of optical delay stages can be less than the duration of the pulse envelope (10 fs

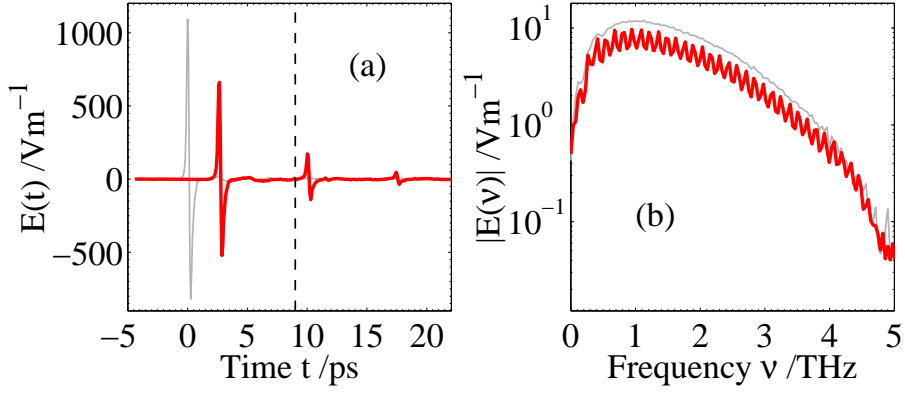


Figure 2.4: Typical THz-TDS data obtained on an optically thick sample (high-resistivity silicon, 0.33 mm thick). **(a)** The time-domain electric field transmitted through the sample E_s (thick line) is delayed by 2.6 ps with respect to the reference electric field E_r (thin line) owing to the medium's refractive index. The Fresnel transmission coefficients and absorption within the sample account for the reduction in the amplitude of E_s . Two multiple internal reflections are visible in the sample, at 10.0 ps and 17.4 ps. **(b)** Fourier transform spectra of time-domain data in (a) for E_s (thick line) and E_r (thin line). The multiple internal reflections produce the oscillatory shape of E_s , and can be removed by restricting the time domain data to up to 9 ps (dotted line in a).

$=3\mu\text{m}$), a stricter upper limit comes from the frequency mismatch between THz pulse and gate pulse in the detector [73]. An upper frequency of ~ 100 THz has recently been reported by Kubler *et al.*[8], for mid-infrared pulses generated and detected using GaSe.

In practice the spectral range of broadband THz emitters is limited by a number of factors, including the duration of the emitted pulse, which depends critically upon the dynamics of carriers in the emitter (Chapter 4), and the spectral response of the detection crystal. Furthermore, to acquire N time-domain data points within a practical time a compromise between bandwidth and resolution must be chosen, as $N = \Delta t/\delta t = f_{\max}/\Delta f$.

2.3 Complex refractive index of a thick sample

This section outlines the method of obtaining the complex refractive index of a material from THz-TDS, by comparing the terahertz electric field (E_s) transmitted through an optically thick sample with a reference electric field (E_r), typically taken without the sample present. The case of a thin, conductive film is treated separately in Section 3.2.2. If the sample is opaque at THz frequencies then the reflected electric field should be measured instead of that transmitted. In this case the reference waveform is taken from a material with a known reflectivity (e.g. a metallic mirror), and a different analysis is required (see e.g. Ref. [77]).

If E_r is measured in vacuum then $\tilde{n} = 1$, and therefore:

$$E_r(\omega) = E_i \exp \left[i \frac{\omega d}{c} \right] \quad (2.2)$$

where E_i is the electric field at some point before the sample. The electric field E_s after transmission through a sample of thickness d can be written in terms of E_r via:

$$\begin{aligned} E_s(\omega) &= t_{vs}t_{sv}E_i \exp \left[i \frac{\omega d}{c} \tilde{n} \right] \text{FP}_{vsv}(\omega) \\ &= t_{vs}t_{sv} \exp \left[i \frac{\omega d}{c} (\tilde{n} - 1) \right] \text{FP}_{vsv}(\omega) E_r, \end{aligned} \quad (2.3)$$

where the Fresnel transmission coefficients [78] are given by $t_{ij} = 2\tilde{n}_i / (\tilde{n}_i + \tilde{n}_j)$ at normal incidence, and the subscripts v and s denote vacuum and sample. The Fabry-Perot term $\text{FP}_{vsv}(\omega)$ accounts for the effect of multiple reflections within the sample, and is defined in general for light traversing from medium i to j to k as

$$\text{FP}_{ijk}(\omega) = \sum_{p=0}^P \left[r_{jk}r_{ji} \exp \left(i \frac{2\tilde{n}(\omega)\omega d}{c} \right) \right]^p, \quad (2.4)$$

where the Fresnel reflection coefficients are $r_{ij} = (\tilde{n}_i - \tilde{n}_j) / (\tilde{n}_i + \tilde{n}_j)$ at normal incidence.

Equation 2.3 suggests that a comparison of $E_s(\omega)$ and $E_r(\omega)$ should yield $\tilde{n}(\omega)$.

Defining the complex transmission function $\tilde{T}(\omega) = E_s(\omega)/E_r(\omega)$ yields

$$\tilde{T}(\omega) = |\tilde{T}|e^{i\phi(\omega)} = t_{vs}t_{sv} \exp \left[i \frac{\omega d}{c} (\tilde{n} - 1) \right] \text{FP}_{vsv}(\omega). \quad (2.5)$$

The presence of $\tilde{n}(\omega)$ in both t_{ij} and FP_{vsv} means that Equation 2.5 cannot in general be rearranged into an analytical expression for $\tilde{n}(\omega)$ in terms of the experimentally determined $\tilde{T}(\omega)$. \tilde{n} can always be obtained, however, via iterative numerical methods such as those outlined by Duvillaret *et al.* [79; 80], and Dorney *et al.* [81]. However, if certain criteria are met an analytic expression for $\tilde{n}(\omega)$ can be obtained, as is now discussed.

2.3.1 Analytical expression for the complex refractive index

If no multiple reflections are seen from the sample then $p = 0$, and $\text{FP}_{vsv}(\omega) = 1$. This can be achieved experimentally by windowing the time-domain data, as in Figure 2.4. If we further make the approximation that the frequency dependence of $\tilde{n}(\omega)$ is weak, and that $t_{ij}(\tilde{n}) = t_{ij}(\tilde{n}(\omega = 0))$ then analytical expressions for the refractive index n and absorption coefficient $\alpha = 2\omega\kappa/c$ can be obtained:

$$n(\omega) = 1 + \frac{c}{\omega d} \phi(\omega), \quad (2.6)$$

$$\alpha(\omega) = -\frac{2}{d} \ln \frac{|\tilde{T}(\omega)|}{|t_{vs}t_{sv}|}. \quad (2.7)$$

2.3.2 Dispersion relations

It is possible to obtain the dispersion relation for a material directly from \tilde{n} obtained via THz-TDS. Rather than obtaining the function $\omega(k)$, the dispersion relation is

described via $k(\omega)$ using the result $k(\omega) = \tilde{n}(\omega)\omega/c$ (Appendix A.1). In the case of weak dispersion (Section 2.3.1) the dispersion relation is simply:

$$k(\omega) = \frac{\phi(\omega)}{d} + \frac{\omega}{c}. \quad (2.8)$$

2.4 Examples of THz-TDS

As discussed in Section 1.3.1, a diverse range of materials of current scientific and industrial interest exhibit marked features in the THz range of the electromagnetic spectrum. In this section an experimental survey of the key phenomena that create a response at THz frequencies is presented – results that are important later in this thesis.

2.4.1 Phonon-polariton dispersion

In an ionic crystal, a photon couples with other transverse vibrations, such as TO-phonon modes, resulting in a propagating quasiparticle known as a phonon-polariton. The dielectric function $\epsilon(\omega)$ is well described by the Lorentz oscillator model [82], in which:

$$\epsilon_{\text{TO}}(\omega) = \epsilon_{\infty} + (\epsilon_s - \epsilon_{\infty}) \frac{\omega_{\text{TO}}^2}{\omega_{\text{TO}}^2 - \omega^2 - i\omega\Gamma}, \quad (2.9)$$

where ω_{TO} and Γ are the TO-phonon frequency and damping rate. This expression can be derived either quantum mechanically from a perturbative treatment of the light-matter interaction (in the electric dipole approximation), or macroscopically from the equation of motion for an electron including damping [82]. The lattice is highly reflective when $\omega_{\text{TO}} < \omega < \omega_{\text{LO}}$, where $\omega_{\text{LO}} = \omega_{\text{TO}}\sqrt{\epsilon_s/\epsilon_{\infty}}$ is the LO phonon frequency, owing to the dielectric function having a large imaginary component, restricting the

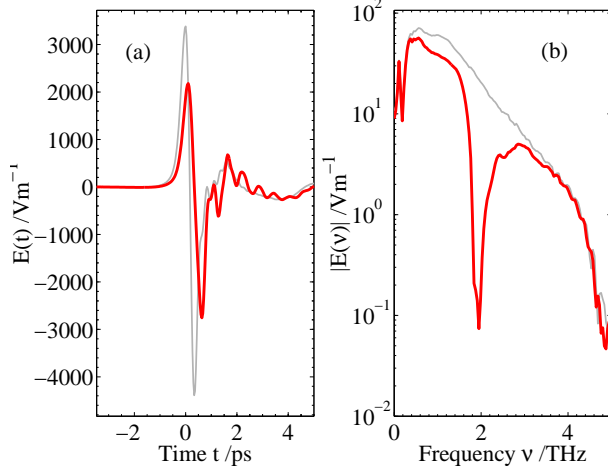


Figure 2.5: (a) Time-domain electric field. After transmission through CsI, the THz electric field has an additional oscillatory component. (b) Amplitude spectra, indicating CsI's TO-phonon mode at 1.8 THz.

propagation of electromagnetic radiation. This range is loosely analogous to the electronic bandgap of semiconductors and the bandgap of photonic crystals. Away from ω_{TO} the polariton is photon-like, exhibiting linear dispersion with $\omega = ck/\sqrt{\epsilon_s}$ in the lower polariton branch ($\omega \ll \omega_{\text{TO}}$) and $\omega = ck/\sqrt{\epsilon_\infty}$ in the upper branch ($\omega \gg \omega_{\text{TO}}$). The high-frequency dielectric constant ϵ_∞ describes the response of the valence electrons to electromagnetic radiation at energies significantly below the bandgap energy. The applicability of Equation 2.9 has been well known for a number of decades, and was initially demonstrated via reflectivity measurements in the mid- and far-infrared [82]. Phonon-polariton dispersion relations can be measured more directly with Raman spectroscopy, in which an incident photon is scattered by a phonon, and the intensity of scattered light is determined at various angles [83]. Recent years have seen a resurgence in the interest in phonon-polaritons, following experiments that demonstrate the coherent control of polaritons within a patterned medium [84]. This has lead to suggestions for polaritonic devices, in which THz radiation is generated, prop-

agated along a waveguide, and detected within a single solid-state chip [84]. THz-TDS offers advantages over both Raman and reflectivity spectroscopy in the investigation of phonon-polaritons, as is now discussed with the specific example of CsI.

The THz electric field transmitted through a $30\ \mu\text{m}$ thick CsI crystal was measured, and is shown in Figure 2.5. The additional oscillations in the time-domain are due to the strong absorption of THz radiation close to the TO-phonon frequency (1.8 THz). In Figure 2.6 the real and imaginary parts of both the complex refractive index \tilde{n} , and the response function $1/\epsilon$ are plotted, calculated as described above (Section 2.3.1). The theoretical curves, derived from Equation 2.9 with $\omega_{\text{TO}} = 1.75\ \text{THz}$, $\epsilon_s = 5.65$, $\epsilon_\infty = 2.7$, $\Gamma = 0.9 \times 10^{12}\ \text{s}^{-1}$, are in excellent agreement with experiment.

A key advantage of THz-TDS over reflectivity measurements is that the complex dielectric function can be determined without use of the Kramers-Kronig relations. THz-TDS also has beneficial aspects in comparison with Raman spectroscopy, in which the wavevector of the polariton is determined from $k^2 = k_i^2 + k_s^2 - 2k_i k_s \cos \theta$, where the incident (scattered) photon has wavevector k_i (k_s), and θ is the scattering angle. When θ is small, the intense peak from elastic scattering can swamp the weaker Raman signal, making the experimental measurement of k away from phonon modes a challenge. Raman spectroscopy requires the rotation of the detector over θ , and cannot measure both upper and lower polariton branches within the same scattering geometry [83]. THz-TDS does not have these disadvantages, and furthermore is less likely to damage a sample (weak far infra-red pulses are used, rather than the intense visible radiation typically used in Raman spectroscopy). Furthermore, measuring the low-frequency modes of polaritons in birefringent media such as ferroelectrics is more readily done via THz-TDS, which does not face problems associated with the wavevector change

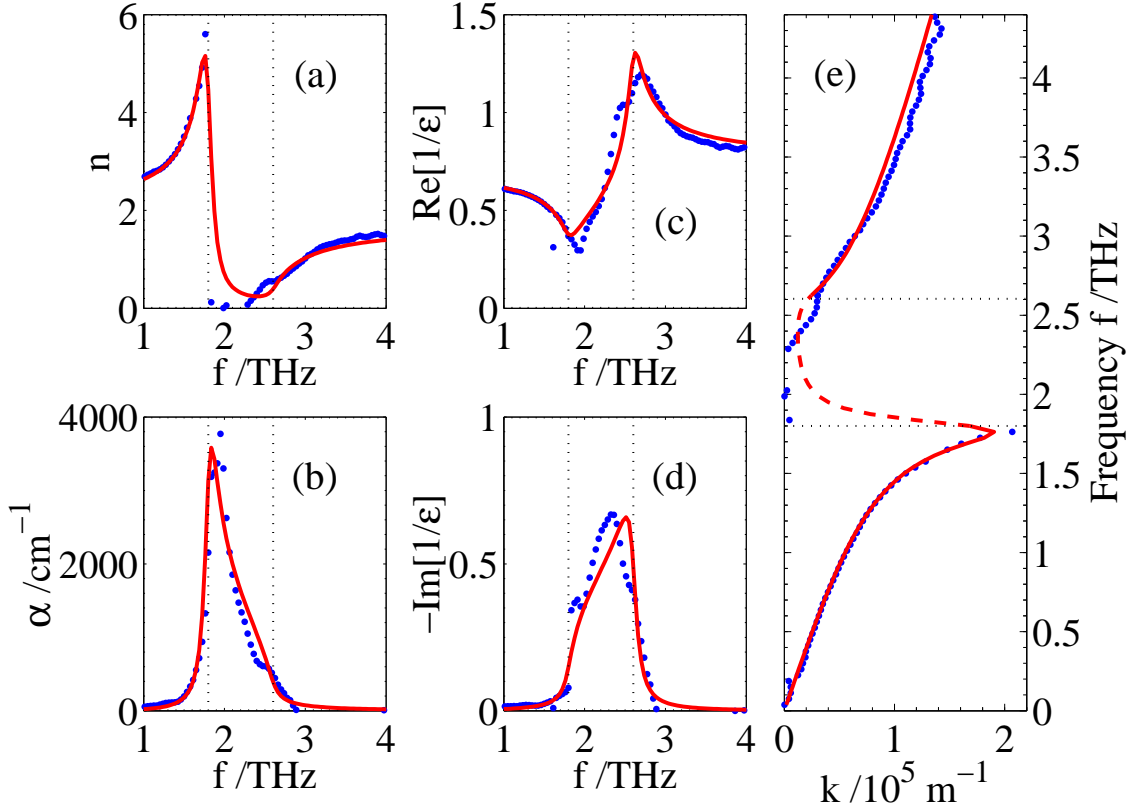


Figure 2.6: (a) Real part of refractive index of CsI determined from experiment (dots), and from Drude-Lorentz model (solid line). Fit parameters are: $\omega_{\text{TO}} = 1.75 \text{ THz}$, $\epsilon_s = 5.65$, $\epsilon_\infty = 2.7$, $\Gamma = 0.9 \times 10^{12} \text{ s}^{-1}$. Dashed lines mark the TO and LO phonon frequencies (1.8 THz and 2.6 THz). (b) Absorption coefficient of CsI. (c) and (d) Real and imaginary part of response function $1/\epsilon$. (e) Phonon polariton dispersion relation, where the wavevector k was calculated from $k(\omega) = \omega \tilde{n}/c$.

between ordinary and extraordinary propagation [20].

2.4.2 Rotational modes of water vapour

Far infra-red radiation couples strongly to the rotational modes of atmospheric water vapour, with numerous modes in the terahertz range. The frequencies and absorption coefficients of these modes have been measured precisely in the past in the range $0.2 - 1.45 \text{ THz}$ using THz-TDS, [85] and the transmission change up to 3 THz has

been reported [76]. In this section the complex refractive index of water vapour in the range $0.2 - 4.8$ THz is reported. Excellent agreement is found with the absorption lines reported in the literature, demonstrating that the THz spectrometer is calibrated correctly. Additionally, the knowledge of the principal atmospheric transmission bands is vital for future optical communications systems operating at THz frequencies.

In Figure 2.7 the time-domain electric fields are shown as measured in a vacuum of 1 mbar (E_s) and in air (E_r) at room temperature and pressure, and 40% humidity. The time-domain traces were taken over a delay of 70 ps, with no multiple internal reflections in this range owing to the use of a 3 mm-thick SI-GaAs photoconductive emitter, and a $20\ \mu\text{m}$ (110) on 6 mm (100) ZnTe. This enabled a frequency resolution of 14 GHz to be obtained (Section 2.2.4). The THz path length within the spectrometer (the sample thickness) was 0.49 m. The complex refractive index is also presented in Figure 2.7, in which 70 absorption peaks are discernable in the range $0 - 5$ THz. The complex refractive index can be modelled well by a Drude-Lorentz dielectric function with multiple oscillators, as shown in the insets to plots c) and d) of Figure 2.7 for the modes at 0.557 THz and 0.752 THz. The measured lifetimes of these modes are $1/\Gamma = 20$ ps, which is why atmospheric water vapour absorption produces the long-lived “ringing” after a THz pulse. On a practical note, these oscillations are useful in alignment of THz systems, to help find the position of zero delay. The second harmonics of a number of modes are visible in Figure 2.7: for example the higher orders of the 1.101 THz mode can be seen at 2.202 THz and 4.403 THz (the mode at 3.303 THz is obscured by the second order of the 1.672 THz mode, at 3.344 THz).

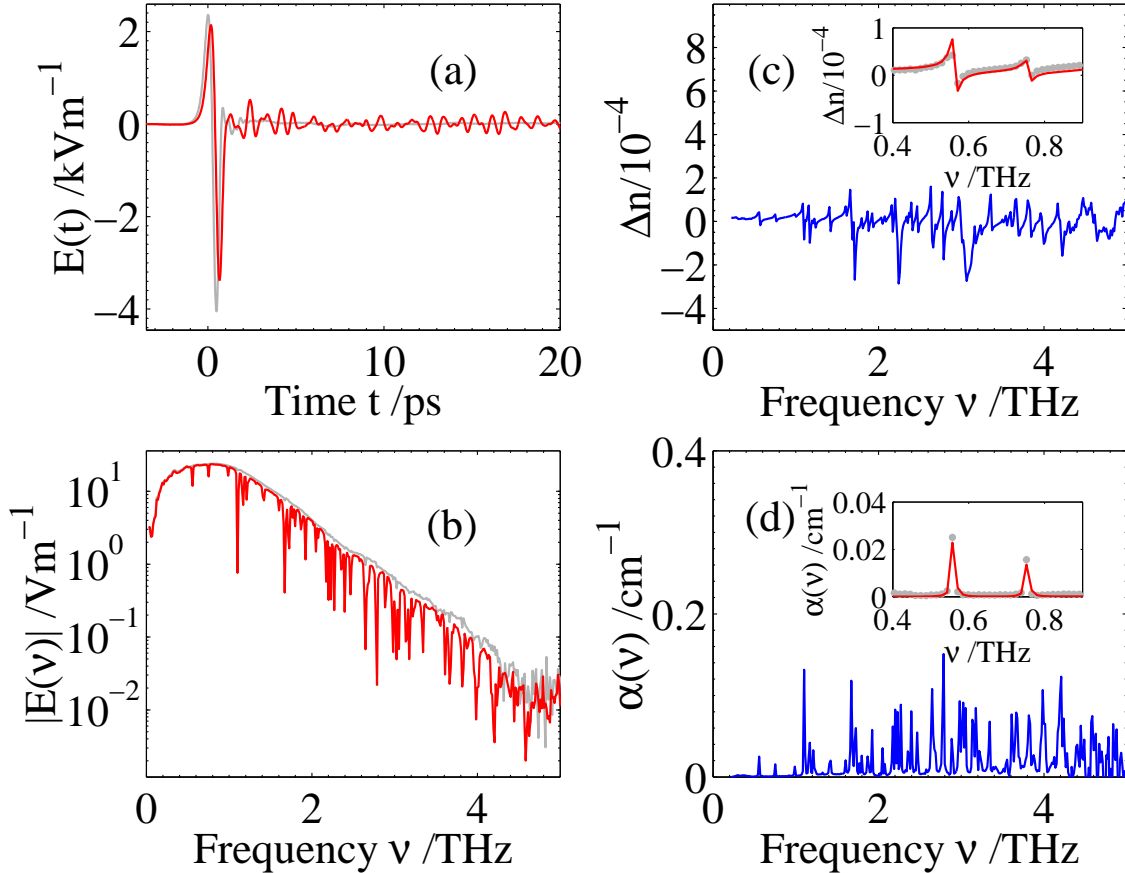


Figure 2.7: (a) Measured time-domain electric fields and (b) spectra obtained in a 1 mbar vacuum (grey lines) and at atmospheric pressure (red lines). Note that some water vapour absorption is still visible in the reference, which can be removed by purging with nitrogen gas and purging successively. (c) Refractive index of water vapour, up to 5 THz, plotted as $\Delta n = n - 1$. (d) Absorption coefficient. The measured absorption lines are (with the principal lines highlighted in bold): 0.557, 0.752, 0.989, **1.101**, 1.170, 1.212, 1.324, 1.421, 1.602, **1.672**, 1.728, 1.770, 1.797, 1.867, 1.923, 2.048, 2.076, 2.174, 2.202, 2.229, 2.271, 2.327, 2.355, 2.397, 2.438, 2.466, 2.578, **2.647**, **2.787**, 2.884, 2.982, 3.024, 3.052, 3.135, 3.177, 3.219, 3.344, 3.386, 3.414, 3.511, 3.553, 3.609, 3.665, 3.734, 3.818, 3.874, 3.929, **3.985**, 4.097, 4.124, **4.208**, 4.236, 4.278, 4.333, 4.403, 4.445, 4.487, 4.542, 4.584, 4.626 THz. For comparison, the lines reported by Exter *et al.* [85] are 0.557, 0.752, 0.998, 1.097, 1.113, 1.163, 1.208, 1.229 and 1.410 THz. The insets in c) and d) illustrate a Drude-Lorentz oscillator fit (lines) to the data (dots) in the vicinity of the modes at 0.557 THz and 0.752 THz.

2.4.3 Free electron plasmas

A good understanding of the conductivity of metallic and semiconducting materials, essential in today's electronics industry, can be obtained via the Drude-Lorentz model of a free-electron gas. The Drude-Lorentz model has been applied widely to inorganic semiconductors within the field of THz-TDS, in studies of doped semiconductors such as silicon [10] and GaN [86] and photoexcited GaAs [87; 88] and InP [23]. Further examples of its use include the superconductor YBCO [89] and the doped (metallic) polymer polypyrrole [12].

In the Drude-Lorentz treatment the material of interest is modelled as a plasma, namely a medium in which mobile charges (e.g. electrons) move with respect to a fixed lattice of charges with an opposite sign (e.g. positively charged ions). For doped semiconductors the dielectric function is of the form:

$$\epsilon_{\text{pl}}(\omega) = \epsilon_{\infty} - \frac{Ne^2}{m^*\epsilon_0(\omega^2 + i\omega\Gamma)}, \quad (2.10)$$

where ϵ_{∞} is the high frequency dielectric constant [82]. N , m^* and Γ are respectively the concentration, effective mass and scattering rate of free carriers. Γ is related to the phenomenological scattering time τ by $\Gamma = 1/\tau$. For metals the same equation holds, but with $\epsilon_{\infty} = 1$ and $m^* = m_e$.

The frequency-dependent response of a free-electron gas can be understood with reference to the plasma frequency ω_p , which is the frequency at which $\epsilon_{\text{pl}} = 0$ in the case of zero damping ($\Gamma = 0$). From Equation 2.10, the plasma frequency is

$$\omega_p = \sqrt{\frac{Ne^2}{m^*\epsilon_{\infty}\epsilon_0}}. \quad (2.11)$$

When $\omega < \omega_p$ the free-electron gas can respond to electromagnetic radiation, while above ω_p the plasma can no longer react to the driving force. This interaction produces

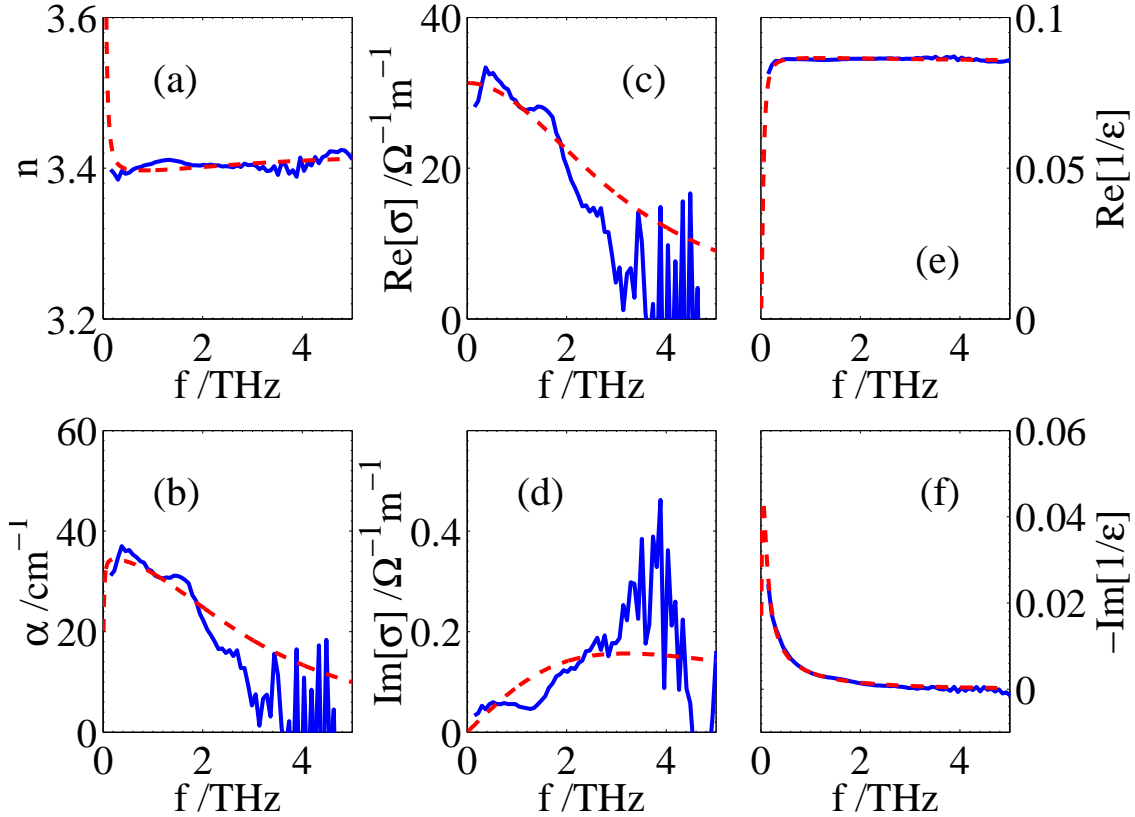


Figure 2.8: Complex refractive index of doped silicon obtained using THz-TDS (solid lines), and fits using the Drude-Lorentz model (dashed lines). **(a)** Refractive index; **(b)** Absorption coefficient; **(c)** Real part of conductivity; **(d)** Imaginary part of conductivity; **(e)** Real part of inverse dielectric function $1/\epsilon$; **(f)** Imaginary part of $-1/\epsilon$.

a frequency-dependent complex refractive index, with a large absorption coefficient below ω_p .

The electrical conductivity $\sigma(\omega)$ can be calculated from the dielectric function using the relation $\epsilon(\omega) = \epsilon_\infty + i\sigma(\omega)/(\epsilon_0\omega)$, which is derived from Maxwell's equations in Appendix A.1. The conductivity exhibits a maximum at zero frequency, with a value $\sigma(\omega = 0) = Ne^2/(m^*\Gamma)$. Defining the electron mobility $\mu = e\tau/m^*$, where $\tau = 1/\Gamma$ is the mean time between scattering events, produces the well-known result $\sigma(\omega = 0) = Ne\mu$.

Figure 2.8 illustrates the complex refractive index, conductivity and inverse dielec-

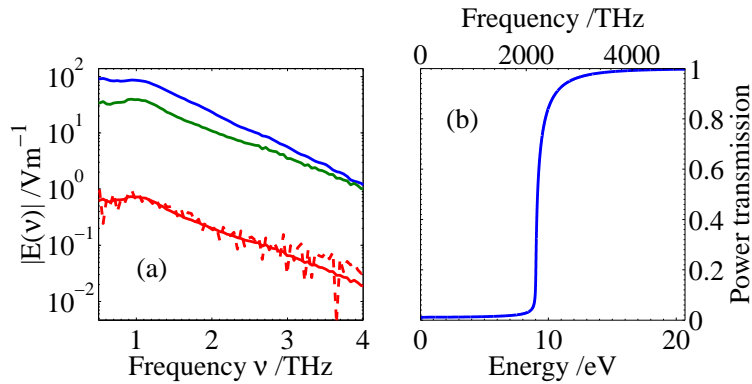


Figure 2.9: (a) Amplitude spectra of measured reference THz electric field (top line), after transmission through silicon (middle line), and after transmission through a 30 nm gold layer on silicon (bottom, dashed line). The amplitude expected using the Drude-Lorentz model for gold (parameters given in the text) is also shown (bottom, solid line). (b) Modelled transmission of gold, illustrating its transparency in the UV above the plasma frequency (9.0 eV).

tric function for an n-type silicon sample, as measured using the THz spectrometer and method outlined in Section 2.3. Good agreement is found with the Drude-Lorentz model just described, when $N = 8 \times 10^{15} \text{ cm}^{-3}$ and $\Gamma = 2 \times 10^{13} \text{ s}^{-1}$. The accurate description of the interaction between THz radiation and electrons in silicon provided by the Drude-Lorentz model is crucial in later chapters of this thesis: it is applied in the study of carrier trapping in polymer transistors during Chapter 5, and in Chapter 3 photoexcited electron-hole plasmas are treated within its framework. The propagation of THz radiation within a free-electron plasma is also critical in some THz emitters, as discussed in Section 4.3 with regard to emission from InSb surfaces.

THz-TDS can also be employed to determine the complex refractive index of thin-films of metals. In a recent study, Gilmore *et al.* [17] used the temperature dependence of THz transmission through a thin metallic film to extract the electron-phonon coupling constant of lead. In this section, the THz transmission of a thin (30 nm) layer of gold deposited on a silicon substrate is reported, as shown in Figure 2.9.

The amplitude of THz radiation after transmission through gold is more than an order of magnitude smaller than that through the silicon substrate. This finding is of particular relevance to the THz spectroscopy of polymer transistors, as described in Section 5.3. The Drude-Lorentz dielectric function models the data accurately, with $N = 5.9 \times 10^{22} \text{ cm}^{-3}$ and $\Gamma = 8 \times 10^{13} \text{ s}^{-1}$. The corresponding conductivity is $2.1 \times 10^7 \Omega^{-1} \text{ cm}^{-1}$, and is effectively constant over the THz range as the modelled plasma frequency, $\omega_p/2\pi = 2.2 \times 10^{15} \text{ Hz}$, lies in the ultra-violet frequency range at 9.0 eV (Figure 2.9b). No measurable time delay is observed in the time-domain electric field transmitted through the gold film (with respect to the silicon), indicating that the thin-film limit (Equation 3.7) is valid.

2.4.4 Transmission through metallic waveguides

The temporal beam profile of electron beam bunches in a free-electron laser can be determined by examining the Smith-Purcell radiation emitted [90]. This radiation is produced by the diffraction of the relativistic electron beam from a periodic grating, and occurs at terahertz frequencies. In order to measure successfully the far infra-red Smith-Purcell radiation emitted it is necessary to eliminate light at lower frequencies using a suitable filter, such as a “waveguide array plate” (WAP) [91]. These filters consist of holes of diameter d drilled (using a CNC machine) in a hexagonal lattice (hole spacing s) through a $\sim 1 \text{ mm}$ thick metal (copper) sheet, as shown schematically in the inset of Figure 2.10a. WAPs are designed to act as band-pass filters, i.e. to transmit electromagnetic radiation within a narrow frequency range. The lowest frequency mode (TE11) that can propagate through the holes, which act as a circular metallic waveguide (of infinite length), is $f_c = 1.841c/\pi d$ [91]. The cut-off at higher frequency is

due to the lowest order diffraction mode, which will occur at a frequency $f_d = 2c/\sqrt{3}s$ for a hexagonal array.

A number of WAPs were characterised using THz-TDS, to obtain their transmission functions over the THz range. Typical time-domain electric fields after transmission through a WAP are shown in Figure 2.10a for filters designed to have maximum transmission at 456 GHz and 1.2 THz. The oscillatory time-domain shape results from the filters having a maximum in transmission between f_c and f_d . The filters all exhibit a sharp cut-off in transmission at the design frequencies of their waveguide modes, $f_c = 0.37$ THz and $f_c = 1.03$ THz respectively (Figure 2.10b), and have a power transmission of less than 10^{-5} at frequencies below f_c (Figure 2.10c). The drop-off in power above the lowest order diffraction mode ($f_d = 0.55$ THz and $f_d = 1.51$ THz respectively) is less dramatic, as the filters were placed at the focal point of THz radiation in the spectrometer. For filters designed with even lower f_c (larger d) the effect of diffraction from the hole array was more noticeable: moving the array 1 cm from the focus significantly reduced the THz power collected by the spectrometer above f_d for a 200 GHz filter (Figure 2.10d).

2.5 Summary

In this chapter the principles of terahertz time-domain spectroscopy were outlined, and detailed examples of the use and benefits of the technique were given. An overview of the photoconductive generation and electro-optic detection of pulses of terahertz radiation was given, with the specific details of the spectrometer used herein. After discussing how to extract the complex refractive index of a sample from time-domain

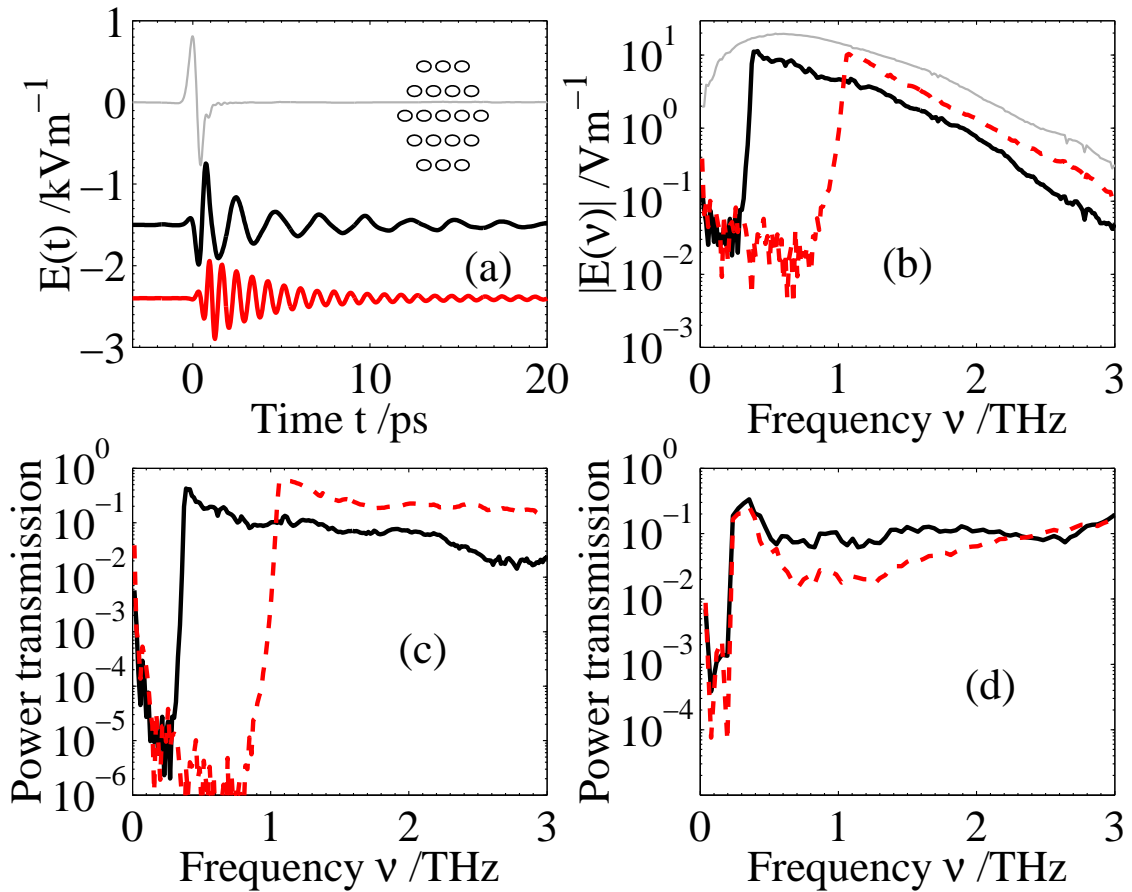


Figure 2.10: (a) Time-domain electric field of reference (top line, decreased by a factor of 3) and of filters designed to have maximum transmission at 456 GHz (middle line, vertically offset for clarity) and 1.2 THz (bottom line), measured over an electro-optic sampling delay of 70 ps. (Inset) indicates the hexagonal lattice of the waveguide array plate. (b) Amplitude spectra E_s for 456 GHz filter (thick, solid line) and 1.2 THz (dashed line) WAPs, and reference E_r (thin line), obtained from a). (c) Power transmission $|E_s/E_r|^2$ for the two filters. The experimental noise floor limits the transmission below f_c . (d) The power transmission for a filter with maximum transmission at 200 GHz when placed at THz focus (solid line) and 1 cm from focus (dashed line).

measurements, the phonon-polariton dispersion of CsI (Section 2.4.1) and the conductivity of silicon and gold (Section 2.4.3) were reported, and related to theory. Finally, band-pass filters operating in the THz regime were characterised (Section 2.4.4), and demonstrated to operate within their designed range.

Chapter 3

Carrier dynamics in damaged inorganic semiconductors

“No physical quantity can continue to change exponentially forever.
Your job is delaying forever.”

G. Moore, *International Solid-State Circuits Conference*, San Francisco,
2003.

3.1 Ultrafast optoelectronics

The driving force behind many of the developments in electronics is the need to transfer and process information at ever faster rates. There is a growing demand for ever higher data bandwidths, necessitating advances in our understanding of how semiconductors interact with light on ultra-short (sub-picosecond) timescales. Numerous devices exist that exploit the interaction between electronic states in semiconductors and photons of light: solid-state lasers, LEDs, quantum-confined structures (such as quantum cascade lasers), photodiodes and solar cells, to name but a few. In a variety of these optoelectronic devices, including photoconductive emitters and detectors of terahertz radiation, a large response to illumination is desirable, but only for an ultra-short timescale. In the language of semiconductor physics this translates to wanting a photoexcited carrier to have a large mobility, but a short carrier lifetime – typically

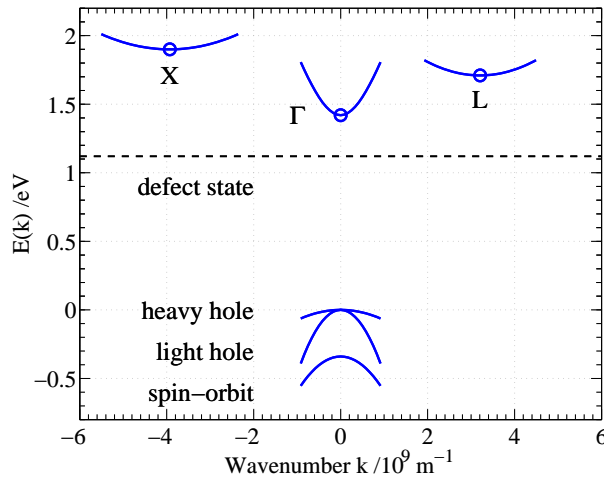


Figure 3.1: Band structure of GaAs, typical of the III-V semiconductors. Parabolic bands are plotted (solid lines), showing the Γ , L and X valleys of the conduction band, and the three valence bands. The defect level (dotted line) created by the arsenic anti-site in GaAs:As⁺ lies 0.3 eV below the conduction band minimum [92].

1 ps or less. Such a material can be obtained via *ion implantation* or *low-temperature growth* of a semiconductor, techniques which are outlined below.

In this chapter optical-pump THz-probe spectroscopy is introduced – a technique that can measure directly the conductivity of photoexcited carriers on a sub-picosecond time scale. The time-resolved conductivity of samples from the semi-insulating III-V semiconductor system $\text{In}_{1-x}\text{Ga}_x\text{As}$ are presented, in order to elucidate the interaction between THz radiation and photoexcited semiconductors. Finally, an investigation is reported of the carrier dynamics in low-temperature grown GaAs, and ion-implanted InP.

3.1.1 Semi-insulating direct bandgap semiconductors

The III-V semiconductors and (most of) their alloys exhibit a direct band gap, in which the transition between the highest filled electronic state (in the valence band)

and the lowest empty state (in the conduction band) occurs at close to zero wavevector. This situation is shown for GaAs in the simplified bandstructure of Figure 3.1, in which the direct bandgap energy is $E_\Gamma = 1.42\text{ eV}$ at room temperature and pressure. Semiconductors have an intrinsic electron and hole density created by thermal excitation across the bandgap, and an extrinsic concentration from dopant (impurity) ions in the crystal. Defects can be introduced during crystal growth that pin the electronic Fermi level close to the mid-point of the bandgap, producing a semiconductor with a near-intrinsic equilibrium carrier concentration. If the direct bandgap is sufficiently large, then the semiconductor has an extremely high dark resistivity, and is termed *semi-insulating*.

A comprehensive review of the physics and applications of semi-insulating semiconductors can be found in Ref. [93]; examples include Fe-doped InP and non-stoichiometric GaAs. While semi-insulating materials have use as replacements for oxide insulator layers in semiconductor devices, their use in ultrafast electronic components is limited by the long lifetime of their injected carriers, which can exceed 1 ns. Highly resistive semi-insulating materials that have shorter carrier lifetimes, and are suitable for ultrafast optoelectronics, can be created by introducing additional defects into the bandgap. Two techniques of achieving this are now outlined: semiconductor growth at low temperature, and ion-implantation.

3.1.2 Low-temperature growth

Gallium arsenide, and other III-V semiconductors, are typically grown via molecular beam epitaxy or metal-oxide chemical vapour deposition [82] at temperatures exceeding 500 °C. If, however, the growth procedure is performed in the range 190-350 °C

then additional defect centres are created. In low-temperature-grown (or LT-) GaAs a number of defects form, including As precipitates, substitutional and interstitial defects and vacancies [94]. A post-growth thermal annealing step is often used to remove some of these defects, in order to produce a high dark resistivity. With a careful control of the growth temperature a material with an ultra-short photoexcited carrier lifetime can be created, for instance as short as 0.1 ps for LT-GaAs [94].

3.1.3 Ion-implantation

An alternative method of creating a material with an ultra-fast optical response is the technique of ion implantation, in which accelerated ions bombard and damage the crystal structure of a pristine semiconductor. A sufficiently energetic incident ion will eject an atom in the target from its lattice site, creating a vacancy. The ejected atom can create additional vacancies (termed recoil vacancies) as it decelerates. The defects created during ion-implantation can trap and scatter photoexcited electrons on sub-picosecond timescales [95; 96; 97].

Ion-implantation has a number of benefits in comparison to low-temperature growth. The controllable ion dosage permits samples with more reproducible properties than LT-GaAs, where difficulties in controlling the temperature during growth result in nominally identical samples having different properties. Ion-implantation has the further characteristic of generating damage over a broad depth range, with a distribution that is almost Gaussian [98]. The defect concentration can be tailored by choosing the ion type, dose, and energy, and implantation can be performed in specific target areas.

The Australian National University 1.7 MV tandem accelerator was used to irra-

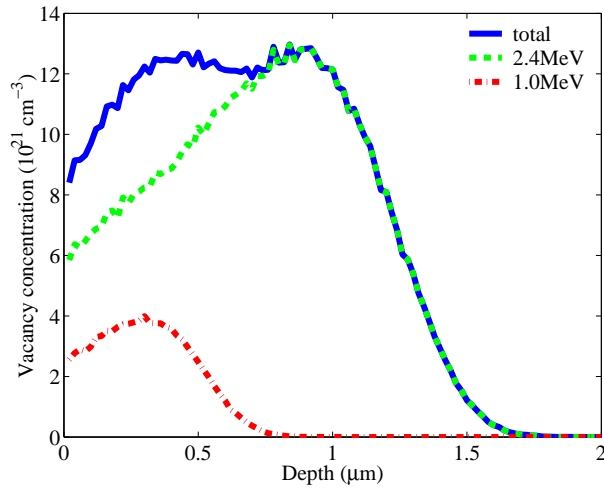


Figure 3.2: Damage profile for arsenic-implanted GaAs – the depth dependence of vacancies (including recoil vacancies) was calculated using the SRIM software [99]. The 1 MeV, $2.5 \times 10^{15} \text{ cm}^{-2}$ dose (dash-dotted line) and 2.4 MeV, $1.0 \times 10^{16} \text{ cm}^{-2}$ dose (dashed line) create an approximately uniform damage profile (solid line) extending over $1 \mu\text{m}$ from the surface. By scaling the concentration according to the dose, the distributions for samples implanted at lower doses can be obtained.

diate a variety of semiconductors with ions, at room temperature. In order to create defects over the absorption depth for band-gap energy light ($\sim 1 \mu\text{m}$), sufficiently energetic ions are required (typically more than 1 MeV for arsenic and iron ions). Approximately uniform damage profiles were created by employing a number of implants, at varying energies and doses. A typical damage profile is shown for arsenic-implanted GaAs (GaAs:As⁺) in Figure 3.2, which was obtained using the Stopping Range of Ions in Matter (SRIM) software [99]. This suite of programs uses a quantum mechanical treatment of ion-atom collisions to calculate the damage that each incident ion produces.

The principal defect in arsenic ion-implanted GaAs (GaAs:As⁺) is thought to be the antisite donor defect As_{Ga}, where As replaces Ga on some Ga lattice sites. Deep-level transient spectroscopy has found that the defect energy levels in GaAs:As⁺ lie

~ 0.3 eV below the conduction band [92]. The electron lifetime in GaAs:As⁺ can be as short as that of LT-GaAs, i.e. ~ 0.1 ps [95; 100]. By performing a post-implant anneal the resistivity of GaAs:As⁺ can be increased to levels comparable to LT-GaAs [100; 101], as is desirable for ultra-fast semiconductors in general, and photoconductive terahertz emitters in particular (Section 4.2.1).

3.1.4 Shockley-Read-Hall lifetime model

The Shockley-Read-Hall (SRH) approach [102] can be used to model the lifetimes of injected carriers in semiconductors, by calculating the expected rate of electron-hole recombination. Within this model the carrier lifetime τ is related to the concentration of recombination centres N_t by

$$\frac{1}{\tau} = N_t v_{\text{th}} \Sigma, \quad (3.1)$$

where Σ is the scattering cross-section for a single isolated defect (typically of the order of magnitude of the defect's cross-sectional area). The thermal velocity v_{th} of a carrier is calculated by equating its kinetic energy $m^* v_{\text{th}}^2 / 2$ and thermal energy $3k_B T / 2$, resulting in

$$v_{\text{th}} = \sqrt{\frac{3k_B T}{m^*}}. \quad (3.2)$$

For example, with an electron effective mass of $m^* = 0.08m_e$ (InP) this results in $v_{\text{th}} = 4.1 \times 10^5$ ms⁻¹.

A number of authors have used the SRH model (Equation 3.1) to investigate the carrier dynamics of LT-GaAs, in order to extract the density of recombination centres from

$$N_t = \frac{1}{\tau v_{\text{th}} \Sigma}. \quad (3.3)$$

The assumption of a constant Σ is made, with a thermal velocity given by Equation 3.2 and a lifetime either from optical-pump THz-probe spectroscopy[103; 104] or from time-resolved reflectivity [105]. For instance, Prabhu *et al.*[103] report that a LT-GaAs sample grown at 300°C with a lifetime of 0.2 ps has $N_t \sim 10^{19} \text{ cm}^{-3}$, when it is assumed that $\Sigma = 7 \times 10^{-15} \text{ cm}^{-2}$. Similarly, Nemec *et al.*[104] find $N_t \sim 4 \times 10^{18} \text{ cm}^{-3}$ with $\Sigma = 2 \times 10^{-15} \text{ cm}^{-2}$. The SRH model is applied to semi-insulating GaAs with passivated surface states in Section 3.3.2, to ion-implanted InP in Section 3.5.3, and later to trapping in semiconducting polymers in Section 5.4.

3.2 Time-resolved conductivity

The experimental and theoretical concepts underpinning the technique of optical-pump THz-probe spectroscopy are outlined in this section, before a brief comparison is made with other time-resolved spectroscopic methods.

3.2.1 Experimental setup

The experimental setup of the optical-pump THz-probe system used in this work is shown in Figure 2.1. The THz electric field transmitted through the sample was recorded via electro-optic sampling, as described in Section 2, using a first lock-in amplifier referenced to the voltage driving the photoconductive switch. An additional part of the laser beam was split off before the THz delay stage, and was sent (collinearly with the THz pulse) to the sample in order to photoexcite carriers (beam P2). The photoexcited carriers in the sample alter the material's conductivity, changing its transmission to THz radiation. However, at the sample pump fluences available from

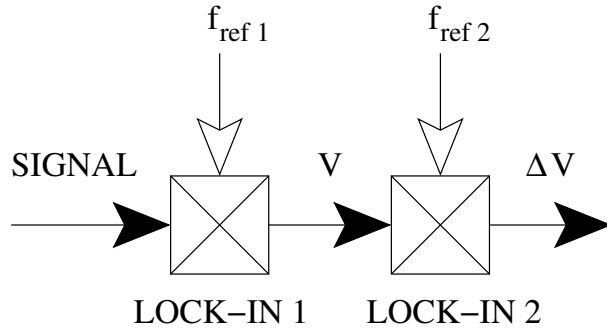


Figure 3.3: The difference voltage (SIGNAL) from the balanced electro-optic sampling setup is fed into a first lock-in amplifier, referenced to the modulation driving the photoconductive switch (at $f_{\text{ref}1} = 20$ kHz). The voltage reported by this lock-in amplifier (V) was sent to a second lock-in amplifier, referenced to the frequency of optical chopping ($f_{\text{ref}2} = 160$ Hz), allowing the change ΔV in V to be measured. As the voltage V recorded in electro-optic sampling is proportional to the THz electric field strength T , the relative change in transmission is $\Delta T/T = \Delta V/V$.

an unamplified Ti:Sapphire oscillator, this transmission change is typically small – of the order of 1 part in 1000. Therefore, the sample pump beam was modulated mechanically via an optical chopper, at around 150 Hz. The change in the THz electric field occurring at this frequency was then recorded, using a second lock-in amplifier (referenced to the chopper), as shown in the circuit diagram of Figure 3.3. The change in the transmitted electric field ΔT between the pump’s ‘on’ and ‘off’ states was thus measured, and can be related to the sample’s conductivity, as described in Section 3.2.2.

There are a couple of issues of note about the sample and the geometry of the spectrometer. The THz beam waist at the sample should be smaller than that of the sample pump beam (P2), so that the probed charge density is uniform. This can be achieved by ensuring that the pump is not focussed at the sample. Ideally, to look at a well-defined carrier density, a charge distribution that is uniform in depth into the sample is required. This constraint requires the sample’s thickness to be

less than its absorption depth, typically $1/\alpha \sim 1\text{ }\mu\text{m}$ in inorganic semiconductors. In order to study the dynamics of photoexcited carriers in THz devices, however, this requirement should not be fulfilled – in thick semiconductors (required for high resolution spectrometers, Section 2.2.4) carrier diffusion into the bulk material can play a significant role (Sections 3.3.2 and 4.5).

Two classes of experiment can be performed using the setup of Figure 2.1. At a fixed sample pump delay time, scanning the THz delay line allows the medium's conductivity to be determined over the THz frequency range by recording the transmission change. If this is done at a number of different delay times before and after the arrival of the sample pump pulse, then the dynamical change in the frequency-dependent conductivity $\sigma(\omega)$ can be measured. The comparison of $\sigma(\omega)$ with a model of the carrier dynamics in the sample often yields invaluable insights into charge transport (Section 1.3.2 and references therein). Alternatively, if the THz delay line is set to the peak of the THz electric field, and the sample pump beam delay is altered, then the resulting transmission change is a measure of the conductivity averaged over the range of frequencies in the THz probe pulse – this is the approach adopted herein.

3.2.2 Calculating the conductivity

An expression is now derived for the conductivity $\sigma(\omega)$ of photoexcited carriers in terms of the change in the transmitted terahertz electric field. According to Beer's Law, the initial density $N(t = 0)$ of photoexcited carriers decays exponentially with depth z into the semiconductor, with a distribution of the form

$$N(z) = N_0 e^{-\alpha z}, \quad (3.4)$$

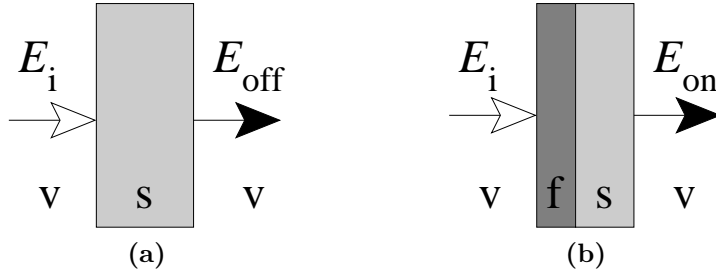


Figure 3.4: The THz electric field after transmission through (a) unexcited and (b) photoexcited sample are denoted respectively E_{off} and E_{on} , and can be related to the incident electric field E_i as in Equations 3.5 and 3.6. The labels v, s and f correspond to vacuum, sample and the photoexcited thin-film.

where the initial surface charge density is N_0 , and α is the absorption coefficient. The photoexcited region can therefore be modelled as a thin film of thickness $\delta = 1/\alpha \sim 1 \mu\text{m}$.

Denoting the electric field before propagation through the sample as E_i , and the field after transmission through the sample when the pump beam is and is not blocked as E_{off} and E_{on} respectively (Figure 3.4), standard boundary condition considerations result in

$$E_{\text{off}} = t_{\text{vs}}t_{\text{sv}}e^{in_s\omega d/c} \text{FP}_{\text{vsv}} E_i, \quad (3.5)$$

$$E_{\text{on}} = t_{\text{vf}}t_{\text{fs}}t_{\text{sv}}e^{in_f\omega\delta/c}e^{in_s\omega(d-\delta)/c} \text{FP}_{\text{vfs}} \text{FP}_{\text{fsv}} E_i, \quad (3.6)$$

where the Fresnel transmission coefficients are $t_{ij} = 2n_i/(n_i + n_j)$, and the subscripts v, s, and f denote respectively vacuum, the unexcited semiconductor and the excited thin-film. The Fabry-Perot terms FP_{ijk} (Equation 2.4) account for multiple internal reflections within medium j , and since the reflections produced by the optically-thick substrate can be removed by windowing the time-domain data (Figure 2.4) then $\text{FP}_{\text{vsv}} = \text{FP}_{\text{fsv}} = 1$. In order to evaluate FP_{vfs} we assume that the thin-film limit

applies, namely that

$$n_f \delta\omega / c \ll 1 \Rightarrow e^{in_f \delta\omega / c} = 1 + in_f \delta\omega / c. \quad (3.7)$$

This is equivalent to assuming that all internal reflections from the thin-film overlap in the time-domain (a situation that was demonstrated experimentally for gold thin-films, which have a significantly greater conductivity than found in most semiconductors – see Section 2.4.3). This produces

$$\text{FP}_{\text{vfs}} = \sum_{p=0}^{\infty} [r_{\text{fs}} r_{\text{fv}} e^{2in_f \omega \delta / c}]^p = \frac{1}{1 - r_{\text{fs}} r_{\text{fv}} e^{2in_f \omega \delta / c}}. \quad (3.8)$$

Defining the function $T(\omega) = E_{\text{on}}/E_{\text{off}}$, and using Equations 3.5-3.8 and the relationship between the conductivity σ and dielectric function ϵ_f of the thin film ($\epsilon_f = \epsilon_\infty + i\sigma/\epsilon_0\omega$, Appendix A.1) results in

$$\sigma(\omega) = \frac{1 + n_s}{Z_0 \delta} \left(\frac{1}{T} - 1 \right), \quad (3.9)$$

where the further assumption that $n_f \gg n_s$ was made. Experimentally, the amplitude of the change in transmitted electric field between the pump on and off states is measured, i.e. $\Delta E = |E_{\text{on}} - E_{\text{off}}| = E_{\text{off}} - E_{\text{on}}$ (since $E_{\text{on}} < E_{\text{off}}$ due to the additional absorption and reflection of THz radiation when the pump beam is on), and thus $1/T - 1 = \Delta E/E_{\text{on}}$. When the change in transmission is small, as is the case at the photoexcited carrier densities herein, $E_{\text{on}} \sim E_s = (E_{\text{on}} + E_{\text{off}})/2$, and therefore the conductivity is proportional to the relative transmission change:

$$\sigma(\omega) = \frac{1 + n_s}{Z_0 \delta} \frac{\Delta E}{E_s}. \quad (3.10)$$

The conductivity has contributions from both electrons and holes, and in general is related to the mobility μ and carrier density N of the two species via

$$\sigma = N_e e \mu_e + N_h e \mu_h. \quad (3.11)$$

In practice the conductivity is dominated by the contribution of electrons with a low excess energy above band-gap, such that they are close to the Γ -point of the Brillouin zone (“in the Γ -valley” – Figure 3.1). Such electrons are significantly more mobile than electrons higher in the band (e.g. in the L or X-valley), or holes. The approximation that $\sigma = N_e e \mu_e$ is therefore valid for the III-V semiconductors.

It is possible to distinguish directly between the contributions of the free carrier density and of the mobility to the conductivity, if free-carrier absorption of THz radiation produces a plasma frequency in the THz range. Fitting the frequency-dependent transmission using the Drude-Lorentz model (Equation 2.10) will give the carrier density, as long as the charge density probed by the THz radiation is uniform (Section 3.2.1). However, the initial carrier density can also be estimated from the known pump pulse fluence, the reflective losses on entering the semiconductor, and the absorption coefficient. The mobility of photoexcited carriers can thus be extracted from the peak of the conductivity, and is assumed to be constant with time after photoexcitation. Any decay in the conductivity with time is therefore due to a reduction in the number density of photoexcited electrons. The electron-hole recombination rate and carrier-trapping rates typically exhibit exponential decays, i.e. a time dependence $N(t) = N_0 \exp(-t/\tau)$, where $N(t)$ can be obtained directly from the experimental data via

$$N(t) = \frac{1 + n_s}{Z_0 e \mu_e \delta} \frac{\Delta E(t)}{E_s(t)}. \quad (3.12)$$

3.2.3 Comparison with other time-resolved techniques

Within the field of ultra-fast optoelectronics there are a number of other techniques based on pulsed laser systems that can be leveraged to investigate carrier dynamics on

picosecond timescales [106]. Here, they are briefly compared with optical-pump THz-probe spectroscopy. The temporal resolution of all of these techniques is ultimately limited by the duration of the exciting laser pulse.

- *Photoluminescence spectroscopy* [107]. The radiative recombination of a photoexcited electron and hole pair generates a photon, often at a lower energy than the excitation energy. The spectrum of this photoluminescence can be recorded via techniques such as up-conversion, giving direct access to information about energy transfer and carrier recombination mechanisms in a material [108]. However, data can be difficult to obtain for materials that don't photoluminesce efficiently, or degrade under photoexcitation. The role of non-radiative recombination centres, such as carrier traps in ion-implanted semiconductors, is harder to determine directly than with THz-TDS.
- *Time-resolved absorption/reflectivity* [109]. A photoexcited carrier distribution is created by an intense above-band edge pulse of light, and then probed by a weaker pulse either at the same frequency, or below the absorption edge. The change in the intensity of the probe beam reflected from the sample (or transmitted through it, for thin samples) is recorded. By delaying the relative arrival time of the pump and probe pulse, the change in reflectivity with time can be obtained, providing information about the dynamical changes occurring during and after photoexcitation. Time-resolved reflectivity is typically used to assess the lifetimes of ultrafast semiconductors, with changes to the reflectivity often ascribed to carrier trapping [94]. Unfortunately, the interpretation of such data is complicated by three competing contributions to the reflectivity

change: bandgap renormalisation, free carrier absorption and bandfilling effects [105; 109; 110]. The first two of these effects create a negative reflectivity change (for GaAs excited above bandgap), while the latter produces a positive reflectivity change [105], making the analysis of reflectivity curves complex. Additionally, the wavelength of both pump and probe pulses is restricted to the frequency range accessible using harmonics of the laser's fundamental mode, i.e. typically to the near-IR, visible and UV. The probe itself can therefore photoexcite carriers (by two photon or two-step absorption if below the bandgap energy), further complicating data analysis.

- *Time-resolved Raman spectroscopy* [106] measures the decay in the population of a low-frequency mode (typically an optical phonon mode) after photoexcitation, witnessed by the inelastic scattering of a probe pulse from excitations created by a stronger pump pulse. A suitably chosen polarisation analyser prevents the light scattered from the pump pulse from entering the detector. Different low-frequency excitations can be created and monitored via time-resolved Raman spectroscopy than can be accessed via THz spectroscopy, owing to the selection rules for inelastic scattering (e.g. non-equilibrium LO-phonons in GaAs [111]).

In summary, optical-pump THz-probe spectroscopy can measure the complex refractive index or the conductivity of a medium, and often provides more direct experimental access to the properties of a material than is possible with other time-resolved techniques.

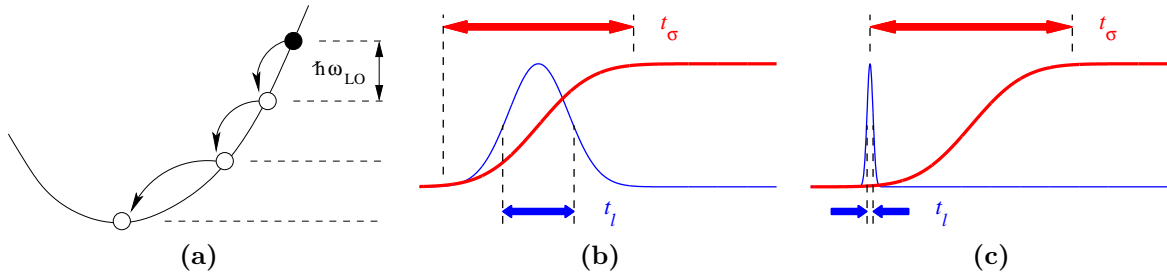


Figure 3.5: (a) Intravalley scattering of a photoexcited electron by the emission of an LO phonon. A number of scattering events are required to reach the minimum of the conduction band. (b) Incident laser pulse intensity (blue) and photoexcited conductivity σ (red) as a function of time. When the laser pulse duration t_l is larger than the scattering time t_s , the timescale t_σ for the rise in σ follows the laser pulse. (c) Conversely, when $t_l < t_s$ the response of the semiconductor limits the rise in conductivity, a situation obtained when photoexciting high above the direct bandgap energy E_Γ .

3.3 Semi-insulating semiconductors

The time-resolved conductivity measurements that can be obtained using optical-pump THz-probe spectroscopy provide direct insights into the ultrafast dynamics of photoexcited carriers in semiconductors, knowledge that is essential to understand properly the emission of THz radiation from photoexcited semiconductors. In this section results from optical-pump THz-probe spectroscopy of semi-insulating semiconductors are presented. The findings are applied to the photoconductive emission of THz radiation throughout Chapter 4.

3.3.1 Photoexcitation dynamics

If a photon incident on a semiconductor has an energy E_γ exceeding its bandgap energy a valence band electron can be excited into the conduction band, increasing the material's conductivity σ . For a direct bandgap semiconductor with Γ -valley energy gap E_Γ the photoexcited electron has an excess kinetic energy $E_{ex} = E_\gamma - E_\Gamma$, which it

begins to lose owing to the various carrier scattering mechanisms ([82], Section 4.2.2) until it reaches the bottom of the band. This situation is illustrated in Figure 3.5a for electron-LO phonon scattering – the time taken for an electron to scatter to the bottom of the band is denoted t_s .

The timescale t_σ of the rise in conductivity for pulsed excitation is determined by a combination of the duration t_l of the laser pulse and t_s . When $t_l > t_s$ the rise in conductivity will follow the laser pulse (Figure 3.5b). However, when $t_l < t_s$, the scattering time can dominate the conductivity change (Figure 3.5c). Such a situation is obtained when electrons are photoexcited high within the conduction band (large E_{ex}), into states with high effective masses (low mobility). In this case the conductivity of a photoexcited electron is initially low, but as it scatters it loses energy, falling lower in the conduction band (towards the Γ point). Since scattering events occur in a finite time, typically a few 100 fs, it takes a measurable period for the initial photo-carrier distribution to equilibrate with the lattice.

Optical-pump terahertz probe spectroscopy is an ideal tool to investigate photoexcitation dynamics in inorganic semiconductors, owing to the ability to record the conductivity on ultra-short timescales. Past work includes a study of GaAs excited at 2.0 eV, in which the rise in conductivity was seen to occur over 3 ps [112], owing to the time taken for inter- and intra-valley scattering towards the Γ valley bandgap energy (1.42 eV). Additionally, by probing the conductivity of photoexcited GaAs with mid-IR pulses (8-30 THz) emitted from GaSe, Huber *et al.* reported that the medium only exhibits a Drude response after a few 100 fs, under excitation at 1.55 eV with 10 fs laser pulses. This may be a direct demonstration that the collective behaviour characteristic of quasiparticles can only occur after the electron distribution, which has

Semiconductor	Description of sample
GaAs	Semi-insulating (SI) GaAs, 0.3 mm thick.
In _{0.53} Ga _{0.47} As	2.5 μ m thick In _{0.53} Ga _{0.47} As separated by a 300 nm undoped InP buffer layer from a 0.3 mm SI-InP (Fe doped) substrate.
InAs	500 nm bulk InAs layer separated by a 150 nm undoped GaAs buffer layer from a 0.3 mm SI-GaAs substrate.

Table 3.1: Details of samples used in the study of photoexcitation dynamics reported in Figure 3.6.

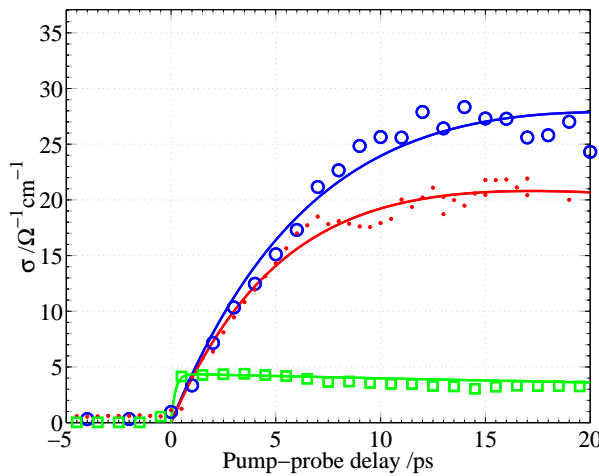


Figure 3.6: Time-resolved conductivity of GaAs (squares), In_{0.53}Ga_{0.47}As (dots) and InAs (circles) measured using 1 kHz amplifier-based optical-pump THz-probe setup. The conductivity reaches a maximum at a later time when the excess electron energy is increased. The solid lines are guides to the eye.

a broad energy distribution owing to the wide spectrum of a 10 fs pulse (Figure 2.2), has cooled somewhat.

In this section the photoexcitation dynamics of In_{0.53}Ga_{0.47}As and InAs (excited at large excess carrier energy E_{ex}) are compared with that of GaAs. Using the methods outlined above, the time-resolved conductivity $\sigma(t)$ was measured at time t after photoexcitation. Incident pulses of duration 40 fs and central wavelength 800 nm were provided by a 1 kHz repetition rate, amplified Ti:Sapphire laser (Section 2.2.1). The use of a low repetition rate laser system was necessary to avoid the influence of elec-

trons with nanosecond lifetimes, as discussed in Section 3.3.2. The samples' details are provided in Table 3.1. In Figure 3.6 $\sigma(t)$ is reported for semi-insulating GaAs, $\text{In}_{0.53}\text{Ga}_{0.47}\text{As}$ and InAs photoexcited at 800 nm (an energy of $E_\gamma = 1.55\text{ eV}$). It can be seen that the time taken for the conductivity to reach a maximum increases from $t_\sigma < 1\text{ ps}$ for GaAs, to 10 ps for $\text{In}_{0.53}\text{Ga}_{0.47}\text{As}$, up to 15 ps for InAs. This increase is due to photoexcited electrons having a larger kinetic energy for a lower bandgap energy semiconductor: the Γ valley bandgap is at 1.42 eV, 0.73 eV and 0.35 eV for GaAs, $\text{In}_{0.53}\text{Ga}_{0.47}\text{As}$ and InAs respectively.

The change in t_σ can be understood using the following simple model, described by Kash *et al.* [111]. If a non-equilibrium carrier scatters with a characteristic lifetime τ , then the time taken for the carrier distribution to equilibrate with the lattice is

$$t_{\text{cool}} = \tau N_{\text{events}} = \tau \frac{E_{\text{ex}}}{E_{\text{LO}}}, \quad (3.13)$$

where the number of scattering events N_{events} is the excess carrier energy $E_{\text{ex}} = E_\gamma - E_\Gamma$ divided by the energy lost per event, which is E_{LO} if electron-LO phonon scattering is the dominate mechanism. τ for LO-phonon scattering can be determined by time-resolved Raman spectroscopy [111], or it can be calculated for the known electron density (Section 4.4.2). Taking $\tau = 0.2\text{ ps}$ results in $t_{\text{cool}} = 0.7\text{ ps}$ for GaAs, 5.0 ps for $\text{In}_{0.53}\text{Ga}_{0.47}\text{As}$ and 8.0 ps for InAs. This model thus reproduces the observed trend in t_σ , although the scattering mechanism may be intervalley rather than intravalley.

3.3.2 Surface states and diffusion

A well known issue in the development of semiconductor devices is the poor quality of the surface. Oxides and dense concentrations of dangling ionic bonds can lead

to electronic states within the semiconductor's bandgap that create a large surface recombination rate. The quality can be improved markedly by chemical treatments that remove the surface oxide layer, and passivate the semiconductor/air interface [113; 114]. While passivation has been demonstrated to improve the performance of III-V laser diodes[115], solar cells[116] and bipolar transistors[113], discussion with regard to sources of terahertz (THz) radiation has been limited to Schottky diode multipliers [3], which produce continuous wave radiation at typically $< 150\text{ GHz}$. In photoconductive emitters of THz radiation the photoexcited carrier distribution lies within $\sim 1\mu\text{m}$ of the surface (owing to the absorption depth): THz emission may therefore be expected to be affected significantly by surface defects.

In this section the influence of surface states on the time-resolved conductivity of photoexcited electrons in GaAs is discussed. The effect that these defects have on THz emission is detailed in Section 4.6.

The surfaces of samples of semi-insulating (SI) GaAs and InSb [both (100) orientation, with dark resistivities of $1.5\times 10^8\Omega\text{cm}^{-1}$ and $1.2\times 10^{-1}\Omega\text{cm}^{-1}$ respectively] were etched with 5:1:1 $\text{H}_2\text{SO}_4 : \text{H}_2\text{O}_2 : \text{H}_2\text{O}$, and subsequently passivated by dipping in $(\text{NH}_4)_2\text{S}$ for 10 minutes.[114] A reference set of samples were made from the same wafers, without the passivation step, and were allowed to oxidize completely in air.

In Figure 3.7 the time-resolved conductivity of the passivated sample is compared with that of the reference. At zero pump-probe delay the conductivity increases rapidly owing to the photogeneration of electrons. After increasing to its maximum value, the conductivity begins to decay as a result of mechanisms that alter the carrier concentration: these include carrier recombination, trapping, scattering and diffusion. The decay in conductivity is non-exponential: at early delay times recombination at surface

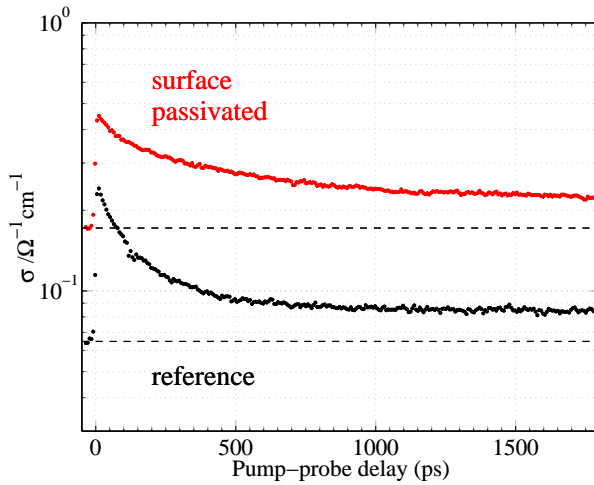


Figure 3.7: Time-resolved conductivity of passivated (top) and reference (bottom) GaAs samples, as measured via optical-pump THz-probe spectroscopy. The dotted lines indicate a non-zero conductivity before the pump pulse arrives, owing to the bulk lifetime ($\tau_b = 15$ ns) exceeding the repetition period between laser pulses (13.3 ns).

defect sites significantly depopulates the electron concentration. At later delay times ($\gtrsim 100$ ps) the carrier distribution has had time to diffuse into the bulk, reducing the role of surface recombination [117]. It can be seen that the surface passivated sample has a larger initial conductivity than of the etched sample, and a longer initial decay time constant. As the incident photon flux was identical for the two samples, this increase in conductivity can be attributed to a $1.9\times$ larger initial electron mobility μ . An exponential fit to the initial decay produces a time constant of $\tau = 389$ ps for the passivated sample, twice that of the etched sample ($\tau = 192$ ps), and consistent with $\mu = e\tau/m^*$. The passivation step can therefore be directly seen to produce a surface with fewer recombination centres.

Following Beard *et al.* [117], the non-exponential shape of the decay in σ can be modelled via a solution to the 1D diffusion equation. With a bulk lifetime $\tau_b = 15$ ns (taken from the limit of the decay in Figure 3.7), good agreement is found with the measured σ when the surface recombination velocity $S_0 = 1.2 \times 10^6 \text{ cm s}^{-1}$ for

the etched reference, and $S_0 = 2.0 \times 10^5 \text{ cm s}^{-1}$ for the surface passivated sample. These values correspond well to those in the literature for etched and passivated GaAs surfaces [113] (however S_0 can be further reduced by improved surface treatments to $S_0 = 10^3 \text{ cm s}^{-1}$ [114]). The Shockley-Read-Hall model (Section 3.1.4) predicts that $S_0 = n_t v \Sigma$ for a surface trap density n_t , scattering cross-section Σ and carrier velocity v . Assuming that v and Σ are identical before and after passivation, the trap density in the passivated sample is 17% of that in the etched sample.

At large pump-probe delay times ($\gtrsim 1000 \text{ ps}$) the decay in conductivity slows, because the carrier distribution has diffused into the bulk. The bulk lifetime (15 ns) exceeds the repetition period between laser pulses (13.3 ns), resulting in a non-zero conductivity at negative pump-probe delays. The consequences of this for THz emission are discussed in Section 4.5, both with regard to THz photonic devices containing semi-insulating GaAs, and using the specific case of $\text{In}_{0.53}\text{Ga}_{0.47}\text{As}$ surface emitters. The carrier lifetime in inorganic semiconductor crystals tends to increase at reduced temperature (as is discussed in the following section), making this effect more pronounced.

3.3.3 Temperature dependance of mobility

Recording the conductivity of a material as a function of temperature can allow the accuracy of charge transport models to be evaluated. The Hall effect, in which a voltage is induced perpendicular to the directions of the applied magnetic field and current flow, is a standard technique that provides experimental access to the d.c. mobilities of inorganic semiconductors. The study of the temperature dependence of the mobility of photoexcited charge carriers via THz-TDS is highly complementary to Hall mea-

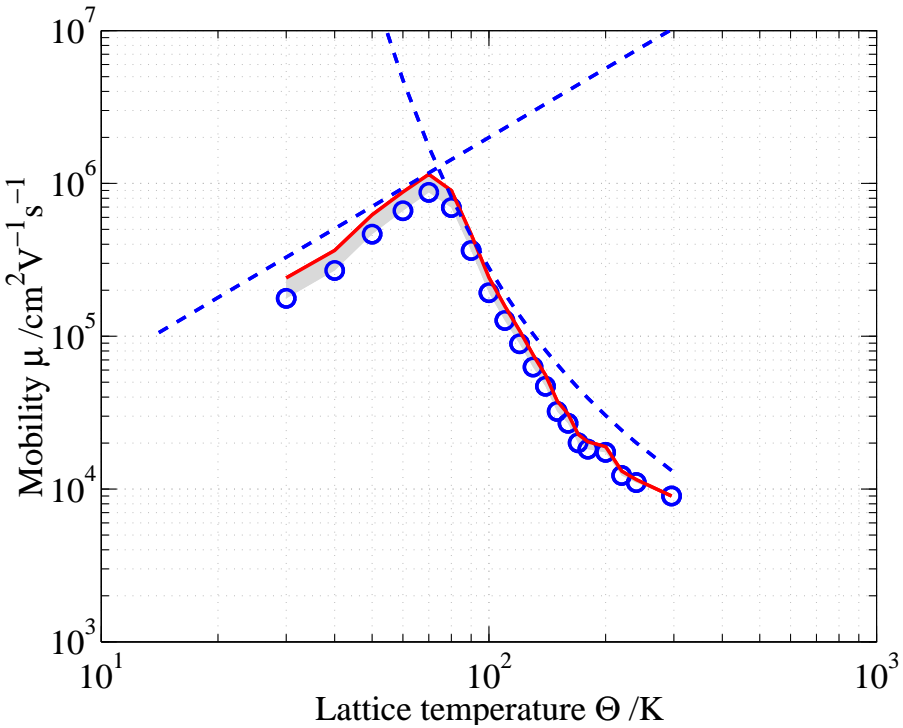


Figure 3.8: Mobility of photoexcited semi-insulating GaAs as a function of lattice temperature, extracted from the conductivity at 1 THz, 30 ps after the pump pulse. The circles indicate the mobility assuming a constant carrier density, and the solid line shows the mobility μ after correcting for the change in photoexcited carrier density (the shaded area marks the change in mobility that this introduces). The dotted lines plot the theoretical mobilities for the principal scattering mechanisms: at a low lattice temperature Θ carrier-carrier scattering ($\mu \propto \Theta^{3/2}$) dominates, while at high Θ carrier-phonon scattering governs the mobility.

surements, with the advantage of providing information over a range of frequencies, and for carrier distributions far from thermal equilibrium. Temperature-dependant time-resolved conductivity measurements have enabled charge transport mechanisms to be investigated in a number of materials of contemporary scientific and technological interest, including thin-films of pentacene [39] (an organic semiconductor), BSSCO [36] (a high-temperature superconductor), and InGaAs quantum dots [46].

The time-resolved conductivity of photoexcited SI-GaAs was measured as a function of the lattice temperature Θ , using the optical-pump THz-probe setup described

above (Section 3.2.1), with the addition of an Oxford Instruments microstat to cool the sample. The motivation for this experiment was to test the cryostat, and to establish the procedure for future temperature-dependant studies (Section 6). Unfortunately, the ageing cryostat used was unable to cool below 30 K, as measured by two different temperature sensors. However, the differential transmission $\Delta T/T$ was obtained over the temperature range 30 – 300 K, and was used to extract the conductivity $\sigma(\omega)$ of photoexcited electrons, as described in Section 3.2.2. The temperature dependence of the electron mobility is as shown by the circles in Figure 3.8, obtained from $\sigma(\omega/2\pi = 1 \text{ THz})$ at a time 30 ps after the sample pump pulse, and assuming a mobility at room temperature of $8800 \text{ cm}^2 \text{V}^{-1} \text{s}^{-1}$ and a constant photoexcited carrier density. However, as the temperature is reduced the bandgap energy of GaAs increases slightly, causing the photoexcited carrier population to decrease. The effect of this was included by reducing the carrier density according to the reduction in the fraction of above-bandgap photons (obtained from the spectrum of the pump pulse, Figure 2.2), with the known temperature dependance of the bandgap [118], producing the solid line.

As illustrated by Figure 3.8, the mobility of photoexcited electrons increases as the sample is cooled from room temperature. The lattice's temperature plays a key role in determining the mobility, because the electron distribution has fully equilibrated with the lattice by 30 ps after the pump pulse. The mobility peaks at 70 K, before decreasing at lower temperatures. The change in mobility can be reproduced well by the known dominant scattering mechanisms, plotted as dashed lines in Figure 3.8. At low temperatures ($\Theta \ll 70 \text{ K}$) carrier-carrier scattering [82] governs the mobility, with a characteristic $\mu \propto \Theta^{3/2}$ dependence. (In d.c. Hall measurements of the equilibrium

mobility carrier-impurity scattering dominates μ at low temperatures, which also has a $\mu \propto \Theta^{3/2}$ dependence). At higher temperatures ($\Theta \gg 70\text{ K}$) the mobility decreases with temperature owing to an increasing carrier-optical phonon scattering rate - the theoretical curve in Figure 3.8 was plotted using the formula given in Ref. [119]. These data provide a firm demonstration of the potential of temperature-dependent studies using time-resolved THz spectroscopy, while reproducing a well-known textbook result for equilibrated electrons in inorganic semiconductors.

3.4 Low-temperature-grown GaAs

The growth of semiconductors at a reduced temperature, followed by an annealing step, creates a material suitable for ultrafast optoelectronic devices. In this section the time-resolved conductivity of a typical $1\text{ }\mu\text{m}$ -thick low-temperature (LT) grown GaAs sample is reported. Similar data were obtained on a number of LT-GaAs samples grown at the University of Leeds, and at the University of Manchester.

The conductivity of the photocarrier distribution in LT-GaAs was determined via the technique outlined above (Section 3.2.1), and is compared with that of SI-GaAs excited under the same pump fluence in Figure 3.9a. The lifetime of the LT-GaAs sample is initially 7.2 ps, compared with 384 ps for SI-GaAs. By comparing the initial conductivity of LT-GaAs with that of SI-GaAs, and assuming that the photoexcited carrier density is the same for both samples, the mobility of the LT-GaAs layer can be calculated as 29 % of that of SI-GaAs. This is far larger than would be expected with a simple prediction from the ratio of the lifetimes and $\mu = e\tau/m^*$, which yields 2 %. The discrepancy can be attributed to the ultrafast trapping of photoexcited carriers

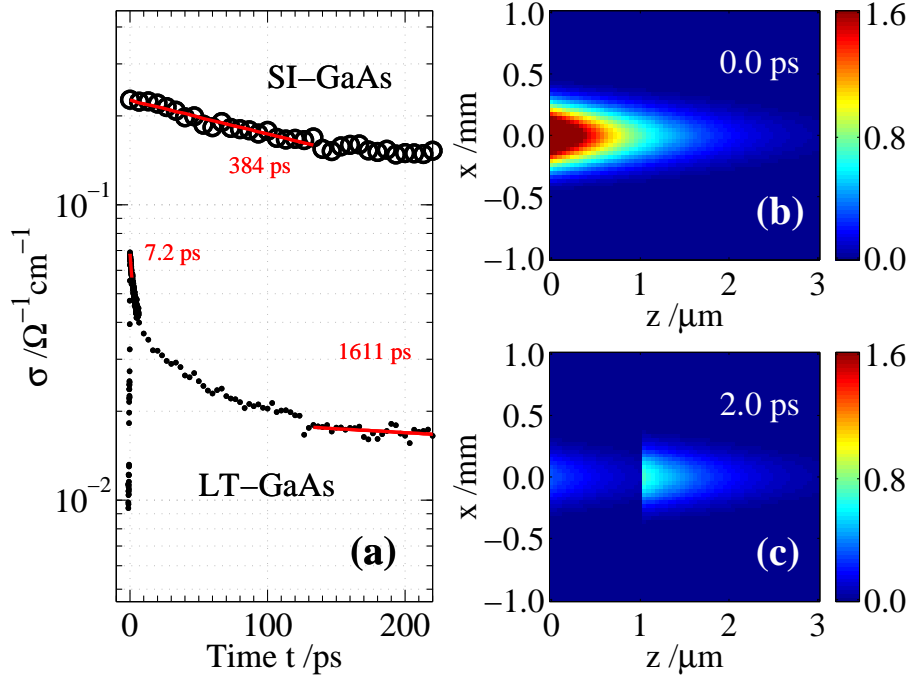


Figure 3.9: (a) Time-resolved conductivity of LT-GaAs (dots) and SI-GaAs (circles), with single-exponential fits (solid lines). The modelled evolution of the photoexcited electron distribution in a $1 \mu\text{m}$ -thick LT-GaAs layer on a SI-GaAs substrate is shown at (b) 0.0 ps and (c) 2.0 ps after the arrival of the pump pulse. The charge distribution is assumed to be Gaussian in the x -direction, and to decay exponentially in the z -direction according to the absorption coefficient. The peak carrier concentration is indicated in red, and is $1.6 \times 10^{17} \text{ cm}^{-3}$. An electron lifetime of 1 ps was assumed in the LT-GaAs layer, and 1 ns in SI-GaAs. The long-lived carriers in the SI-GaAs dominate the conductivity response of the material on a long time scale.

within the LT-GaAs layer: electrons are mobile, yet short-lived.

The decay in conductivity in Figure 3.9a is non-exponential, with a lifetime that lengthens at larger pump-probe delay times, tending to 1.6 ns at $t > 150 \text{ ps}$. This is a result of the LT-GaAs layer being only $1 \mu\text{m}$ thick: the absorption depth in GaAs is $0.8 \mu\text{m}$ at 800 nm, and 30 % of carriers are photoexcited within the SI-GaAs substrate. Figures 3.9b-c indicate this situation by plotting the expected carrier distribution using a simple model. While electrons decay rapidly within the LT-GaAs layer, electrons within the bulk SI-GaAs substrate have lifetimes exceeding 1 ns, creating the long-lived

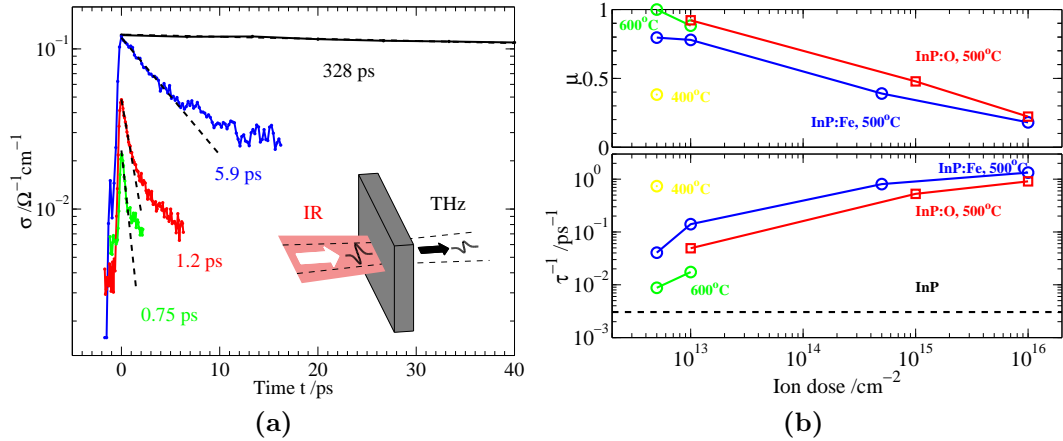


Figure 3.10: (a) Conductivity of photoexcited electrons in the InP:Fe⁺ samples annealed at 500°C, obtained using the method outlined in the text. (b) Top: The mobility of the various samples of InP:Fe⁺ (circles) and InP:O (squares) is shown as a function of the higher energy ion dose, relative to that of unimplanted InP, at different annealing temperatures. Bottom: Inverse of the lifetime of the initial decay in conductivity. The inverse lifetime of unimplanted InP is shown by the dotted line.

tail to the conductivity decay for the LT-GaAs sample. Because of the influence of the electrons in GaAs, the extracted lifetime (7 ps) should be treated as an upper limit of the trapping time in the LT-GaAs layer. In Section 4.5 the influence of long-lived electrons upon THz emission from photoconductive switches made on a 1 μm-thick LT-GaAs sample is discussed.

3.5 Ion-implanted InP

A wealth of information about the defect centres in ion-damaged semiconductors, and their influence on the ultra-fast dynamics of photoexcited carriers, can be obtained from time-resolved conductivity measurements. This is now illustrated using optical-pump THz-probe measurements on O- and Fe-implanted InP [97].

Dual-energy (0.8 and 1.8 MeV) implants of Fe⁺ ions were performed at room tem-

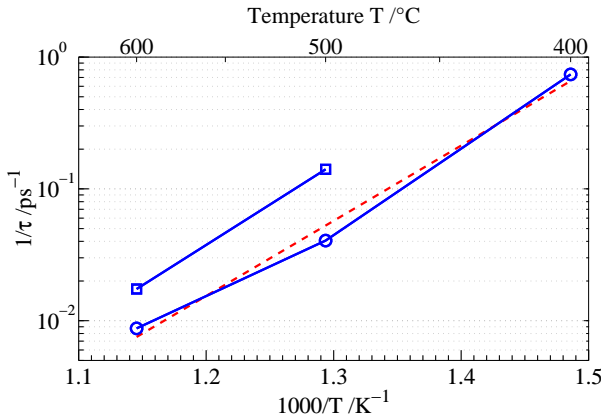


Figure 3.11: Arrhenius plot for InP:Fe⁺ samples (inverse lifetime against inverse annealing temperature). The gradient of the straight line fit is E_a/k_B , from which the activation energy for thermal annealing of the ion-implanted defect centres is $E_a = 1.20 \pm 0.06$ eV.

perature, for different ion doses. The highest dose for the 2.0 MeV implant was $1 \times 10^{16} \text{ cm}^{-2}$, and the other samples had 1/20th and 1/1000th of this dose. The 0.8 MeV implants were at 25% of the corresponding 2.0 MeV dose. For the InP:O⁺ samples three implants (250 keV, 0.6 MeV and 1.2 MeV) were used, producing similar damage. A post-implantation annealing step (for 30 minutes, typically at 500 °C) allowed the resistivity to recover. The damage (vacancy) profile of both InP:Fe⁺ and InP:O⁺ was calculated using the SRIM software [99], and extends over the absorption depth of 800 nm photons.

The time-resolved conductivity of photoexcited electrons in ion-implanted InP:Fe⁺ was measured (Figure 3.10a). As the dose increases, the lifetime of photoexcited electrons decreases from the unimplanted case (330 ps) to 0.75 ps at the largest dose levels. Similar transients (not shown) were obtained for the InP:O⁺ samples.

3.5.1 Activation energy for annealing traps

The dependence of the carrier lifetime τ on the annealing temperature T_{ann} can be used to extract the activation energy E_a for thermal defect removal, using the relationship:

$$\frac{1}{\tau} = \frac{1}{\tau_0} e^{E_a/k_B T_{\text{ann}}}. \quad (3.14)$$

The gradient of an Arrhenius plot (log of rate $1/\tau$ against $1/T_{\text{ann}}$) can therefore be used to obtain E_a , as illustrated in Figure 3.11. For InP:Fe⁺ this gives $E_a = 1.20 \pm 0.06$ eV, in excellent agreement with the value of $E_a = 1.27 \pm 0.05$ eV obtained from a similar study using the photoluminescence lifetime [97]. This energy is comparable to that to remove the phosphor vacancy, suggesting that this is the principal defect site in InP:Fe⁺. The time-resolved optical conductivity and photoluminescence data have the same behaviour with T_{ann} , which indicates that the dynamics of photoexcited carriers in ion-damaged InP is dominated by radiative recombination at phosphor vacancies, rather than non-radiative carrier trapping.

3.5.2 Defect concentration

Additionally, the concentration of defect sites in ion-implanted InP can be deduced from the measured lifetimes, via a simple model for the motion of photoexcited electrons, which is developed here. For diffusing particles undergoing Brownian motion one can write the mean diffusion length as $\langle x \rangle = \sqrt{Dt}$. Equating the time t during which the electron can undergo diffusion to the photoexcited carrier lifetime τ , and using the Einstein relation for the diffusion coefficient ($D = \mu k_B T/e$) results in

$$\langle x \rangle = \sqrt{\frac{\mu \tau k_B T}{e}}. \quad (3.15)$$

It should be noted that this treatment will only be valid for carrier transport in an amorphous medium (i.e. at high damage doses), when hopping is the principal conduction mechanism. At lower doses the transport is increasingly band-like, and the mobility is dominated by carrier-carrier and carrier-phonon scattering mechanisms rather than by trapping or scattering at defects (Sections 3.3.2, 3.3.3 and 4.4.2). Since $\langle x \rangle$ is the mean distance to the nearest scattering site, the concentration of vacancies can be calculated using $N_{\text{vac}} = 1/\langle x \rangle^3$ and Equation 3.15, yielding

$$N_{\text{vac}} = \left(\frac{e}{\mu k_B T \tau} \right)^{3/2}. \quad (3.16)$$

This results in $N_{\text{vac}} = 5.5 \times 10^{16} \text{ cm}^{-3}$ and $N_{\text{vac}} = 2.3 \times 10^{16} \text{ cm}^{-3}$ for the highest dose InP:Fe⁺ and InP:O⁺ samples, respectively, the damage being greater for the more massive Fe⁺ ions. As may be expected, the values of N_{vac} thus extracted are linearly proportional to the incident dose n_{ion} (Figure 3.12). At a low dose deviations from linearity may arise from the introduction of band-like transport, while at high dose the finite time resolution of the spectrometer (limited by the non-co-linear sample pump geometry used in these data) can increase the recorded lifetime.

When taken in conjunction with the mean vacancy concentration from the SRIM simulations N_{sim} , these values of N_{vac} can be used to calculate the fraction of vacancies remaining after the post-implant thermal annealing step (500°C, 30 minutes) $\eta = N_{\text{vac}}/N_{\text{sim}} = 2.5 \times 10^{-7}$ (Figure 3.12).

3.5.3 Applicability of Shockley-Read-Hall model

If the SRH model is applicable to ion-implanted InP, the dose-dependence of the lifetime would be $\ln 1/\tau \propto \ln N_t \propto \ln n_{\text{ion}}$ (Equation 3.1). Figure 3.10b indicates that

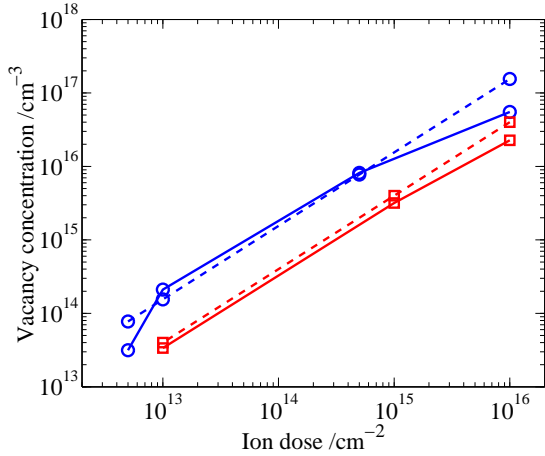


Figure 3.12: Concentration of vacancies in InP:Fe⁺ (circles) and InP:O (squares) calculated from the lifetime and mobility of photoexcited carriers, as outlined in the text. The simulated vacancy concentration from the SRIM software is also shown (dotted lines), assuming that the fraction of vacancies remaining after annealing $\eta = 2.5 \times 10^{-7}$ for both ion species.

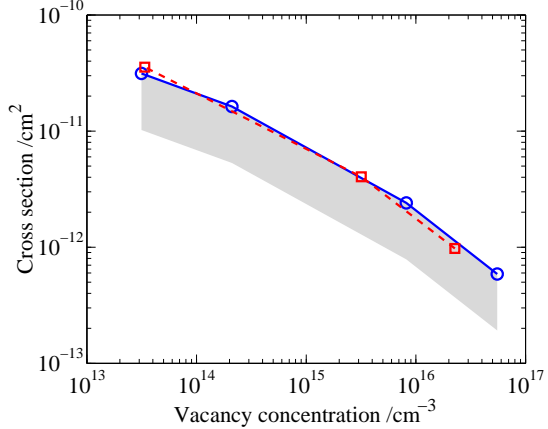


Figure 3.13: Cross-section for electron-vacancy scattering Σ extracted from the SRH model of carrier recombination (Equation 3.1) for InP:Fe⁺ (circles) and InP:O (squares) versus vacancy concentration N_{vac} , assuming an electron distribution in thermal equilibrium with the lattice with velocity v_{th} . The variation of Σ with N_{vac} indicates the invalidity of the SRH model. The shaded area represents the range of cross-section for an electron distribution with average velocity varying from v_{th} up to the velocity due to the excess kinetic energy above bandgap, v_x .

this is not the case. One explanation for this discrepancy may be that the cross-section Σ is dose dependent: indeed on plotting $\Sigma = 1/(N_t \tau v_{\text{th}})$ and taking $N_t = N_{\text{vac}}$ (using the data shown in Figure 3.12) the resultant Σ can be seen to decrease from 10^{-10} cm^{-2} at low vacancy concentration to 10^{-12} cm^{-2} at high vacancy concentration (Figure 3.13). The calculated cross-sections for InP:O⁺ agree with the trend observed for InP:Fe⁺, again indicating that the principal defect site is the same. This change in Σ would imply that the P-vacancies formed at lower vacancy concentrations have a larger size. This result is somewhat counterintuitive, and may be due to the switch from scattering or trapping at defect sites at high vacancy concentration to the increasing

contribution of phonon-scattering to the cross-section at lower N_{vac} , when electrical transport is more band-like.

A further possible reason for the observed disagreement with the SRH model is the assumption during the derivation of Equation 3.1 that the injected carrier distribution is in thermal equilibrium with the semiconductor lattice. For InP photoexcited with 10 fs duration light pulses ($\hbar\omega = 1.4 \leftrightarrow 1.8 \text{ eV}$, see Figure 2.2) this is not the case: the carrier distribution is far from equilibrium on timescales shorter than 1 ps. Equating the carriers' excess energy above the Γ -valley minimum ($\hbar\omega - E_{\Gamma} = 0.21 \text{ eV}$) to the kinetic energy results in a velocity $v_x = \sqrt{2(\hbar\omega - E_{\Gamma})/m^*} = 9.6 \times 10^5 \text{ ms}^{-1}$, more than twice the velocity in thermal equilibrium (Equation 3.2). In practice the velocity of photoexcited electrons will be somewhere between these two extremes, as the distribution relaxes towards thermal equilibrium. The scattering cross-section will therefore be time-dependent, and fall within the shaded area of Figure 3.13.

3.6 Summary

Infra-red pump THz probe spectroscopy was used to measure the time-resolved conductivity of a number of semiconductors, from which the photoexcitation and decay dynamics of photoexcited electrons was inferred. The conductivity was observed to reach a maximum at a time t_{σ} after the arrival of the pump pulse, with t_{σ} increasing as the bandgap of the semiconductor decreased. This was attributed to the time for the non-equilibrium carrier distribution to cool to the (more conductive) bottom of the conduction band. Semi-insulating InP, GaAs, InAs and InGaAs were observed to have long ($> 100 \text{ ps}$) carrier lifetimes. The chemical passivation of the surface of GaAs was

studied, and found to double the surface recombination lifetime and initial conductivity. Finally, shorter carrier lifetimes (< 10 ps) were measured for low-temperature grown GaAs and ion-implanted semiconductors, and related to the Shockley-Hall-Read model.

Chapter 4

Broadband generation of terahertz radiation

“Science is spectral analysis. Art is light synthesis.”
Karl Kraus, 1874-1936.

4.1 Overview

The ‘art’ of generating and detecting single-cycle pulses of light with sub-picosecond duration has enabled numerous spectroscopic studies in the THz frequency range, as reviewed in Chapter 1 and demonstrated throughout this thesis. In this chapter, the emission mechanisms in photoconductive sources of THz pulses are discussed in greater depth. The approach adopted is based on both experiment and simulation; the motivation behind the research was to increase the power and frequency range of THz emitters. Both a simple phenomenological model of THz emission and a carrier dynamics simulation are utilised. The THz radiation from semiconductor surfaces is investigated, and the influence of ion-implantation on the ultrafast trapping and scattering of carriers is determined. Electrons with lifetimes exceeding 1 ns are observed to restrict the radiated THz power from InGaAs surface emitters, and from LT-GaAs photoconductive switches (in the transmission geometry). Finally, the passivation of

GaAs surfaces is examined, via THz surface emission measurements and simulation. A doubling in the power from photoconductive switches fabricated on passivated GaAs is reported.

4.2 Modelling photoconductive THz emission

In the far-field approximation, the THz radiation pulse emitted from a photoconductive source has an electric field given by [33]:

$$\vec{E}_{\text{THz}} \propto \frac{1}{1 + \sqrt{\epsilon}} \frac{\partial \mathbf{J}}{\partial t}, \quad (4.1)$$

where the current density \mathbf{J} within a semiconductor is given by:

$$\mathbf{J} = \sigma \mathbf{E} + eD \nabla N = \sigma \mathbf{E} + e\mu \frac{k_{\text{B}}T}{e} \nabla N. \quad (4.2)$$

Here, only the electron current density has been included: a similar expression holds for the hole contribution, and is neglected owing to their substantially smaller mobility. In the above, σ is the conductivity and \mathbf{E} the applied electric field (either between two metallic contacts, as in a photoconductive switch, or the surface depletion/accumulation field – see Figure 2.3). The diffusion coefficient is $D = \mu k_{\text{B}}T/e$ for electrons with mobility μ at temperature T , and the electron concentration is N .

4.2.1 Phenomenological approach

In order to gain an intuitive handle on THz emission, it is beneficial to consider the following simple model, applied to a SI-GaAs photoconductive switch. The diffusion current's contribution to \mathbf{J} will be negligible, and further postulating that $\epsilon \neq \epsilon(t)$, one can assume therefore that $E_{\text{THz}}(t) \propto \partial J / \partial t = \partial(\sigma E) / \partial t$. The magnitude and

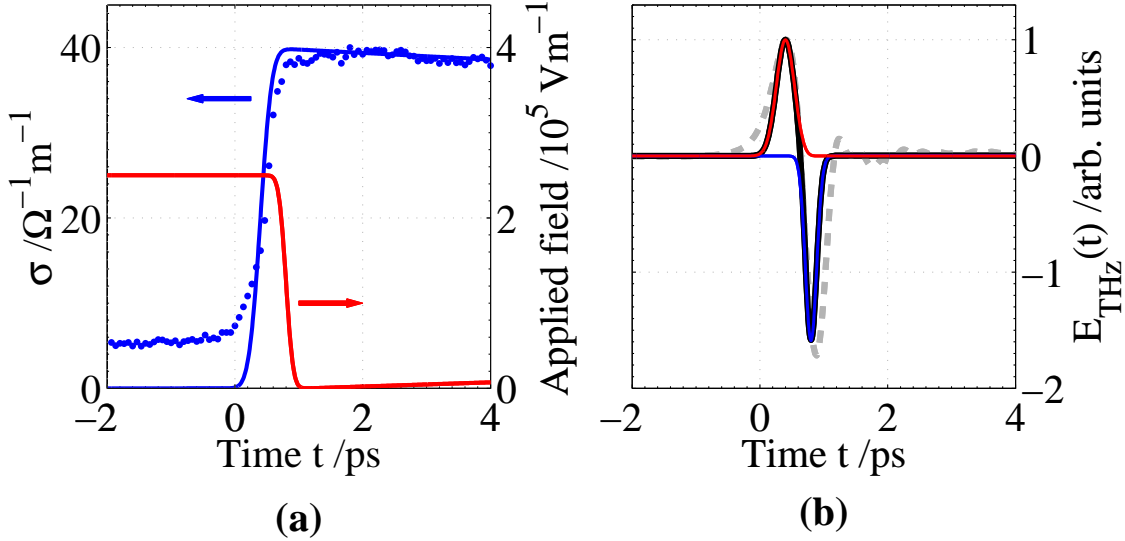


Figure 4.1: Calculated THz emission from a SI-GaAs photoconductive switch, using the simple model described in the text. (a) Typical time-resolved conductivity of SI-GaAs excited at 790 nm by 10 fs, 3 nJ pulses. Experimental data (blue dots) are well fit by an error function multiplied by an exponential decay with lifetime 330 ps (blue line). The non-zero conductivity before the arrival of the pump-pulse at $t = 0$ is a consequence of the long lifetime of electrons in the bulk (Section 3.3.2). Also shown is the expected shape of the applied electric field (red line), which is screened within a time 500 fs to 1 ps after the arrival of the pump pulse at zero time. (b) The modelled THz electric field (black line) is the sum of the $\sigma \partial E / \partial t$ (blue) and $E \partial \sigma / \partial t$ (red) terms, and matches well the typical experimental emission waveform (dotted line).

dynamical change in the conductivity can be taken from optical-pump THz-probe spectroscopy (Chapter 3). The change in σ with time can be modelled with an error function (and E with a complementary error function) multiplied by an exponential decay, as indicated in Figure 4.1a. A value of $E = 2.5 \times 10^5 \text{ Vm}^{-1}$ can be estimated from the applied voltage (100 V) across the gap (400 μm). It is assumed that the applied electric field is completely screened within some time after photoexcitation. This assumption is verified by the 3D solution of Poisson's equation for a photoconductive switch [67]. The screening of E is assumed to begin 500 fs after the arrival of the pump pulse, and to require a further 500 fs. The THz electric field emitted can then

be calculated as $E_{\text{THz}} \propto \sigma \partial E / \partial t + E \partial \sigma / \partial t$, and is plotted in Figure 4.1b. The rapid rise in conductivity produces the positive peak of the THz pulse, while the rapid screening of the applied field creates the negative peak. Good agreement with the measured THz emission from a photoconductive switch is obtained.

In this approach the shape of E was somewhat arbitrarily chosen, and the conductivity was measured experimentally. These two limitations restrict the predictive power of the model, for instance about how THz emission alters when the properties of the semiconductor (e.g. carrier lifetime, bandgap energy) or laser (e.g. pulse duration, wavelength) are altered. To model THz emission accurately and in a fully self-consistent manner requires the treatment of an ensemble of carriers, and the calculation of the quantum-mechanical scattering rates for each carrier. Furthermore, the change in the applied electric field needs to be accurately known, which can be achieved by solving Poisson's equation (Equation A.1) in three dimensions. These requirements can be fulfilled within the framework of a carrier dynamics simulation such as described in the following and in Refs. [67; 68].

4.2.2 Carrier dynamics simulation

In order to model the ultrafast carrier dynamics leading to terahertz emission without resorting to arbitrary fitting parameters, an approach based on a three-dimensional Monte Carlo simulation [68] was adopted. This model includes the interactions between extrinsic and photogenerated carriers in the Γ , L and X-valleys, plasmon and magnetoplasmon effects, and the dielectric-air interface [68; 120]. In brief, a set of 10^6 pseudoparticles comprising extrinsic and photogenerated carriers and fixed ions are used to simulate the semiconductor. At each 5 fs step in time the model numerically

solves Poisson's equation to obtain the three-dimensional potential, subject to the appropriate boundary conditions for the surface. The semiconductor is assumed to have a parabolic band structure, and Γ , L and X valleys and heavy holes are included with the parameters listed in Table 4.1. Carrier-carrier, carrier-phonon, carrier-charged impurity and carrier-vacancy scattering mechanisms are included [68; 121]. The simulated particles are within a box of size $x \times y \times z = 6 \times 6 \times 4 \mu\text{m}^3$, which is subdivided into a grid of $64 \times 64 \times 32$. The simulation starts at a time $t = -0.7 \text{ ps}$, to allow the extrinsic carriers to equilibrate before the arrival of the incident optical pulse, which has peak intensity at time $t = 0.0 \text{ ps}$, and is centred at $x, y = 0$.

The simulation uses incident pulse parameters characteristic of state-of-the-art pulsed lasers. It is assumed that the pump pulse has a Gaussian spatial and temporal shape, and a transform-limited Gaussian energy distribution. For the case of a 10 fs Ti:Sapphire laser (with central wavelength $\lambda = 800 \text{ nm}$, $\Delta\lambda = 80 \text{ nm}$, typical beam power $P_{\text{exp}} = 400 \text{ mW}$ and a repetition rate $R = 75 \text{ MHz}$) a simulation power of $10 \mu\text{W}$ and a Gaussian spot of standard deviation $\sigma_{x,y} = 0.5 \mu\text{m}$ was used, in order to obtain the same photon flux as is achievable in experiment.

Originally, this carrier dynamics simulation was applied to surface THz emitters: it distinguished between the diffusion (photo-Dember) and surface field mechanisms of charge separation in InAs and GaAs [68; 122], and provided a quantitative explanation of the enhancement of power under a magnetic field [68]. Subsequently, it was extended by Castro-Camus *et al.* [67] to model photoconductive switch emitters. This was achieved by setting the potential ϕ at the surface accordingly: the contacts of the photoconductive switch are defined by $\phi = 0 \text{ V}$ for $-3 \mu\text{m} \leq x \leq -1 \mu\text{m}$, and $\phi = 5 \text{ V}$ for $1 \mu\text{m} \leq x \leq 3 \mu\text{m}$, corresponding to typical experimental field strengths for

large area emitters. The enhancement in emission power close to the anode of a photoconductive switch (seen experimentally) was explained as a consequence of an enhanced electric field, and the difference in electron and hole mobilities [67]. A further advantage of modelling terahertz emission is that the effect of altering one parameter (or more) of the semiconductor material or laser can be investigated rapidly, and an optimum combination sought. This was done for $\text{In}_{1-x}\text{Ga}_x\text{As}$ terahertz emitters excited by pulses from Er:fibre lasers, where potential improvements in the emission power were identified by choosing an alloy fraction closer to InAs [120]. Additionally, an experimentally observed increase in emitted THz power and bandwidth from LT-GaAs photoconductive switches with increasing pump fluence was accurately modelled with the simulation, and attributed to a reduced screening time of the applied electric field [123].

This carrier dynamics simulation is utilised throughout the remainder of this Chapter. In Section 4.4 it is extended to model THz emission from heavily damaged semiconductors, such as low-temperature-grown and ion-implanted semiconductors. Subsequently, in Section 4.6.1 it is used to investigate how the pinning of the Fermi-level, created by surface defects, influences THz emission.

4.3 THz radiation from semiconductor surfaces

Terahertz emission from semiconductor surfaces can be used to investigate the carrier dynamics in ion-damaged semiconductors (Section 4.4), or to probe the surface charge distribution (Section 4.6.1). In this section, typical surface emission measurements from the III-V semiconductors are introduced experimentally, providing insights into

Table 4.1: Parameters used in the simulation (at room temperature and pressure), from Vurgaftman *et al.*[124] and the NSM archive[118]. For InGaAs, values of the bowing parameter B for each property are in brackets, taken from Vurgaftman *et al.*[124]. When no bowing parameter was found in the literature, linear interpolation between InAs and GaAs was used and the value is given in *italic*. The two-mode TO-phonon energies for InGaAs were taken from Groenen *et al.* [125]. For consistency the intervalley deformation potential D_{ij} was taken from Zollner *et al.*[126], the only reference found with values for GaAs, InAs and InP.

Parameter	GaAs	In _{0.53} Ga _{0.47} As	InAs	InP
Γ valley band-gap E_Γ (eV)	1.42	0.73 (0.477)	0.354	1.34
L valley offset $E_{L-\Gamma}$ (eV)	0.29	0.58 (0.33)	0.73	0.59
X valley offset $E_{X-\Gamma}$ (eV)	0.48	0.56 (1.4)	1.02	0.85
Γ valley effective mass (m_Γ^*)	0.067	0.039 (0.0091)	0.022	0.08
L valley effective mass (m_L^*)	0.56	<i>0.41</i>	0.29	0.63
X valley effective mass (m_X^*)	0.85	<i>0.73</i>	0.64	0.66
Heavy hole effective mass (m_{hh}^*)	0.5	0.45 (-0.145)	0.40	0.60
Number of Γ -, L- and X-valleys	1, 4, 3	1, 4, 3	1, 4, 3	1, 4, 3
LO phonon energy (meV)	36.0	<i>33.0</i>	30.0	43.0
TO-phonon energy (meV)	33.5	<i>31.6, 28.3</i>	26.7	38.1
$D_{\Gamma L}$ (eV/m)	0.4×10^{10}	<i>0.7×10^{10}</i>	1.0×10^{10}	1.8×10^{10}
$D_{\Gamma X}$ (eV/m)	2.9×10^{10}	<i>2.5×10^{10}</i>	2.2×10^{10}	2.6×10^{10}
Acoustic phonon deformation potential (eV)	7.0	<i>5.9</i>	5.0	6.0
Speed of sound (ms ⁻¹)	5240	<i>4693</i>	4280	5080
Mass density (kg m ⁻³)	5360	<i>5506</i>	5667	4810
Static/high frequency dielectric constant $\epsilon_s, \epsilon_\infty$	12.95, 10.89	13.9 (0.67), <i>11.6</i>	15.15, 12.25	12.5, 9.61
Absorption coefficient α (μm^{-1}) [$\lambda = 800\text{nm}$]	1.2	0.8 [$\lambda = 1.55\mu\text{m}$]	6.5	2.5

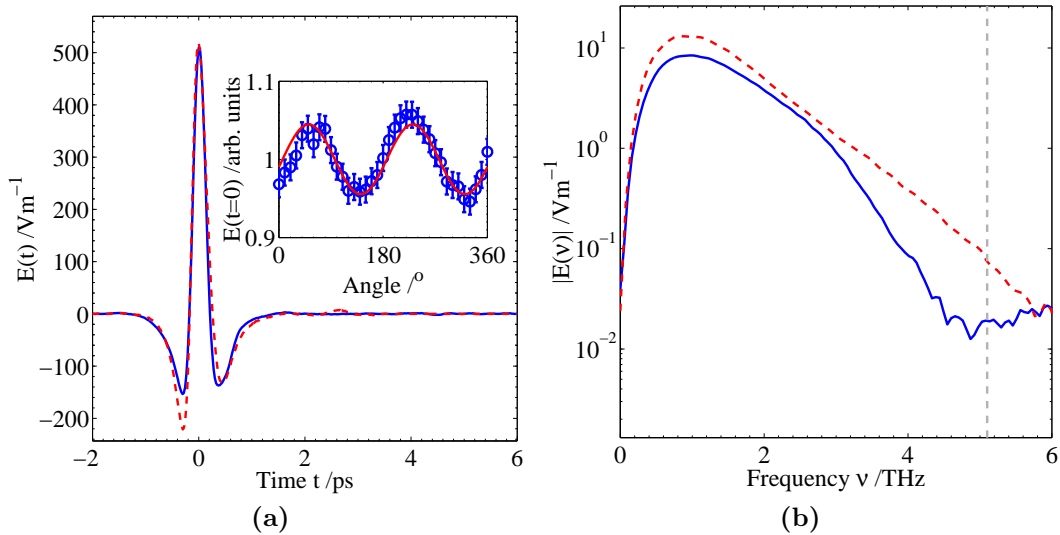


Figure 4.2: (a) Emitted THz electric field from surface of InAs, as detected by electro-optic sampling using a 0.2 mm-thick (110) ZnTe (solid line) or with a 0.2 mm (110) GaP (dotted line) crystal. (**Inset**) Peak of emitted electric field as sample is rotated about its surface normal, indicating that optical rectification contributes less than 8 % of the emitted field at these pump fluences. (b) Fourier transform of data in (a). The amplitude as detected by the ZnTe crystal (solid line) and GaP (dotted line, TO-phonon at 11 THz).

the dynamics of photoexcited carriers in these materials.

At the typical pump fluences available with unamplified Ti:sapphire lasers, the dominant THz radiation mechanism from (100) GaAs surfaces is charge separation under the surface field, while for higher mobility semiconductors such as (100) InAs the photo-Dember effect prevails [68] (Figure 2.3). At higher fluences, and for (110) and (111) crystal cuts, THz emission from optical rectification (the non-linear mixing of two optical frequency photons, producing a THz frequency photon) becomes more significant [127].

The THz emission from InAs, GaAs, InSb and GaSb were measured as follows: 90% of the output of a Ti:Sapphire oscillator laser (10 fs pulse duration, 75 MHz repetition

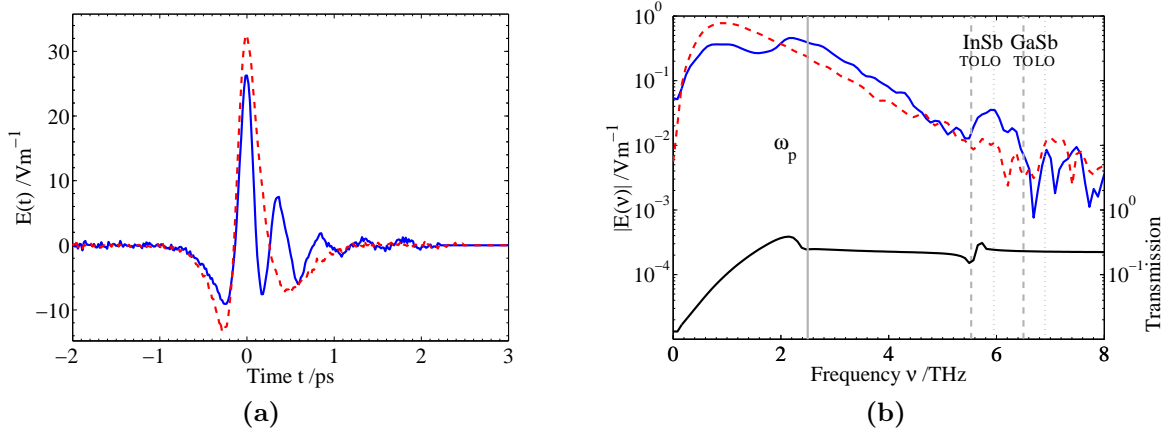


Figure 4.3: (a) Time-domain THz electric field recorded from InSb (solid line) and GaSb (dotted line) surfaces. (b) Frequency-domain THz electric field for InSb (solid blue line) and GaSb (dotted line). Vertical lines indicate the plasma frequency of InSb, and the TO- and LO-phonon frequencies of InSb and GaSb. The modelled transmission from InSb into vacuum is also shown (black line).

rate, 450 mW beam power, 790 nm wavelength) was incident on the semiconductor's surface at 45°; the remainder was used to detect the emitted THz transient using electro-optic sampling using 0.2 mm-thick (110) detection crystals of either ZnTe or GaP. The measured THz time-domain electric field from InAs is plotted in Figure 4.2a – the peak of E_{THz} as the sample is rotated about its surface normal is shown as an inset. Optical rectification can be seen to contribute less than 8% to E_{THz} . Turning now to Figure 4.2b, the amplitude spectrum measured using ZnTe was reduced significantly close to its TO-phonon mode (5.1 THz), owing to absorption and dispersion in the crystal. In comparison, GaP has its TO-phonon mode at 11 THz, which therefore produces no spectral features in the frequency range at which InAs emits ($0 \leftrightarrow 6$ THz).

The larger magnitude of photo-Dember emission from InAs in comparison to GaAs can be ascribed to the greater difference in electron and hole mobilities [68]. By this reasoning, the antimonides InSb and GaSb ought to act as excellent emitters of THz

radiation. However, the emitted THz radiation from InSb and GaSb is anomalously low, as Figure 4.3a indicates. This discrepancy may be due to the excitation energy being significantly above bandgap, resulting in extremely long carrier lifetimes that exceed the repetition period of the laser oscillator. This reduces the power from photo-Dember emitters, as discussed in Section 4.5.

An additional feature of THz emission from InSb is the observation of pronounced oscillations in the time-domain, which produce an enhancement in the emission of THz radiation around 2 THz, as exhibited in Figure 4.3b. This is a consequence of the free-electron plasma response: with a carrier density of $N = 1.7 \times 10^{16} \text{ cm}^{-3}$ the electronic plasma frequency in InSb is $\omega_p/2\pi = 2.5 \text{ THz}$. The transmission from InSb to vacuum was modelled using the Fresnel transmission coefficients (shown as the black line in Figure 4.3b), and indicates that the coupling from the semiconductor into free space increases just below ω_p . This spectral feature was not observed to alter significantly when the pump power (and therefore the photoexcited carrier density) was halved, suggesting that extrinsic doping carriers are mainly responsible for the plasma response.¹ The change in density across the photo-excited carrier distribution might account for the deviation between this simple model and the measured spectral shape. Also visible in Figure 4.3b are the TO-phonon modes of InSb and GaSb, at 5.5 THz and 6.5 THz respectively. Polar semiconductors absorb electromagnetic radiation strongly at their TO-phonon frequencies (Section 2.4.1). The transmission function from a semiconductor into free space exhibits a maximum close to the LO-phonon frequency, producing an enhancement in THz emission above the TO-phonon frequency (shown for InSb in Figure 4.3b). This spectral enhancement has been observed in THz emission

¹The concentration of intrinsic carriers is expected to be $5 \times 10^{15} \text{ cm}^{-3}$ at room temperature for InSb [29].

from GaAs photoconductive switches [128], where it was assigned to the coherent emission of LO-phonons.

4.4 Emission from ion-implanted semiconductors

In the effort to improve THz emitters, one method to achieve a greater bandwidth is to shorten the rise time of E_{THz} , normally limited by the duration of the exciting infrared laser pulse. Another approach is to reduce the duration of E_{THz} after excitation, by choosing a semiconductor with a short carrier lifetime and/or a high momentum scattering rate. In this section the second approach is investigated, by examining the THz emission from the surfaces of GaAs implanted with As⁺ ions (Section 3.1.3) at different doses. Subsequently, the carrier dynamics in ion-implanted GaAs is simulated, via the inclusion of carrier-vacancy momentum scattering (Section 4.4.2) and an ultra-short carrier lifetime (Section 4.4.3).

Both surface field [129] and photoconductive antenna [130] ion-implanted THz emitters have been previously studied, and were found to produce THz radiation at slightly higher frequencies than semi-insulating GaAs [130]. Additionally, ion-implanted photoconductive antennae have been used as detectors of THz radiation, [71; 131] where the carrier lifetime plays a critical role in determining the THz electric field from the measured current [132]. Some previous studies utilised low energy ions, typically 200 keV, resulting in implantation depths of only $\sim 0.1 \mu\text{m}$. However, as the infrared absorption depth is $\sim 0.8 \mu\text{m}$ in GaAs only $\sim 10\%$ of photocarriers are generated within $0.1 \mu\text{m}$, and the non-implanted layer dominates THz emission. In this work a uniform density of vacancies was formed over the infrared absorption depth

(Figure 3.2) by performing multi-energy implantations of arsenic ions (at 1 MeV and 2.4 MeV), and subsequently annealing the sample.

4.4.1 Measured surface field terahertz emission

The THz electric fields emitted from seven GaAs:As⁺ samples were measured (using a 0.2 mm (110) ZnTe crystal) with a signal-to-noise ratio of above 150:1. The maximum THz electric field strength was of the order of 3 Vm^{-1} , less than observed for the unimplanted GaAs reference sample (4 Vm^{-1}), and an InAs sample (216 Vm^{-1}) with the same experimental setup.² The emitted power was not found to vary systematically with ion dose, perhaps because of variations in the surface potential of the samples, which can greatly alter the surface field strength.

Typical measured THz electric fields are shown in Figure 4.4 for low ($2.5 \times 10^{12} \text{ cm}^{-2}$ at 1 MeV, $1 \times 10^{13} \text{ cm}^{-2}$ at 2.4 MeV) and high ($1.25 \times 10^{15} \text{ cm}^{-2}$ at 1 MeV, $5 \times 10^{15} \text{ cm}^{-2}$ at 2.4 MeV) implant doses, annealed for 30 minutes at 500 °C. At higher implant doses the THz pulse duration is shorter, and the negative peak after the principal peak has both larger magnitude and smaller period (Figure 4.4a). In Figure 4.4b the Fourier transform of the time-domain electric field reveals that at greater ion doses THz emission shifts to higher frequencies.

The post-implant thermal annealing step (500 °C, 30 min.) was observed to result in larger peak THz fields, and greater power at low frequencies, as shown in Figure 4.5 for the lowest dose sample ($2.5 \times 10^{12} \text{ cm}^{-2}$ at 1 MeV, $2.5 \times 10^{12} \text{ cm}^{-2}$ at 2.4 MeV). Annealing removes defects, at least partly repairing the damaged crystal structure.

²The reduced THz emission amplitudes in comparison with those in the rest of this chapter are a consequence of an older spectrometer design being used to collect the data in this section, with a lower collection efficiency.

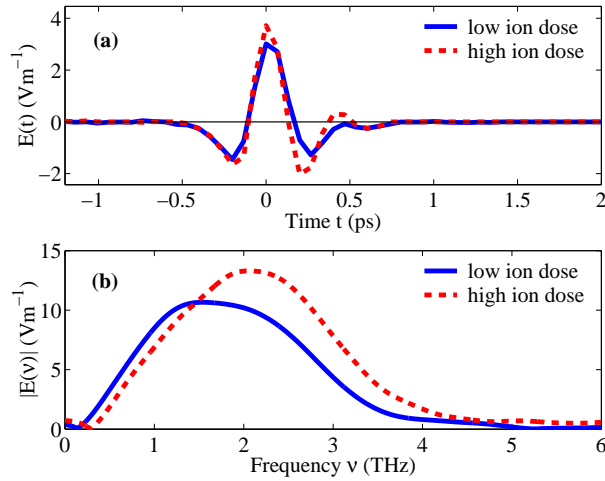


Figure 4.4: (a) Measured THz electric field E_{THz} emitted via the surface field mechanism from GaAs:As⁺ samples implanted with a low (solid line) and high dose (dotted line), and subsequently annealed, as described in the text. (b) Fourier transform of data in (a) illustrates a shift in emission to higher frequencies when implanting at higher doses.

Because defects scatter carriers, and can also trap conduction band electrons, one can qualitatively predict that annealing will increase the pulse width, decreasing the relative THz emission at high frequencies. In order to be more quantitative, a simulation approach based on the model described in Section 4.2.2 is now adopted.

4.4.2 Scattering from neutral impurities

When As⁺ ions collide with atoms in GaAs both the incident ion and the recoiling target atoms introduce vacancies, which act as carrier scattering centres. Calculations using SRIM [99] suggest that approximately 10,000 vacancies are produced per incident ion, with the damage profile of Figure 3.2. For the unannealed samples this corresponds to vacancy concentrations ranging from $N_{\text{vac}} \sim 10^{19} \text{ cm}^{-3}$ to $\sim 10^{22} \text{ cm}^{-3}$. Electron paramagnetic resonance experiments have shown [133] that the concentration of arsenic antisite defects is about 10^{18} cm^{-3} after a 500°C, 30 min. anneal, for ion doses of

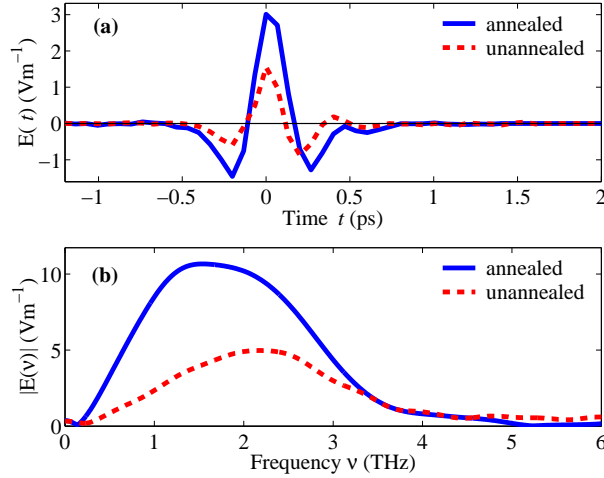


Figure 4.5: THz emission from unannealed (dotted lines) and annealed GaAs:As⁺ (solid lines) for the lowest implant dose ($1 \times 10^{13} \text{ cm}^{-2}$ at 2.4 MeV and $2.5 \times 10^{12} \text{ cm}^{-2}$ at 1 MeV). Annealing causes an increase in maximum THz field from 1.6 Vm^{-1} (unannealed) to 3.0 Vm^{-1} (annealed), but a decrease in the frequency of peak power from 2.1 THz (unannealed) to 1.6 THz (annealed).

10^{16} cm^{-2} . Since N_{vac} for the annealed samples therefore varies from 10^{15} cm^{-3} to 10^{18} cm^{-3} , carrier-vacancy scattering cannot be disregarded as it normally is at lower defect concentrations.

Vacancies are included in the simulation by assuming that carriers scatter elastically from an electrically neutral spherical square well of width R , as defined by the potential $V = -V_0$ for carrier-vacancy distances $r \leq R$ and $V = 0$ for $r > R$. Following the partial-wave approach taken in Ref. [134], the momentum scattering rate W_{vac} can be calculated from the cross-section σ using $W_{\text{vac}} = \sigma N_{\text{vac}} v$, where v is the electron velocity before (and after) scattering. The resulting expression is

$$W_{\text{vac}} = \frac{4\pi\hbar N_{\text{vac}}}{m^*k} \frac{(k \cot kR - \beta \cot \beta R)^2}{(k^2 + \beta^2 \cot^2 \beta R)(1 + \cot^2 kR)}, \quad (4.3)$$

where β is given by

$$\beta = \sqrt{\frac{2m^*(E + V_0)}{\hbar^2}}. \quad (4.4)$$

The final state carrier is scattered uniformly into 4π steradians, because of the

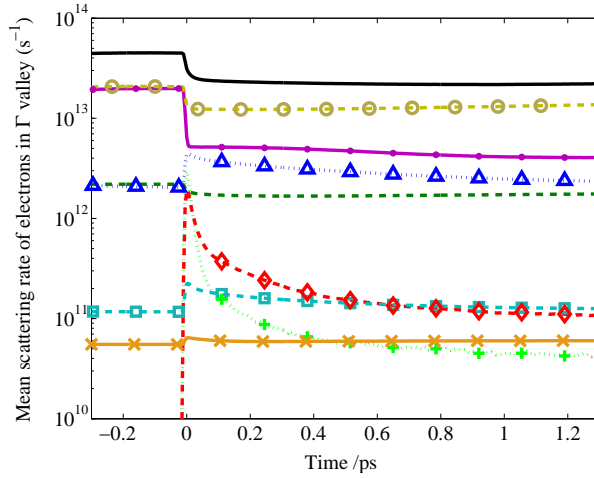


Figure 4.6: Momentum scattering rates for electrons in the Γ -valley, with donor and vacancy concentrations of $1 \times 10^{15} \text{ cm}^{-3}$ each. The rate for each scattering mechanism is averaged over all particles in the simulation, and is plotted as a function of time after laser excitation. The largest contributions to the total rate (solid line) come from electron-hole scattering (\circ) and charged impurity scattering (dots). LO-phonon emission (\triangle) and absorption (dashed line) are also significant. Acoustic phonon scattering (\square) and vacancy scattering (\times) produce lower rates, as do TO-phonon absorption (\diamond) and emission (\oplus) with the electronic final state in the L-valley. The infrared pulse arrives at $t = 0$ ps, and produces a step in most scattering rates.

spherical symmetry of the well. Taking typical literature values of $R = 3 \text{ nm}$ and $V_0 = 300 \text{ meV}$ [92] produces a scattering rate ranging from $\sim 10^{11} \text{ s}^{-1}$ at $N_{\text{vac}} = 1 \times 10^{15} \text{ cm}^{-3}$ to $\sim 10^{14} \text{ s}^{-1}$ at $N_{\text{vac}} = 1 \times 10^{18} \text{ cm}^{-3}$.

To enable a comparison between these carrier-vacancy momentum scattering rates and those of the other scattering mechanisms, Figure 4.6 shows the average momentum scattering rates of electrons in the Γ -valley as a function of time t after the infrared pulse for $N_d, N_{\text{vac}} = 1 \times 10^{15} \text{ cm}^{-3}$. The scattering rates vary as a function of time due to changing carrier concentration and energy distributions. The greatest contributions to the total rate result from electron-hole scattering and charged impurities, which both decrease at $t = 0$ since they are inversely proportional to the local carrier density [68]. LO-phonon emission and absorption contribute $\sim 10\%$ to the total rate. Acoustic

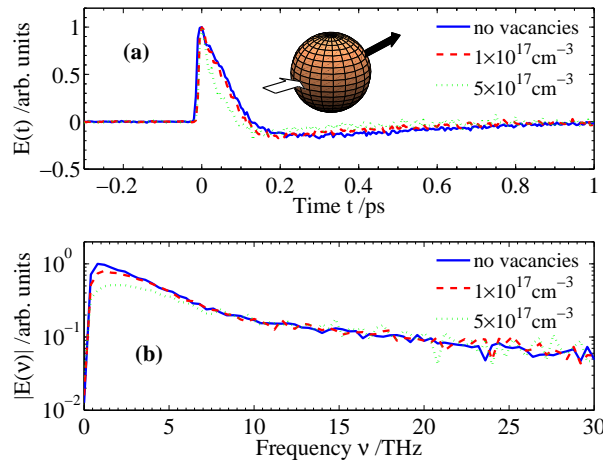


Figure 4.7: Simulated THz emission from GaAs:As⁺, in (a) the time domain and (b) the frequency domain, with no vacancies, and for vacancy concentrations of $1 \times 10^{17} \text{ cm}^{-3}$, $5 \times 10^{17} \text{ cm}^{-3}$. The FWHM of the spectra increase slightly with vacancy concentration. (Inset) In (a) the spherical potential well, and scattering geometry, is shown schematically.

phonon and neutral vacancy scattering provide only $\sim 1\%$ of the total rate. At $t = 0$ the rates from TO-phonon emission or absorption followed by a jump into the L-valley are $\sim 1\%$, but decrease to $\sim 0.1\%$ at later times due to the average carrier energy decreasing.

The simulated THz emission from GaAs surfaces is plotted in Figure 4.7a: the pulse duration decreases at increasing vacancy concentration. An increase in N_{vac} produces a larger W_{vac} , and a shorter THz pulse. While Figure 4.6 provides some insight into the significance of the various momentum scattering mechanisms, the angular distribution of each mechanism must also be considered. At $N_{\text{vac}} = 1 \times 10^{17} \text{ cm}^{-3}$ the vacancy scattering rate is $\sim 6 \times 10^{13} \text{ s}^{-1}$, i.e. only 10% of the total rate, yet as can be seen in Figure 4.7a the THz pulse duration is reduced. This is a consequence of the uniform angular distribution for vacancy scattering: the carrier direction is altered more significantly than in the other mechanisms.

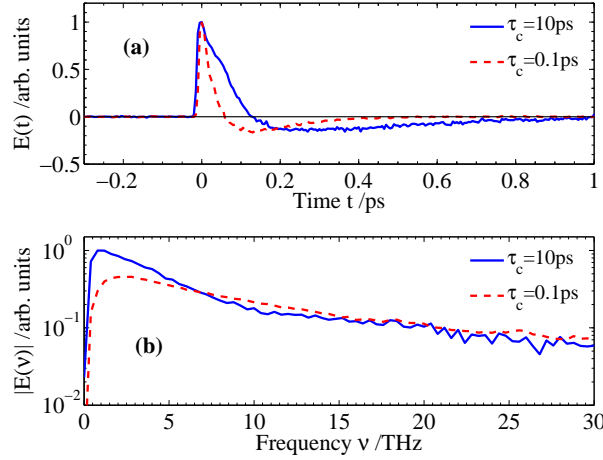


Figure 4.8: Simulated THz electric field from bulk GaAs at carrier trapping times of $\tau_c = 10\text{ ps}$ and $\tau_c = 0.1\text{ ps}$. In (a) the unfiltered simulated $\tau_c = 0.1\text{ ps}$ pulse (dashed line) has shorter duration than the 10 ps (solid line). Their Fourier transforms are shown in (b) .

4.4.3 Carrier trapping at defects

The effect of trapping defects on THz emission was included in the simulation by introducing an exponential decay of the number of photoexcited carriers n as a function of time t after the infrared pulse according to the equation

$$n(t) = n(0)e^{-t/\tau_c}, \quad (4.5)$$

where τ_c is the carrier trapping time. Time-resolved photoluminescence experiments of GaAs:As⁺ implanted with a single 10^{16} cm^{-2} dose of 2 MeV ions have measured the carrier trapping time to be as short as $\tau_c = 0.1\text{ ps}$ [95; 100]. It is important to distinguish τ_c from the carrier recombination time, which is $\sim 4\text{ ps}$ [135]. It is assumed that once trapped carriers cannot escape the defect via thermal excitation, and that trapped carriers do not alter free carrier states. When the number of carriers n is reduced on time scales of $< 1\text{ ps}$ the electric field decay time after the pulse can be shortened, as shown in Figure 4.8, resulting in a greater bandwidth. At $\tau_c = 0.1\text{ ps}$ the

FWHM from the simulation is 7.8 THz, nearly 80% larger than at a carrier trapping time of > 10 ps (FWHM = 4.4 THz).

4.4.4 Comparison of experiment and simulation

The spectrum of the simulated THz emission has a larger magnitude at both low and high frequencies than the experimental data (Figure 4.9b). This can be accounted for by the combined effect of the electro-optic sampling system and the parabolic mirrors used to collect the THz radiation. A frequency-domain picture of EOS with ZnTe has been presented by Gallot *et al.* [136; 137] that models the effect of the detection apparatus using three complex filters, namely: the spectrum of the autocorrelation of infrared pulse (which has negligible effect), the frequency-dependent electro-optic susceptibility $\chi^{(2)}$ of ZnTe, and the mismatch between the infrared group velocity and THz phase velocity in ZnTe. The resulting low-pass filter causes the simulation's high frequency components to reduce in magnitude, as shown in Figure 4.9b. While the slow drop-off in simulated electric field at increasing frequencies suggests that large bandwidths are possible from surface field THz emitters, experimentally a thin ($\sim 10 \mu\text{m}$) ZnTe crystal is necessary to observe such frequency components, rather than the $200 \mu\text{m}$ thick one used here.³

While the experiment was designed to collect THz radiation with high efficiency, low frequency THz radiation emitted from the sample surface will be diffracted beyond the collection capability of the parabolic mirrors. By treating the two parabolic mirrors as a single thin lens, Côté *et al.* have calculated the high-pass filter cor-

³Or alternatively a GaP crystal, with its higher TO-phonon frequency, can be used to measure at higher frequencies, as in Section 4.3.

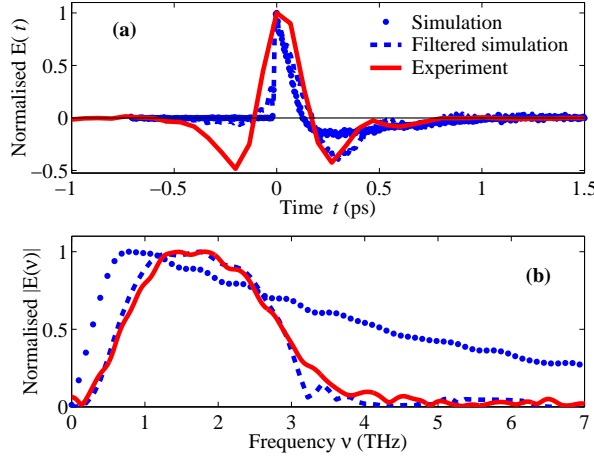


Figure 4.9: Comparison of simulated THz emission from GaAs with n-type doping $N_d = 1 \times 10^{15} \text{ cm}^{-3}$ using the low-dose sample data from Fig. 4.4. In (a) the simulated electric field (dots) is seen to have a sharp rise $\sim 10 \text{ fs}$ in duration, and to drop sharply after $\sim 0.1 \text{ ps}$, producing the broad spectrum in (b). When low-pass and high-pass filters are applied (taking account of the dispersion in ZnTe, and diffraction-limited collection respectively, as described in the text), the filtered spectrum (dashed line) can be seen to match the experimental spectrum (solid) extremely well. When transformed back into the time-domain, the filtered simulated electric field (the dashed line of (a)) matches for times $\geq 0.2 \text{ ps}$.

responding to this effect [138]. They found that the approximate filter function $F_{\text{high}}(\omega) = \text{erf}^2(2\omega R\sigma/cf)$, where the THz radiation has a Gaussian beam-waist σ , and is collected by two parabolic mirrors each of focal length f and radius R . For this experimental geometry ($f = 15 \text{ cm}$, $R = 2.5 \text{ cm}$, $\sigma = 0.16 \text{ mm}$) this filter has a steep rise from 0 to 1 between 0 and $\sim 1.5 \text{ THz}$, which when applied to the simulated data causes a reduction in low frequency components of the electric field.

Multiplying the simulated spectrum by these filters in the frequency domain produces an accurate match to the experimental spectra, as Figure 4.9b indicates. Taking the inverse Fourier transform of the filtered simulated spectrum results in a time-domain trace that compares adequately with the experimental time-domain data (Figure 4.9a). The low-pass (ZnTe) filter causes an increase in both the oscillation period

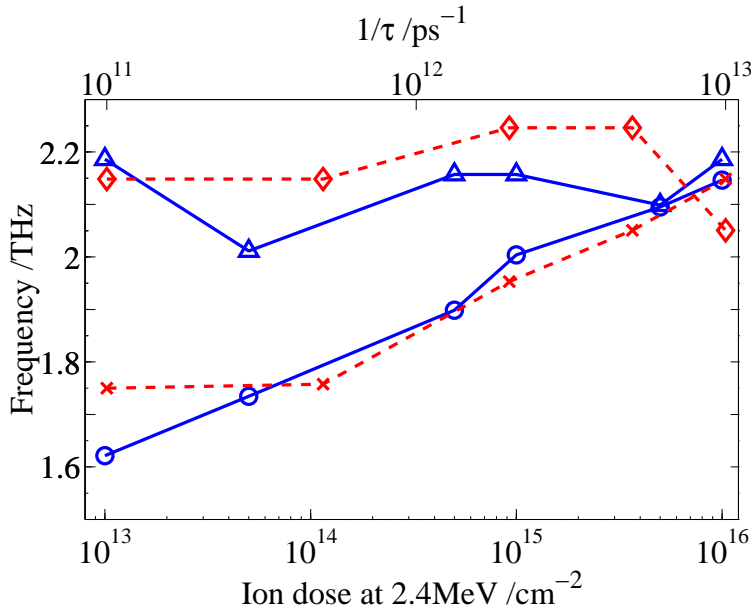


Figure 4.10: Frequency of peak emitted THz power f_{peak} (circles, solid line) and FWHM of spectra (triangles, solid line) as a function of ion dose at 2.4 MeV (the 1 MeV ion dose was a quarter of the 2.4 MeV dose). f_{peak} is defined as the midpoint of the two frequencies at which the amplitude of the Fourier transform of the electric field is 95% of its maximum. The experimental data can be compared with values extracted from spectra produced by the carrier dynamics simulation (dashed lines), plotted as a function of inverse carrier trapping time $1/\tau_c$. The trend in f_{peak} (crosses) from the simulation reproduces the experiment. The FWHM from the simulation after filtering (diamonds) do not vary with $1/\tau_c$, and are consistent with those measured.

and the negative peak amplitude after the pulse. The dip in experimental electric field before the pulse is not reproduced by the application of the filters to the simulated data, and may be an artefact of the alignment.

The filters were applied to simulated spectra at carrier trapping times varying from $\tau_c = 0.1 \text{ ps}$ to $\tau_c = 100 \text{ ps}$. As shown in Figure 4.10, this enables a direct comparison between the experimental f_{peak} as a function of ion dose, and f_{peak} extracted from the model as a function of $1/\tau_c$.⁴ When $\tau_c = 0.1 \text{ ps}$ the filtered spectral peak is at

⁴Since the publication of these results in Figure 8 of Ref. [121], the simulation was extended with a more realistic (Gaussian) pump pulse energy distribution, with the consequence of a better match to the data, as shown here. Additionally, the data point at $1 \times 10^{14} \text{ cm}^{-2}$, present in the experimental data of Ref. [121], has been removed owing to an anomalously large lifetime (as measured by optical-

2.15 THz, in excellent agreement with the value (also 2.15 THz) of the highest dose sample ($2.5 \times 10^{15} \text{ cm}^{-2}$ at 1 MeV, $1 \times 10^{16} \text{ cm}^{-2}$ at 2.4 MeV). As the carrier trapping time is increased ($1/\tau_c$ decreased) the simulation tends to $f_{\text{peak}} = 1.75 \text{ THz}$, a close match to the experimental value (1.62 THz). Values of the FWHM of filtered simulated spectra are approximately independent of τ_c , owing to the bandwidth limitations imposed by the 0.2 mm-thick ZnTe crystal.

A smaller increase in f_{peak} was observed over the experimental range of vacancy concentrations: at 10^{15} cm^{-3} $f_{\text{peak}} = 1.6 \text{ THz}$, and at 10^{18} cm^{-3} $f_{\text{peak}} = 1.9 \text{ THz}$. This suggests that carrier trapping may be more significant than carrier-vacancy momentum scattering in determining THz pulse duration.

The experimental reduction in the spectral peak of THz emission after annealing (Fig. 4.5) may be attributed to a combination of a reduction in carrier-vacancy scattering and an increase in carrier trapping time from $\tau_c \sim 0.1 \text{ ps}$ to $\tau_c \sim 1 \text{ ps}$.

4.5 Long-lived carriers limit THz emission

In Section 3.3.2 time-resolved conductivity measurements of high-purity GaAs were reported, and it was demonstrated that photoexcited electrons can have lifetimes τ exceeding the pulse period (typically $> 10 \text{ ns}$) of mode-locked lasers with a high repetition rate. This finding is of great significance to the design and performance of photoconductive THz emitters and detectors, and has been largely overlooked in the past. The residual carriers created by the preceding laser pulse will reduce the change in conductivity, and therefore also the emitted field strength. In addition, the low-pump THz-probe spectroscopy).

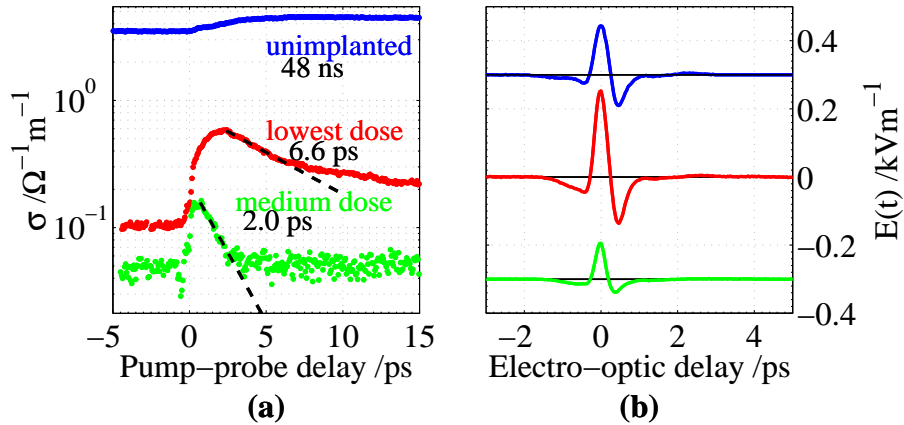


Figure 4.11: (a) Time-resolved conductivity of Fe^+ -implanted $\text{In}_{0.53}\text{Ga}_{0.47}\text{As}$ measured using optical-pump, THz probe setup based on a Ti:Sapphire laser oscillator with a high (75 MHz) repetition rate. Data are shown for unimplanted InGaAs (blue), a low dose implant (red, $1 \times 10^{13} \text{ cm}^{-2}$ at 1.8 MeV and $2.8 \times 10^{12} \text{ cm}^{-2}$ at 0.7 MeV) and a higher dose (green, $5 \times 10^{14} \text{ cm}^{-2}$ at 1.8 MeV and $1.4 \times 10^{14} \text{ cm}^{-2}$ at 0.7 MeV). (b) Surface THz emission from InGaAs samples.

ering of the dark resistivity increases the noise background and heats the emitter, which can require cooling (to avoid device damage) when operated at high voltages [75]. Similarly, the noise in photoconductive detectors of THz radiation is increased by long-lived electrons in devices fabricated on SI-GaAs, or in low-temperature grown or ion-damaged layers (thinner than the absorption depth) on semi-insulating substrates (as in the LT-GaAs samples investigated in Section 3.4). In Ref. [139], Hussain *et al.* demonstrate that a 100 nm-thick AlAs layer between a thin ($1 \mu\text{m}$) GaAs: As^+ layer and a SI-GaAs substrate significantly improves the performance of the material as a photoconductive detector. The AlAs acts as a barrier to electrons, preventing carriers from the semi-insulating substrate from entering the contacts of the detector. In another study, Bromage *et al.* report the use of long-lived carriers in semi-insulating GaAs as an attenuator, in an alternative THz measurement technique based on dithered photoconductive detection [140].

Long-lived carriers have a marked influence on the photoconductive generation of THz radiation in both surface and photoconductive switch emitters, as is now demonstrated. The time-resolved conductivity and surface emission from samples of iron-ion implanted $\text{In}_{0.53}\text{Ga}_{0.47}\text{As}$ [96] were measured, following the procedures outlined above and in Section 3.2.1. As indicated in Figure 4.11a, electrons in unimplanted InGaAs have an extremely long lifetime (48 ns) exceeding the repetition period of the laser (13.3 ns). Consequently, the conductivity before the arrival of the pump pulse (at zero delay time) is almost as high as that afterwards. After iron-ion implantation, the electron lifetime is reduced significantly to 6.6 ps at a low incident ion dose, and 2.0 ps at a higher dose.

The surface emission from these semiconductors is shown in Figure 4.11b: the amplitude of the electric field nearly doubles from the unimplanted to the lowest dose sample, before decreasing for the higher dose. This change can be explained quantitatively by the following simple model. For a photo-Dember emitter such as InGaAs the current density is $\mathbf{J} \propto \mu \nabla n$ (Equation 4.2) since the surface field component σE is negligible. Furthermore, the dominant component of the gradient of the electron concentration ∇n is the z -component (i.e. the surface normal): the carrier distribution has an extent of the spot size ($\sim 50 \mu\text{m}$) in the x and y directions, but significantly less in the z direction ($1/\alpha \sim 0.3 \mu\text{m}$). Therefore, $\partial n / \partial z$ dominates THz emission, and using $n(z) = n_0 \exp(-\alpha z)$ one can write $\partial n / \partial z \propto n$. Consequently, $J \propto \mu n \propto \sigma$ for a photo-Dember emitter, meaning that the emitted THz field strength $E_{\text{THz}} \propto \partial \sigma / \partial t \sim \Delta \sigma / \Delta t$. Employing this simple relation, and inputting values of the change in conductivity before and after the arrival of the pump pulse from the time-resolved conductivity (Figure 4.11a) produces a relative emission amplitude of

1.81 and 0.61 for the lower and higher dose InGaAs:Fe⁺ samples respectively, in comparison to that from unimplanted InGaAs. These values agree well with the measured relative emission amplitudes, which are 1.75 and 0.73.

To further investigate the effect of long-lived electrons on THz emission, photoconductive switches were fabricated on SI-GaAs, LT-GaAs and GaAs:As⁺ samples, and the time-resolved conductivity of each material was measured to determine its electron lifetime and mobility. The GaAs:As⁺ (implanted at a dose of $5 \times 10^{13} \text{ cm}^{-2}$ at 2.4 MeV and $1.25 \times 10^{13} \text{ cm}^{-2}$ at 1.0 MeV) had a mobility $\mu = 978 \text{ cm}^2 \text{V}^{-1} \text{s}^{-1}$ and initial lifetime $\tau = 1.3 \text{ ps}$, while for the LT-GaAs (1 μm thick layer on SI-GaAs) $\mu = 2470 \text{ cm}^2 \text{V}^{-1} \text{s}^{-1}$ and $\tau = 50 \text{ ps}$, assuming that the mobility of SI-GaAs was $8500 \text{ cm}^2 \text{V}^{-1} \text{s}^{-1}$. The THz emission from each emitter was measured using a 200 μm thick GaP crystal, and is reported in Figure 4.12. Spectral power can be observed beyond the TO-phonon mode of GaAs at 8.1 THz. Both the THz radiation emitted in the ‘transmission’ and ‘reflection’ geometry were measured, namely that emitted parallel and anti-parallel to the direction of the emitter pump beam. The only alterations required to the spectrometer (see Figure 2.1) were the flipping of the first parabolic mirror, and the relocation of the photoconductive emitter, which was placed and aligned using an $x - y - z$ translation stage. The pump fluences were set to comparable values.

The amplitude spectra of the measured THz emission from SI-GaAs, LT-GaAs and GaAs:As⁺ samples are shown in Figure 4.12, for the reflection geometry. The peak recorded time-domain electric field of these emitters increases with the mobility extracted from the time-resolved conductivity, as the figure’s inset demonstrates. In the transmission geometry, however, the situation is more complex. While the emitted field for the GaAs:As⁺ sample is almost identical to that in the reflection geometry,

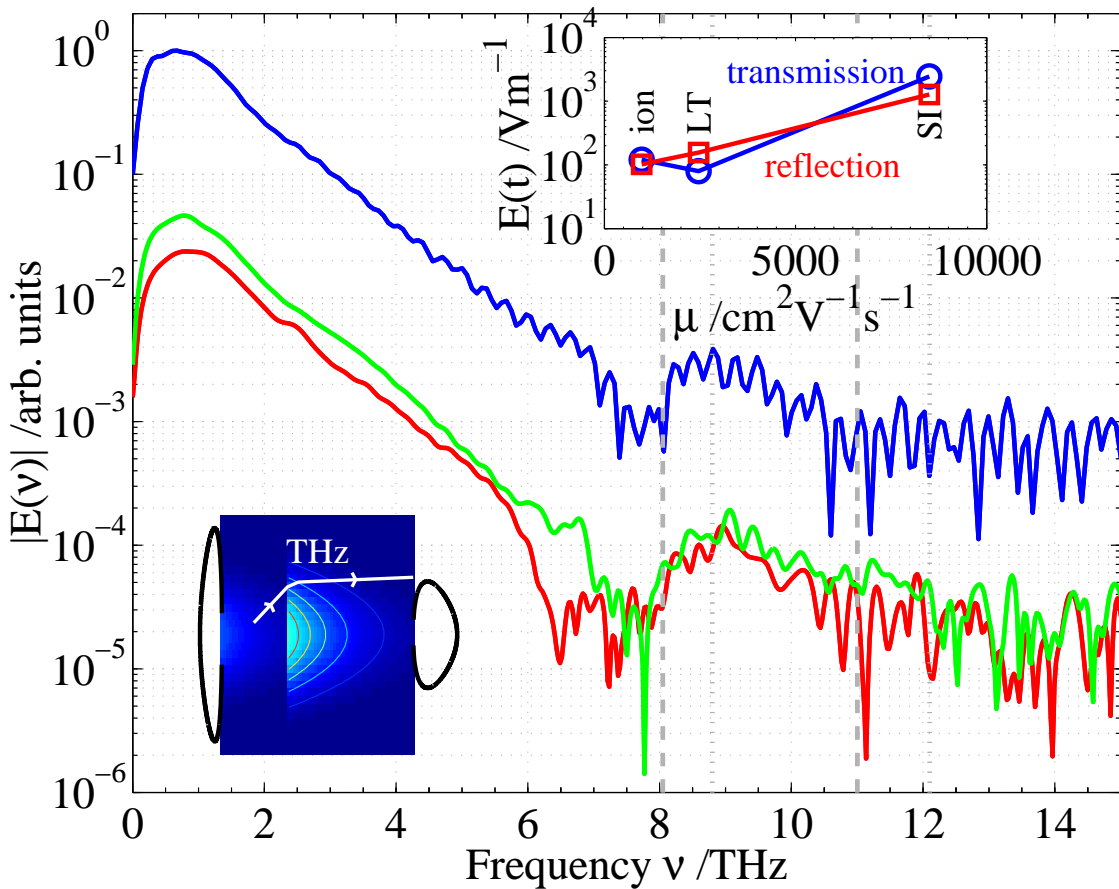


Figure 4.12: Amplitude spectra of THz emission from photoconductive switches made on SI-GaAs (blue), LT-GaAs (green) and GaAs:As⁺ (red). (**Inset, top right**) Peak of time domain electric field versus mobility extracted from time-resolved conductivity data, in the transmission (○) and reflection (□) geometry. (**Inset, bottom left**) Cartoon (not to scale) of the carrier density in LT-GaAs, as in Figure 3.9. The white lines indicate the collimation of a THz photon as it enters the optically dense semi-insulating substrate. Black lines indicate the expected shape of the radiation patterns in free space in the transmission and reflection geometry.

the amplitude for LT-GaAs in transmission is smaller than that in reflection. This is a consequence of the long-lived electron distribution in the sample's semi-insulating substrate: the THz radiation emitted from within the LT-GaAs layer is partially reflected by the charges in the substrate (Section 3.2.1). The power emitted from SI-GaAs emitters also differs between the two geometries: a greater peak field is recorded in transmission. This may be a consequence of the electron distribution acting as a lens, a situation shown schematically in the bottom-left inset to Figure 4.12. Within the Drude model of a free-electron gas (Equation 2.10), the real part of the refractive index ($\Re(n)$) is lower below the plasma frequency ω_p than above it. Consider now the propagation of an emitted THz photon (at a particular frequency in the THz range below ω_p): as it moves away from the surface it enters a region with a reduced carrier density (shown by the coloured contour lines in Figure 4.12), with a lower ω_p (Equation 2.11). The photon is refracted, owing to the increase in $\Re(n)$ as ω_p decreases – this is illustrated by the white ray in the inset to Figure 4.12. Also shown are the expected radiation patterns in the reflection and transmission directions: in the transmission direction the power is somewhat more collimated. This lensing effect should also play a role in the LT-GaAs emitter. Neither this lensing effect (which increases E_{THz}) nor long-lived electrons (which decrease E_{THz}) are significant for the GaAs:As⁺ sample, because the damaged region extends further than the absorption depth of the semiconductor (Figure 3.2).

4.6 Enhanced emission from passivated surfaces

In Section 3.3.2 the time-resolved conductivity of SI-GaAs was shown to double in magnitude after the passivation of surface defect states. Here, the influence of the passivation of the surface is investigated further by THz emission measurements and the simulation of surface emitters. Subsequently, a doubling in the power of THz emission from photoconductive switches fabricated on passivated GaAs is reported, owing to the enhanced conductivity change. A 0.2 mm (110) ZnTe on a 6 mm (100) substrate was used in the work reported in this section.

4.6.1 Surface emitters

The THz emission from the surfaces of the passivated and reference samples was measured, and is shown in Figure 4.13a. The polarity of the THz electric field from the etched GaAs sample was opposite to that of InAs, while for passivated GaAs the radiated pulses had the same polarity as InAs. The polarity change suggests that passivation suppresses the surface states that create the surface field, namely that passivated GaAs acts as a photo-Dember emitter. No significant change in the THz emission from samples of InSb was observed after applying the same passivation process, since InSb (like InAs) is primarily a photo-Dember emitter (Figure 4.13) [127].

The three-dimensional carrier dynamics simulation outlined in Section 4.2.2 was used to investigate how changes to the surface states in GaAs alter THz emission. The influence of surface defects can be described by the pinning of the electrostatic potential at the surface, where the potential relative to the bulk is V_{pin} . Figure 4.13b indicates the peak of the simulated THz electric field as V_{pin} is varied. With no Fermi

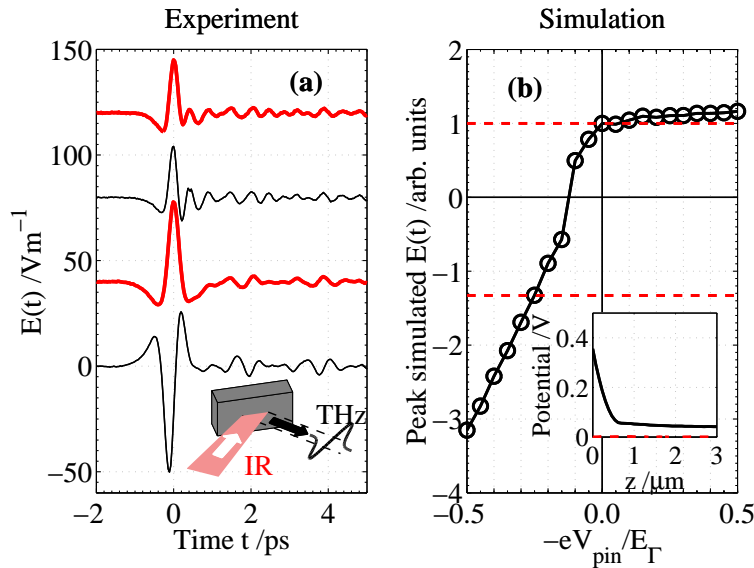


Figure 4.13: (a) From bottom to top: Emitted time-domain THz electric field from surfaces of etched GaAs, passivated GaAs, etched InSb and passivated InSb. The peak of THz pulses emitted from InAs (not shown) had a positive sign. The oscillations after the main pulse result from the THz absorption lines of atmospheric water vapour. Passivation produces no noticeable change in E_{THz} for InSb, but causes the polarity to flip and the amplitude to decrease for GaAs. (Inset) schematic of experimental geometry, showing the infra-red (IR) emitter pump beam at 45° to the emitter, and the radiated THz pulse. (b) Peak of simulated THz electric field emission from GaAs surfaces, versus surface pinning potential energy $-eV_{\text{pin}}$ relative to the bandgap energy $E_\Gamma = 1.42$ eV. Dotted horizontal lines represent the measured peak field sizes for the passivated (top) and etched reference (bottom) samples. (Inset) Simulated electrostatic potential 50 fs after the arrival of the infrared pump pulse, as a function of depth z into the semiconductor, for $V_{\text{pin}} = 0.355$ V (solid line) and $V_{\text{pin}} = 0$ V (dashed line).

level pinning ($V_{\text{pin}} = 0$) the simulated THz radiation has the same sign as InAs, and the semiconductor acts as a photo-Dember emitter – there is no surface field, as the inset to Figure 4.13b indicates. As V_{pin} becomes increasingly negative the simulated field strength changes in sign, owing to the surface field component. Therefore, assuming that the passivated GaAs sample has $V_{\text{pin}} = 0$, the pinning potential in the etched sample can be estimated from the relative emission amplitudes as $V_{\text{pin}} = -0.25E_\Gamma/e$. This is an upper estimate on the magnitude of V_{pin} , as the passivated sample may not have $V_{\text{pin}} = 0$.

4.6.2 Photoconductive switches

The THz emission from photoconductive switches fabricated on passivated and etched GaAs is reported in Figure 4.14. It can be seen that the peak THz electric field strength from the passivated sample is larger than that of the etched reference, with a near doubling of the emitted power (Figure 4.14b). This increase can be attributed to the larger change in conductivity σ of the passivated sample (Figure 3.7), since the emitted THz electric field is $E_{\text{THz}} \propto \partial J / \partial t = \partial(\sigma E) / \partial t$ (Section 4.2.1). Obtaining a greater power from photoconductive THz emitters is beneficial for spectroscopy. Surface passivation could be used in addition to other schemes that increase the power of THz sources (such as placing a hemispherical silicon lens to collimate the emitted radiation, or using an anti-reflection coating to enhance coupling from the emitter into free space), and has the benefit of introducing no dispersive media into the THz path.

4.7 Summary

The measured and simulated emission of THz radiation from a variety of semiconductor surfaces and photoconductive switches was used in this chapter to discuss aspects of ultra-fast carrier dynamics, including the trapping of electrons in ion-implanted materials with picosecond lifetimes. Improvements in the power of THz emission were observed after passivation of the surface of GaAs, and in the power emitted at high frequencies after ion-implantation. The influence of electrons with lifetimes exceeding the repetition rate of Ti:Sapphire oscillator lasers on THz photonic devices was described: they were shown to reduce the overall power of InGaAs and LT-GaAs ph-

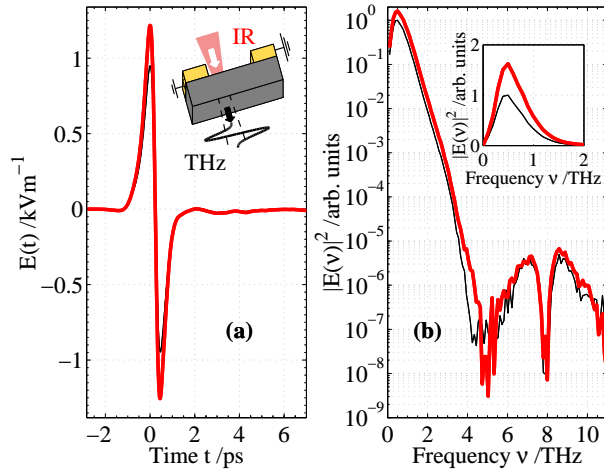


Figure 4.14: (a) Electric field strength of emitted THz pulses from photoconductive switches made on passivated GaAs (thick line) and an etched reference (thin line), as a function of electro-optic delay time. (**Inset**) schematic of experimental geometry, showing the infra-red (IR) emitter pump beam close to the anode of a photoconductive switch, and the radiated THz pulse. (b) Power spectra of THz emission from passivated (thick line) and etched (thin line) GaAs.

to conductive emitters, and to enhance the power transmitted through semi-insulating GaAs photoconductive emitters.

Chapter 5

Charge trapping in polymer transistors

“Electricity is an extream subtle fluid, penetrating other bodies, and subsisting in them, equally diffused.”

Benjamin Franklin, *Of Lightning, and the Method (Now Used in America) of Securing Buildings and Persons from Its Mischievous Effects*, 1767.

5.1 Introduction

A long-overlooked subtlety of electron transport was that a class of organic materials, in particular polymer chains, can sustain an electrical current. The discovery in 1977 that the electrical conductivity of the polyacetylene chain can be tailored between values typical of insulators or metals [141] sparked a flurry of research into conducting polymers, which continues to the present day. The source of the excitement surrounding polymer-based electronics lies in a number of major advantages over traditional inorganic semiconductors. Polymers are inherently flexible, can be easily and cheaply processed from solution, and can be used to create large area devices: properties not typically shared by inorganic semiconductors. Since the demonstration of the first polymer-based light-emitting diode (LED) [142] and the first all-polymer transistor [143] the number of researchers and companies developing polymer electron-

ics has skyrocketed. Recent exciting device demonstrations include flexible full-colour displays, radio-frequency ID tags, and electronic paper [144].

Essential to the implementation of such devices has been the development of the polymer field-effect transistor (pFET), the organic counterpart of the building block of modern electronics. In this chapter a non-contact study of carrier trapping in pFETs is reported, performed using terahertz time-domain spectroscopy. Initially, the physics of electrical conduction in polymers and pFETs is outlined (Sections 5.1.1-5.1.2), before a brief review is given of carrier trapping in pFETs (Section 5.1.3). Subsequently, measurements of the change in THz transmission through pFETs are reported (Section 5.2). It is then demonstrated that the density of trapped holes in the transistor's accumulation layer can be monitored during device operation (Section 5.3): a characteristic that is linked intimately to the degradation of the transistor's performance. This is achieved by coupling the polymer's low-mobility holes to higher mobility electrons in the silicon gate. The correlation of these findings with scanning probe potentiometry measurements (Section 5.1.4) allows for the first time the direct assignment of the contributions to transistor degradation arising from changes in the contact resistance, the field-effect mobility and the trapped carrier density (Section 5.4). Following this, both the response of the transistor to absorption-edge frequency light and the thermal removal of trapped holes are investigated in Section 5.5. Finally, the THz transmission of the devices after dielectric breakdown of the gate insulator is reported in Section 5.6.

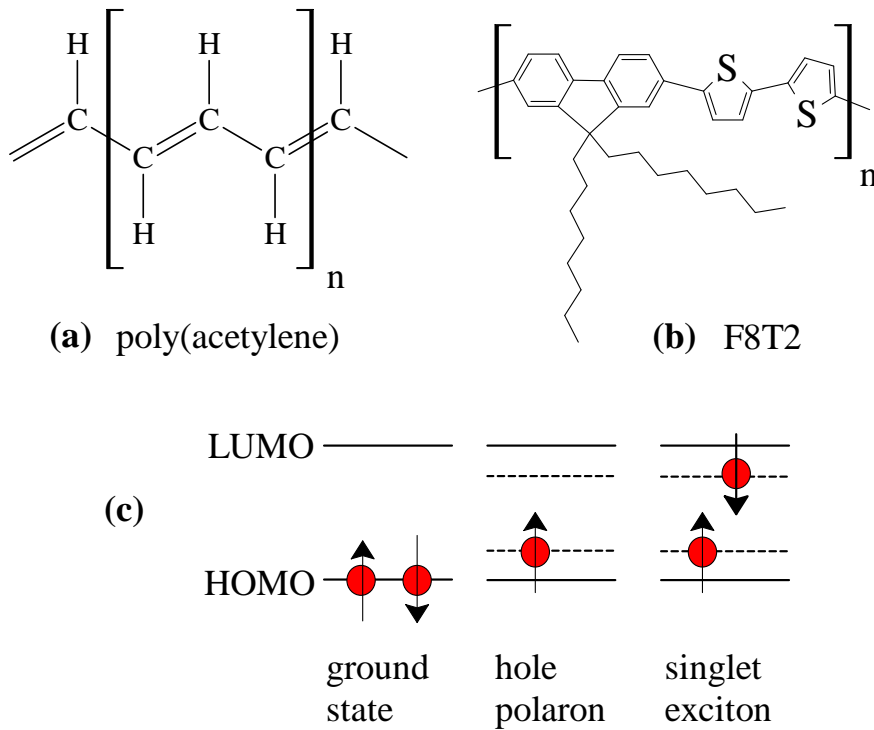


Figure 5.1: (a) Structure of poly(acetylene), a prototypical polymer semiconductor, and (b) the fluorene-thiophene copolymer poly[(9,9-dioctylfluorene-2,7-diyl)-*co*-(bithiophene)] (F8T2). (c) Simple energy diagram of electronic states in a conjugated polymer. In the ground state, the highest occupied molecular orbital (HOMO) level contains two electrons of opposite spin. The removal of one electron creates a hole polaron, with the energy of the remaining electron altered. Alternatively, photoexcitation from the ground state creates a neutral singlet exciton.

5.1.1 Semiconducting polymers

The prototypical semiconducting polymer is polyacetylene, which can be drawn as a sequence of alternating single and double carbon bonds, as in Figure 5.1a. In terms of electron orbitals, each carbon atom has one electron in a σ bond to a hydrogen atom, and three electrons in hybridised sp^2 bonds to the two adjacent carbon atoms. This hybridised system is delocalised along the chain, and is termed the π -conjugated system. A vast variety of polymer systems contain delocalised electrons, for instance poly[(9,9-dioctylfluorene-2,7-diyl)-*co*-(bithiophene)] – or F8T2 – has a delocalised backbone con-

taining both fluorene and thiophene rings (Figure 5.1b).

With increasing energy, the last filled electronic state is termed the *highest occupied molecular orbital* (HOMO), and the first empty level the *lowest unoccupied molecular orbital* (LUMO). Within this picture, schematically shown in Figure 5.1c, the polymer has an energy gap E between HOMO and LUMO levels, typically of a few eV in energy. In the monomer ethylene this energy gap is in the far-ultra-violet at 6.9 eV, while in benzene it is in the near-ultra-violet, at 4.6 eV. The increasing delocalisation of the π -conjugated system results in a lower E , as may intuitively be expected by picturing an electron confined quantum mechanically in a square well [74]. Altering the conjugation length of the system is not, however, the only method of altering E : electron-donating or -withdrawing side groups can change orbital energies [141]. Additionally, forming a co-polymer, which contains two monomer repeat units that would polymerise individually, can allow the engineering of the energy gap. For instance, the polymer F8 (poly[(9,9-dioctylfluorene)]) has $E = 3.3$ eV (HOMO 2.4 eV, LUMO 5.7 eV) but the addition of two thiophene rings (with a lower ionisation potential) to make F8T2 lowers the HOMO-LUMO gap to $E = 2.4$ eV (HOMO 3.1 eV, LUMO 5.5 eV) [145; 146].

While the HOMO-LUMO energy gap is loosely analogous to the bandgap of inorganic semiconductors, the process of charge generation in an organic semiconductor alters the medium's electronic structure. The promotion of an electron from the HOMO level into the LUMO level creates a distortion in the chain's charge cloud, resulting in the alteration of the orbital's other energy levels. The Franck-Condon principle states that the timescale of this electronic response is significantly shorter than the nuclear response, an assumption justified by the light electron mass in comparison to nuclear

masses. Consequently, the resulting charge and distortion can be thought of as a new quasiparticle, the polaron. Schematic energy level diagrams for a hole polaron, and an exciton polaron (a bound electron and hole), are shown in Figure 5.1c. The absorption spectra of most polymers is dominated by excitonic effects: significant absorption occurs at optical frequencies, where tightly-bound (Frenkel) excitons are formed by transitions from the HOMO to the LUMO level and subsequent molecular relaxation. With typical binding energies of a few 100 meV, Frenkel excitons are stable at room temperature ($k_B T = 26$ meV). The optical absorption edge is due to singlet-singlet transitions, since the ground state is a singlet (spin 0 – triplet states have spin 1, and the absorption of a photon does not alter the spin state). Part of the attraction of polymer semiconductors is the ready adjustment of the absorption edge across the visible spectrum, and equally that of the inverse process, electroluminescence.

Charge carriers, necessary for electrical transport, can be created in polymers by a number of mechanisms, including:

1. *Electrical injection* from metallic or semiconductor contacts.
2. *Two-step photoexcitation*. Under intense illumination from mode-locked pulsed lasers the excitons created by single-photon absorption can be excited into a higher state, from which they dissociate into free charges within 150 fs [147].
3. *Dissociation of excitons* into free carriers, either under an electric field, at impurities or at surface interfaces.
4. *De-trapping* of localised (immobile) carriers, for example via a thermally-activated process out of a potential well.

Once a charge carrier is generated it can move along the polymer chain. Charge transport is thought to be a thermally-activated hopping process, with similarities to transport in amorphous inorganic semiconductors. The principal evidence for this view comes from the observation of an enhanced mobility with increasing temperature [141], in stark contrast to the reduction in mobility with temperature typically observed for metals and inorganic semiconductors (Section 3.3.3). Charge transport can thus be viewed as a random walk along a polymer chain, or even between chains if the intrachain coupling strength is sufficiently high. However, it has recently been demonstrated that polyaniline films can exhibit the temperature-dependent conductivity of metals [148] – future work should clarify the interplay and cross-over between the two regimes of charge transport.

5.1.2 Polymer field-effect transistors

The building block of modern electronic devices is the field-effect transistor, which can act as a voltage-controlled switch. In order to construct polymer-based electronic circuitry, equivalent all-polymer transistors need to be created: indeed these were demonstrated first in 1994 [143]. As a beneficial intermediate step, polymer transistors can be made with inorganic semiconductors as the gate, allowing the electrical performance of the polymer to be determined with reference to a better understood system. The following is a brief introduction to the operation of the polymer/inorganic transistor design studied herein: excellent and more general reviews of the fundamentals of polymer field-effect transistors can be found in Refs. [149; 150].

A schematic diagram of the bottom-gate, bottom-contact polymer transistors fabricated for this study is shown in Figure 5.2a. A 100 nm-thick layer of F8T2 was

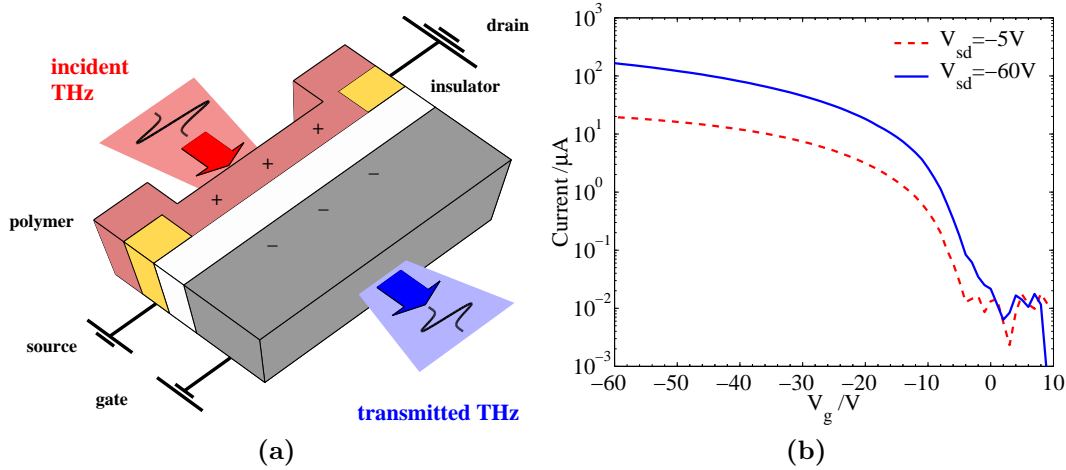


Figure 5.2: (a) Schematic geometry of a bottom-contact, bottom-gate polymer field-effect transistor. Under a negative gate voltage V_g a hole (+) accumulation layer forms in the polymer, and an electron (-) accumulation layer is created in the gate. (b) Source-drain current versus applied gate voltage V_g for a typical pristine pFET, at a constant source-drain voltage $V_{sd} = -5 \text{ V}$ (dotted line) and $V_{sd} = -60 \text{ V}$ (solid line). [Data courtesy of T. Richards, University of Cambridge].

deposited through spin-casting from solution onto an interdigitated gold array, which had a $40 \mu\text{m}$ channel length, $50 \mu\text{m}$ finger width and total channel width 45 mm . A 200 nm -thick layer of SiO_2 electrically insulated the polymer from the gate electrode, which comprised a lightly n-doped silicon wafer ($2.5 \times 10^{15} \text{ cm}^{-3}$) with a total thickness of 0.62 mm .

On the application of a negative voltage V_g to the silicon gate (relative to the source and drain contacts) an electron accumulation layer forms on the boundary between the insulator and the gate. A hole accumulation layer is induced at the same time in the polymer: this is the “channel” of the transistor. The hole and electron layers are mirror charge sheets, and hence have an equal charge density per unit area $n_h = n_e$. If a second voltage V_{sd} is applied between source and drain, holes in the transistor accumulation layer can transport current between the contacts. As Figure 5.2b indicates, a current

of over $100 \mu\text{A}$ flows between source and drain at $V_g = -60 \text{ V}$ and $V_{sd} = -60 \text{ V}$. A significant source-drain current is only obtained when the gate voltage V_g is more negative than a particular threshold voltage V_t , required for the conductive channel to form. This is a characteristic of all pFETs: for these particular devices $V_t = -5 \text{ V}$ (Figure 5.2b).

At positive applied gate voltages, however, no current flows: this is a consequence of the rapid trapping of electrons in the polymer at silanol (Si-O-H) sites on the interface with the SiO_2 gate insulator [146]. Since current flows only with negative gate voltages the pFET is said to exhibit “polar” conduction: “ambipolar” transistors can be fabricated by passivating the SiO_2 surface, allowing electrical transport of both electrons and holes in the polymer [146].

The charge density in the polymer and gate of a pFET can be estimated from the capacitance per unit area $C_{\text{ox}} = 1.73 \text{ F m}^{-2}$ of the gate insulator. At an applied gate voltage $V_g = -30 \text{ V}$, the charge per unit area stored by the insulator is $Q \simeq C_{\text{ox}}V_g$, which results in a hole charge density $n_h = n_e = 3.2 \times 10^{12} \text{ cm}^{-2}$. A more exact treatment can be obtained by solving Poisson’s equation in the vicinity of the polymer/insulator boundary (or the insulator/gate boundary). This is reported in Appendix A.2, and results in an analytical expression for the hole (or electron) charge distribution as a function of gate voltage. The charge distribution obtained using Equation A.13 for a cross-section through the pFET is shown in Figure 5.3. The electron and hole accumulation layers can be seen to be contained predominantly within a few nanometres either side of the insulator. In fact, at $V_g = -30 \text{ V}$, 81% of the total charge density of holes is within 1 nm of the polymer/silicon dioxide interface. At a charge concentration of $N_e = 2.5 \times 10^{15} \text{ cm}^{-3}$, the bulk electrons in silicon have

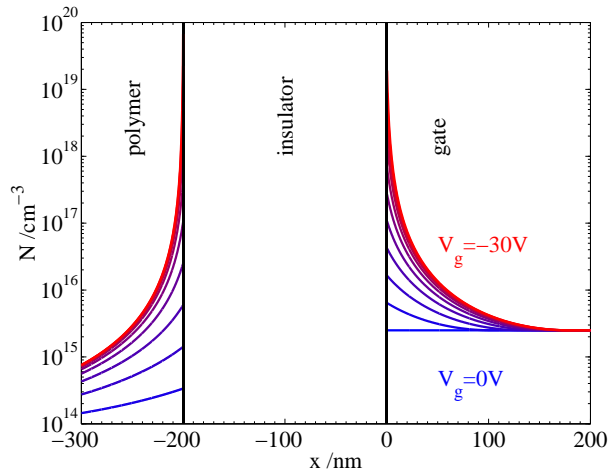


Figure 5.3: Charge density of holes in the polymer, and electrons in the silicon gate (obtained from the analytical solution to Poisson’s equation derived in Appendix A.2) at different applied gate voltages V_g . With no V_g the electron concentration in the gate is equal to the bulk doping level $N_d = 2.5 \times 10^{15} \text{ cm}^{-3}$, and there are no free charges in the polymer. As V_g is made increasingly negative the charge density rapidly increases close to the insulator, with the top curves displaying the concentrations for $V_g = -30 \text{ V}$.

a plasma frequency (Section 2.4.3 and Equation 2.11) of $\omega_p = 0.2 \text{ THz}$, while when $V_g = -30 \text{ V}$, the charge concentration is $N_e = 4.0 \times 10^{18} \text{ cm}^{-3}$ (averaged over the first 8 nm from the surface), resulting in $\omega_p = 8.8 \text{ THz}$.

5.1.3 Trapping in polymer transistors

Two key technological milestones need to be surpassed before polymer transistors achieve commercial viability, loosely termed the short-term and the long-term performance. The first of these is categorised best by the mobility of charge carriers in the polymer. Improvements in polymer processing, surface treatments of gate insulators and the alignment of polymer chains using self-assembled mono-layers have led to high device mobilities [150; 151], which are now competitive with amorphous silicon thin-film transistors. Long-term device degradation mechanisms are increasingly becoming a focus of research, as they are now limiting the commercial application of polymer

transistor technology.

A critical degradation effect is a swing in the threshold voltage of transistor action to ever larger magnitudes during operation [152; 153; 154; 155; 156]. This is thought to be caused by the trapping of holes in either the organic semiconductor or at the semiconductor/insulator interface. Trapped, immobile, holes screen the applied gate voltage, resulting in ever larger gate voltages being required to achieve the same source-drain current. In previous studies of carrier trapping in pFETs, device current-voltage characteristics (such as Figure 5.2b) have been acquired on short timescales (e.g. 1 s) during a period when the gate voltage bias was otherwise kept constant [152; 153; 154; 155; 156]. If the device is modelled as a metal-oxide-semiconductor field-effect transistor (MOSFET), then the threshold voltage and carrier mobility can be extracted from the $I - V$ curves. However, as discussed in Section 5.1.4, such bulk measurements are intrinsically complicated by device effects (e.g. the injection barriers at the contacts), and do not necessarily give direct access to charge transport within the conductive channel of the polymer. It is therefore desirable to use a non-contact technique, such as spectroscopy or potentiometry, to investigate charge trapping and device degradation in pFETs.

In contrast to the delta-function-like density-of-state distributions of traps in inorganic semiconductors, trap states in polymeric systems are broad and are intimately related to the conduction states. A number of mechanisms can influence the mobility of charge carriers in polymers, and act in some sense as traps [157]. The various schemes, in order of increasing trap size, include:

1. *Self-trapping*. A charge carrier on an organic chain deforms the molecule, changing the energy and renormalising the effective mass of the charge. The resultant

charge and deformation can be described as a new quasi-particle, the polaron. If two charge carriers share the same deformation, the quasi-particle is referred to as a *bipolaron*. The timescale for the formation of polarons is the timescale of electrical relaxation, 10-100 fs.

2. *Impurities.* A molecule incorporated in a polymer matrix retains its HOMO and LUMO levels independent of the polymer. If either of these levels happens to fall into the polymer's energy gap, it will form a trap. These can be chemical impurities remaining from the synthesis of the polymer (polymerisation centres).
3. *Geminate pairs.* The low dielectric constant of most polymers means that Coulomb forces between charges are screened only weakly. If both an electron and a hole are present, they can bind, forming a geminate pair typically a few molecules in length. If recombination is sufficiently suppressed, a geminate pair can act as a carrier trap by lowering the local potential energy. Geminate pairs can be formed by the dissociation of excitons under an electric field, or at an impurity site, typically on timescales of 100 fs [158]. Geminate pairs recombine on timescales of 1 ms, as evidenced by the long decay of their fluorescence [159].
4. *Structural defects.* Polymer chains can exhibit strong torsional disorder: the conjugation length of the chain, and the electrical polarisation of the surrounding material, both alter HOMO/LUMO levels, and create a smeared distribution of levels.

Of these trapping mechanisms, interfacial chemical impurities and defects are thought to play a significant role in conduction in pFETs, as may be expected from

the fact that the conductive channel is confined to within a few nanometres of the insulator.

5.1.4 Scanning-probe potentiometry

In many devices the mismatch in workfunction between the source/drain contacts and the polymer creates a “contact resistance”, a potential barrier to charge injection. If this alters during transistor operation, the reliable extraction of meaningful data (for instance the density of trapped charges) solely from current-voltage characteristics becomes a difficult task [160]. As an alternative experimental approach, the local surface potential on operating pFETs can be measured via non-contact potentiometry. Scanning Kelvin-probe microscopy (SKPM) [161; 162] was used to track the electrostatic potential in the accumulation layer of a pFET with a high spatial resolution ($< 100\text{ nm}$). A detailed description of the experimental set-up and the methods employed for data analysis and processing can be found in Ref. [163]. In short, the experimental technique consists of regulating the voltage applied to a conducting tip with a feedback loop, such that the electro-static force between tip and sample is minimised. The resulting tip potential follows the electrostatic potential in the accumulation layer.

The F8T2 transistors investigated were similar to those examined using THz-TDS apart from a reduced channel length ($2\text{ }\mu\text{m}$), owing to the limited translational range of the SKPM tip. Figure 5.4 displays the measured source-drain current I as a function of operating time of the F8T2 transistor. The contact resistance R and channel field-effect mobility $\mu_F = \mu_h n_h$ (where μ_h is the mobility of a hole) can be extracted from the measured potential of the accumulation layer at each time. It can be clearly

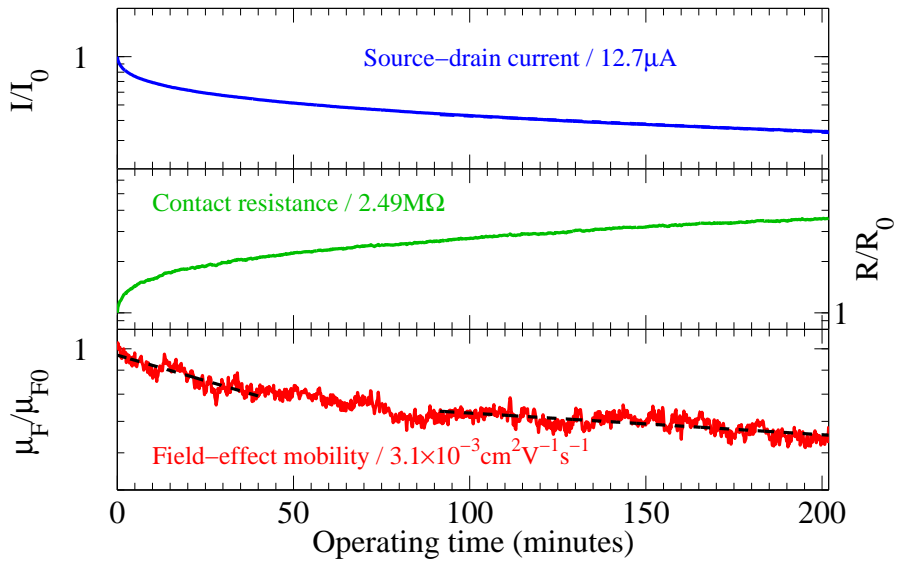


Figure 5.4: Source current (top), source contact resistance (middle) and field-effect mobility μ_F (bottom) of a 2\AA channel length F8T2/300 nm SiO_2/Si pFET as a function of operating time, normalized to their initial values and shown on a semi-logarithmic plot. The curves were extracted from scanning Kelvin-probe microscopy measurements across the transistor channel. A constant gate voltage bias of $V_g = -40\text{ V}$ was applied, to produce an initial sheet charge density $n_h = 2.9 \times 10^{12}\text{ cm}^{-2}$ comparable to that in the THz experiments. The variation in contact resistance with time is accounted for in the extraction of the field-effect mobility. The dotted lines are exponential fits to μ_F at early and late operating times, with time constants $\tau = 1.2 \times 10^4\text{ s}$ and $\tau = 5.6 \times 10^4\text{ s}$ respectively. [Data courtesy of T. Richards, University of Cambridge].

seen that the early non-exponential decay of I is caused by a rapid initial increase of the contact resistance with operating time [164]. The field-effect mobility (the mobility multiplied by the ratio of free charges to total charges) on the other hand, shows an initial exponential decay with a lifetime $\tau = 1.2 \times 10^4\text{ s}$, before tending to saturate at longer operating times. These results demonstrate the difficulty in extracting meaningful information about the dynamics of carrier trapping in pFETs from $I - V$ characteristics, which are significantly influenced by changes in contact resistance [160]. The observed decay of the field-effect mobility may be caused either by a decrease in hole mobility or hole density in the channel. The technique used in

the remainder of this chapter, based on terahertz spectroscopy, is able to measure the hole density independently.

5.2 Terahertz charge modulation spectroscopy

Charge-modulation spectroscopy (CMS), in which an alteration of charge density induces a transmission change to electromagnetic radiation, is a well-established technique in portions of the spectrum away from the terahertz range: CMS in the mid-infrared to visible spectral ranges provided early evidence of the polaronic nature of charge carriers in organic semiconductors [165], and has additionally been applied in the millimetre-wave region to polymer diodes [166]. However, the THz-frequency response of conductive charge layers can provide vital information about the dynamics of carriers in semiconductors, as demonstrated in Chapters 3 and 4, and discussed in Section 1.3.2. In the following, the modulation of the charges in the conductive channel is used to alter the transmission through a pFET in the THz frequency range. Using THz spectroscopy is beneficial, as energies significantly lower than visible photons will not photoexcite extra charges. The use of THz-TDS ensures a much higher signal-to-noise ratio than can be achieved with incoherent spectroscopic techniques, such as FTIR [167].

5.2.1 Setup of experiment

The terahertz time-domain spectrometer described in Chapter 2 was used to measure the THz radiation transmitted through polymer transistors, as schematically shown in Figure 5.2a. A semi-insulating GaAs photoconductive switch biased with a 20 kHz

square wave at $\pm 150\text{ V}$ generated the single-cycle electric-field transient under photoexcitation by pulses from a Ti:Sapphire oscillator laser (10 fs, 75 MHz repetition rate, 400 mW beam power). Electro-optic sampling (with a $200\text{ }\mu\text{m}$ (110) ZnTe crystal on a 6 mm (100) substrate) was used to detect the transmitted transient, using a first lock-in amplifier referenced to the voltage driving the photoconductive switch. To create charge-modulation effects, an a.c. square wave bias voltage V_g was applied to the gate (Figure 5.2a), typically $V_g = 0 \leftrightarrow -30\text{ V}$ at 40 Hz. In this experiment the source and drain contacts were connected to 0 V, and no source-drain current flowed. A second lock-in amplifier was used to measure the change ΔT in the THz electric field T transmitted through the transistors at the frequency of the V_g modulation. The modulation period (0.025 s) was chosen to be significantly longer than both the estimated channel formation time ($\sim 9\text{ }\mu\text{s}$) [168] and the RC time constant created by the contact resistance ($\sim 1\text{ ms}$), in order to eliminate the influence of device capacitance effects. Using a shorter modulation period did not alter the measured differential THz transmission. The THz beam and transistor were kept in a vacuum of 1 mbar to minimize THz absorption from atmospheric water vapor.

5.2.2 Measured THz transmission change

Figures 5.5a and 5.5b display the measured change in THz electric field ΔT under the application of a bias $V_g = 0 \leftrightarrow -30\text{ V}$: it is approximately 1000 times smaller than the size of the electric field T transmitted through the transistor. No transmission changes were observed after the F8T2 layer was chemically removed, or for devices fabricated without the polymer layer.

By plotting $\Delta T/T$, as in Figure 5.6a, it can be seen that on the application of a gate

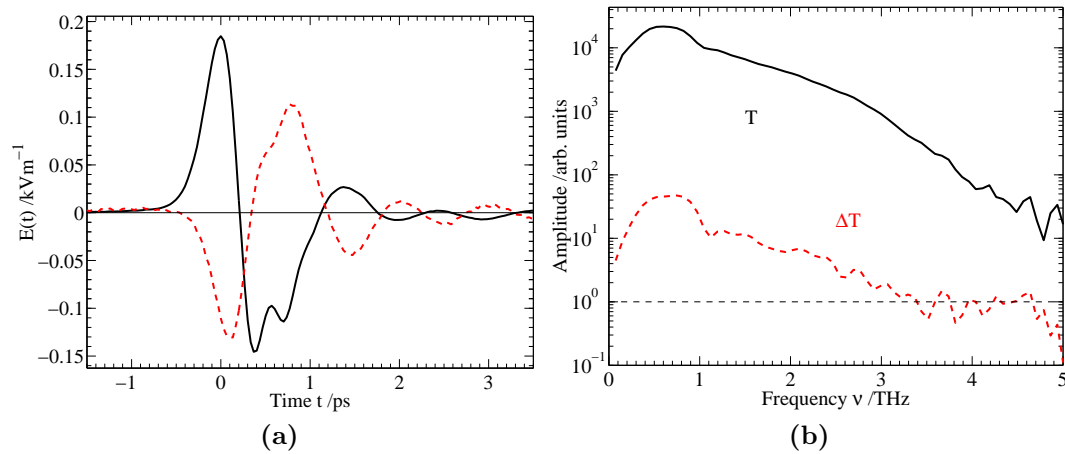


Figure 5.5: (a) Measured THz electric field $T(t)$ after transmission through transistor (solid line) and change in transmitted THz electric field $\Delta T(t)$ (dashed line, multiplied by 100) upon application of a gate voltage $V_g = 0 \leftrightarrow -30 \text{ V}$. Both are given as a function of electro-optic sampling delay time t . (b) Amplitude spectra of the transmitted THz radiation $T(\nu)$, and change in transmitted amplitude $\Delta T(\nu) = T(V_g = -30 \text{ V}) - T(V_g = 0 \text{ V})$ obtained from the time-domain data in a) through Fourier transformation.

bias the transistor transmits less THz radiation (negative $\Delta T/T$) over the entire range of frequencies. This is indicative of the creation of a partially reflective layer, through an increase in the charge carrier density within the transistor. A negative V_g induces both a hole accumulation layer on the polymer/insulator boundary, and an electron accumulation layer of equal surface carrier density on the insulator/gate boundary (Figure 5.3), and therefore both charge sheets should be expected to contribute to the observed $\Delta T/T$. However, the mobility of holes in the polymer's accumulation layer is only $\mu = 7 \times 10^{-3} \text{ cm}^2 \text{V}^{-1} \text{s}^{-1}$ (which can be estimated from the device's current in the saturation regime). This is more than five orders of magnitude lower than the electron mobility in the silicon gate ($\sim 1400 \text{ cm}^2 \text{V}^{-1} \text{s}^{-1}$). Consequently the conductivity of the hole charge sheet is negligible in comparison to that of the electron layer, and therefore the observed $\Delta T/T$ can be attributed entirely to the accumulation layer in

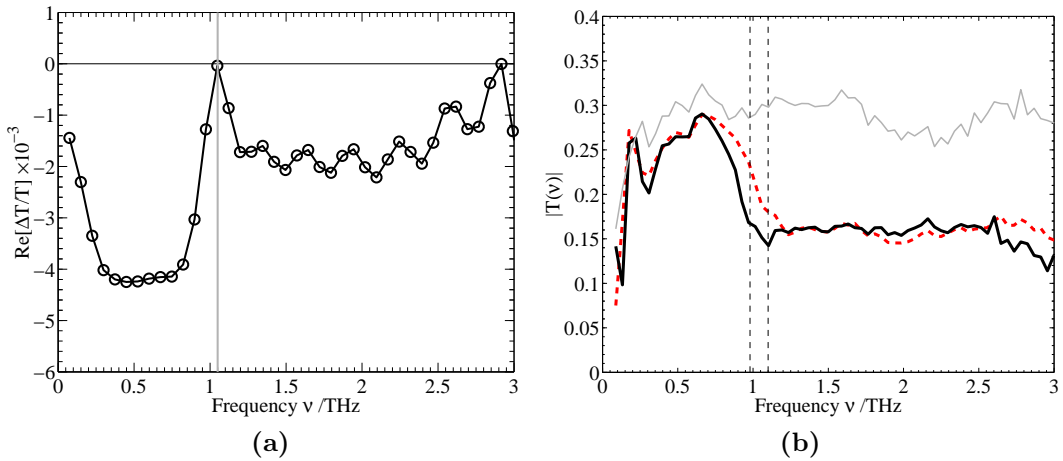


Figure 5.6: (a) Relative change in transmission $\Delta T/T$, calculated from the data in Figure 5.5b. (b) The THz transmission through the silicon substrate (thin solid curve) exhibits a decrease below 0.5 THz owing to the plasma frequency of the gate (0.2 THz). The transmission through a transistor with a grating repeat period of $90\ \mu\text{m}$ (thick solid curve) diffracts THz radiation at lower frequencies than a $80\ \mu\text{m}$ period device (dashed curve).

the silicon. This interpretation was confirmed by an attempt to measure $\Delta T/T$ for an all-polymer transistor, on a quartz substrate: no transmission change was observed, within the experimental noise floor limit of $\Delta T/T < 1 \times 10^{-5}$. For silicon-gate polymer transistors the electron layer in the gate therefore acts as an indirect, but sensitive probe of the hole density in the polymer, by coupling it to higher mobility electrons in the silicon.

As stated in Section 5.1.2, electrons in the accumulation layer in the silicon gate have a plasma frequency $\omega_p = 0.2 \text{ THz}$ when $V_g = 0 \text{ V}$, while $\omega_p = 8.8 \text{ THz}$ when $V_g = -30 \text{ V}$. Since the plasma frequency is above the highest frequency measurable with the spectrometer (3 THz), $\Delta T/T$ should be roughly uniform below ω_p . However, Figure 5.6a indicates that this is not the case: $\Delta T/T$ goes to zero close to 1 THz. The description of the transmission change just discussed requires the following adden-

dum: the gold interdigitated array comprising the transistor's source/drain contacts can act as a diffraction grating at THz frequencies. Rotating the transistor device about its surface normal revealed that maximum transmission (25 % of the incident electric field's peak) occurred when the fingers of the interdigitated array were at 90° to the plane of polarization of the incident THz electric field, as expected for a wire-grid diffraction grating. Furthermore, the repeat period of the array was 90 μm , which corresponds to a frequency of 0.98 THz in vacuum (after accounting for the refractive index of silicon). This results in a first diffraction minimum in $\Delta T/T$ near 1 THz, as indicated by the vertical line in Figure 5.6a, and further reductions at higher frequencies. This interpretation was confirmed by measuring the THz transmission through pFETs with different grating repeat periods. As is shown in Figure 5.6b, a shorter grating period (80 μm) creates a diffraction grating at a higher frequency (1.1 THz).

5.3 Modelling the THz transmission change

In order to relate the measured THz transmission change under gate voltage modulation to the charge density in the transistor in a quantitative manner, a model is now developed based on thin-film optics. Since THz radiation is significantly attenuated by transmission through a 100 nm-thick gold layer (Section 2.4.3) the measured transmitted electric field T can safely be assumed to have passed through the transistor's channel. Data analysis is restricted to the spectral range up to ~ 1 THz, which is unaffected by diffraction.

In Section 3.2.2 the transmission change introduced by a thin charge layer was derived, and it was found that the medium's conductivity is proportional to the trans-

mission change $\Delta T/T$ (Equation 3.10, valid for small $\Delta T/T$). Because the mobility of holes in F8T2 is significantly lower than that of electrons in silicon (Section 5.2.2), the conductivity of the hole layer is negligible. The electron accumulation layer in the silicon gate therefore dominates the transmission change. The response of electrons in silicon to THz radiation can be well described by the dielectric function given in Equation 2.10 (Section 2.4.3). Therefore, the charge density and scattering rate for electrons in the silicon layer can be taken as fit parameters in the transmission model.

The approach adopted to model $\Delta T/T$ was very similar to that of Section 3.2.2, except the incident electric field is taken as that from the insulator into the silicon, rather than from vacuum into the photoexcited sample. The accumulation layer in the silicon gate was assumed to have a constant electron concentration N_e over a thickness $\delta_e = 8 \text{ nm}$ at a particular gate voltage. The electron scattering rate was assumed to be constant, at $\Gamma = 1.5 \times 10^{12} \text{ s}^{-1}$. However, the assumption of a charge sheet of uniform thickness creates unphysically large Fresnel transmission coefficients and Fabry-Perot terms, owing to the discontinuity in refractive index between the accumulation layer and bulk silicon. This problem can be circumvented by assigning the entire change in $\Delta T/T$ to the phase change within the electron charge layer. This corresponds to neglecting the Fresnel transmission coefficients or Fabry-Perot terms, which tend to constants for the more physically-realistic smoothly varying charge distribution encountered in an accumulation layer (Section 5.1.2). With this approximation, $\Delta T/T$ becomes

$$\frac{\Delta T}{T} = \frac{E_{\text{on}} - E_{\text{off}}}{(E_{\text{on}} + E_{\text{off}})/2} = \frac{2(e^{i\phi} - 1)}{e^{i\phi} + 1}, \quad (5.1)$$

where $\phi = (n_{\text{on}} - n_{\text{off}})\delta\omega/c$. The complex refractive index of the electron accumulation layer, and transmitted electric field through the device at V_g were n_{on} and E_{on}

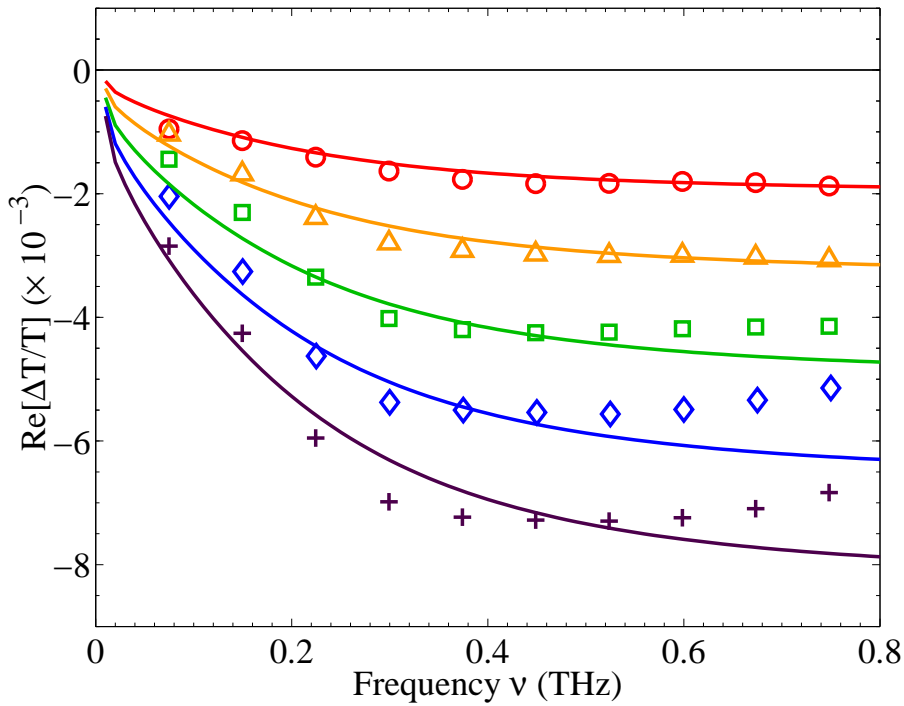


Figure 5.7: Measured differential transmission signal $\Delta T/T$ for a range of gate voltage modulations $0 \leftrightarrow V_g$ with $V_g = -10$ V (circles), -20 V (triangles), -30 V (squares), -40 V (diamonds), and -50 V (crosses). The solid lines are fits to the data based on a Drude-Lorentz thin-film model as described in the text, with $\Delta T/T \propto V_g \propto n_h$.

respectively (and similarly when the device was off, at $V_g = 0$ V).

Using this model, excellent agreement with the experimentally measured $\Delta T/T$ is obtained for an electron accumulation layer density of $N_e^{\text{off}} = 2.5 \times 10^{15} \text{ cm}^{-3}$ in the ‘off’ ($V_g = 0$ V) state and $N_e^{\text{on}} = 4.0 \times 10^{18} \text{ cm}^{-3}$ in the ‘on’ ($V_g = -30$ V) state when $\delta_e = 8$ nm, as shown in Figure 5.7. These parameters agree well with those obtained from the analytical solution of Poisson’s equation at the SiO_2/Si boundary, as discussed in Section 5.1.2 and detailed in Appendix A.2. Assuming that the sheet charge density in the polymer (n_h) is the same as that in the gate (n_e), the hole accumulation layer charge density for a pristine transistor in the ‘on’ state, N_h^{on} , can be calculated from $N_h^{\text{on}} = N_e^{\text{on}}\delta_e/\delta_h$, where δ_h and δ_e are the thickness of the hole

and the electron accumulation layers, respectively. Taking $\delta_h = 1 \text{ nm}$ as a reasonable approximation, $N_h^{\text{on}} = 3.2 \times 10^{19} \text{ cm}^{-3}$ is obtained at $V_g = 0 \leftrightarrow -30 \text{ V}$. These values compare favourably to those typically found in the literature [169].

Experimentally, $\Delta T/T$ is observed to increase linearly with the applied gate voltage (Figure 5.7), in accordance with an increase of charge density in the channel. Using identical parameter values to those determined above for $V_g = -30 \text{ V}$, but scaling n_e and δ_e linearly with gate voltage, results in model curves closely matching the measured $\Delta T/T$ over the entire range of applied V_g , as Figure 5.7 also illustrates. In summary, the THz transmission change under gate voltage modulation can be used to probe the charge density of the conductive channel of a silicon gate pFET.

5.4 Hole trapping in the accumulation layer

The sensitivity of the technique just outlined to the hole density in the transistor channel makes it an ideal tool, in particular to investigate the mechanisms governing device degradation under the prolonged application of a gate bias voltage. $\Delta T/T$ was measured as a function of biasing time at $V_g = 0 \leftrightarrow -30 \text{ V}$ for a number of transistors. As revealed in Figure 5.8a, $\Delta T/T$ decreases exponentially for approximately the first hour, after which it gradually saturates. The time constant of this decay is $\tau = 7.1 \times 10^3 \text{ s}$, and is comparable to that of the decay in conductivity obtained from the SKPM data $\tau = 1.2 \times 10^4 \text{ s}$ (Section 5.1.4). The decay in $\Delta T/T$ can be attributed to an increase in density of trapped holes at the polymer/insulator interface with time, resulting in a larger hole density n_h^{off} in the ‘off’ state, and therefore also an increased n_e^{off} : trapped holes remain in the channel and thus reduce ΔT . This situation is shown

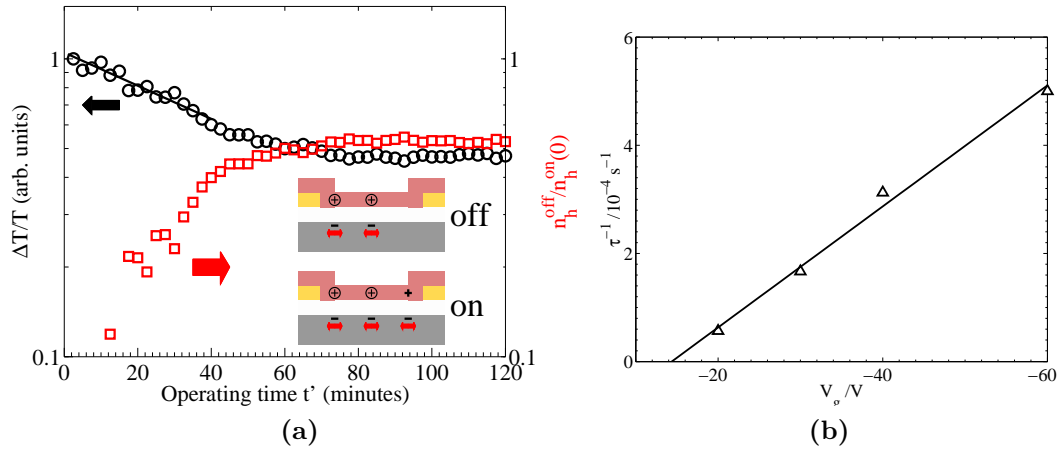


Figure 5.8: (a) When $V_g = 0 \leftrightarrow -30 \text{ V}$ is applied for times t' (half the measurement time, owing to the 50% V_g duty cycle) the differential transmission (circles) decays initially exponentially (straight line). The time constant $\tau = 7.1 \pm 2.4 \times 10^3 \text{ s}$ of this decay was determined by averaging fits for three nominally identical transistors, over the first 40 minutes. The trapped charge density remaining in the channel during the off period, $n_h^{\text{off}}(t')/n_h^{\text{on}}(0)$ (squares, extracted from the modelled fits to $\Delta T/T$, with charge density $n_h^{\text{on}}(0) = 3.2 \times 10^{12} \text{ cm}^{-3}$ when on) saturates at large t' . (**Inset**) Cartoon of the proposed mechanism for the reduction in $\Delta T/T$. (b) Hole trapping rate $1/\tau$ obtained from exponential fits to $\Delta T/T$ during application of $0 \leftrightarrow -V_g$ for 30 minutes.

schematically in the inset to Figure 5.8a. A change in hole mobility in the polymer cannot contribute to a change in THz transmission, as the hole accumulation layer does not have a sufficiently high conductivity (Section 5.2.2). The differential change in transmission $\Delta T/T$ is therefore proportional to the mobile hole density, $n_h^{\text{on}} - n_h^{\text{off}}$ (Equation 3.10).

The observed initial exponential decay of $\Delta T/T$ indicates that the hole trapping rate in the polymer is a linear function of the mobile hole density, i.e. $dn/dt = -n/\tau$. This finding is incompatible with the bipolarionic trapping mechanism that has recently been proposed as a contributor to device degradation on timescales below 1 s [153; 154], which predicts that $dn/dt \propto n^2$.

Figure 5.8a also displays the trapped hole density n_h^{off} as a function of operating

time, as extracted from the data using the model described in Section 5.3, under the assumption that all other parameters are unaffected by degradation. The hole density for the ‘off’ state increases considerably within the first hour, but then saturates at a value of approximately half that of the initial value in the ‘on’ state, $n_h^{\text{on}}(0)$. This saturation is a result of the finite density of hole traps on the polymer/insulator interface, estimated at $1.5 \times 10^{12} \text{ cm}^{-2}$ from the limit of this change. Assuming that these traps lie within 1 nm of the insulator, the concentration of traps is $1.5 \times 10^{19} \text{ cm}^{-3}$. The trapping cross-section can be estimated from the decay rate $1/\tau$ via the Shockley-Read-Hall model (Section 3.1.4) as $\Sigma = 5 \times 10^{-35} \text{ m}^2$, where the thermal velocity (Equation 3.2) was calculated assuming a hole effective mass of $m^* = m_e$. This value of Σ is tiny in comparison to other cross-sections in semiconductor physics (e.g. $\Sigma \sim 10^{-14} \text{ m}^2$ for electron-impurity scattering), as befits the extremely slow trapping rate.

In Figure 5.8b the initial trapping rate $1/\tau$ is extracted from exponential fits to the initial decay over the first 20 minutes, at a number of applied gate voltages. It can be seen that $1/\tau$ is linearly proportional to the applied gate voltage. Applying the Shockley-Read-Hall model, this rise in $1/\tau$ suggests that the trapping cross-section or the trap density (or both) increase with gate bias. While this trend has been seen previously [154], a definitive physical explanation is not immediately forthcoming. It is possible that at higher fields the extra charge density distorts the polymer more significantly, increasing the trap density and cross section.

5.5 Removal of trapped holes

Having demonstrated that charge modulation spectroscopy in the THz range can track hole trapping in pFETs, an investigation of the reverse process is reported in this section. Previous studies have found that the threshold voltage of F8T2 pFETs returns to its initial (pre-trapping) value if the device is left in the dark with no bias applied [152; 155], with shorter recovery times at elevated temperature [170]. The recovery of devices is attributed to the thermal excitation of holes out of their traps, and is a slow process at room temperature, typically taking hours to return to their pristine condition [152]. In the experiments above, the period of the V_g modulation was too short to obtain significant carrier de-trapping during the ‘off’ state of the cycle.

Another reported method of removing trapped holes is the illumination of the polymer with photons of above bandgap energy [152; 163]. While a definitive mechanism remains to be established, it has been proposed that the electron part of a photoexcited exciton can recombine with a trapped hole, leaving the remainder of the exciton: a mobile hole [163].

In the following, results are presented concerning the thermally-activated removal of trapped holes and the effect of illumination on a pFET, via the THz spectroscopy technique outlined above. In order to prepare transistors with the same initial conditions, a gate voltage modulation of $V_g = 0 \leftrightarrow -30\text{ V}$ was applied to a set of pristine transistors for 2 hours, to fill the trap states. The change in the peak THz time-domain electric field (at zero electro-optic delay time) was then recorded every 2 s, enabling the hole density to be tracked on shorter timescales. This recorded value is essentially the transmission change averaged over the spectral range of the THz pulse: a larger

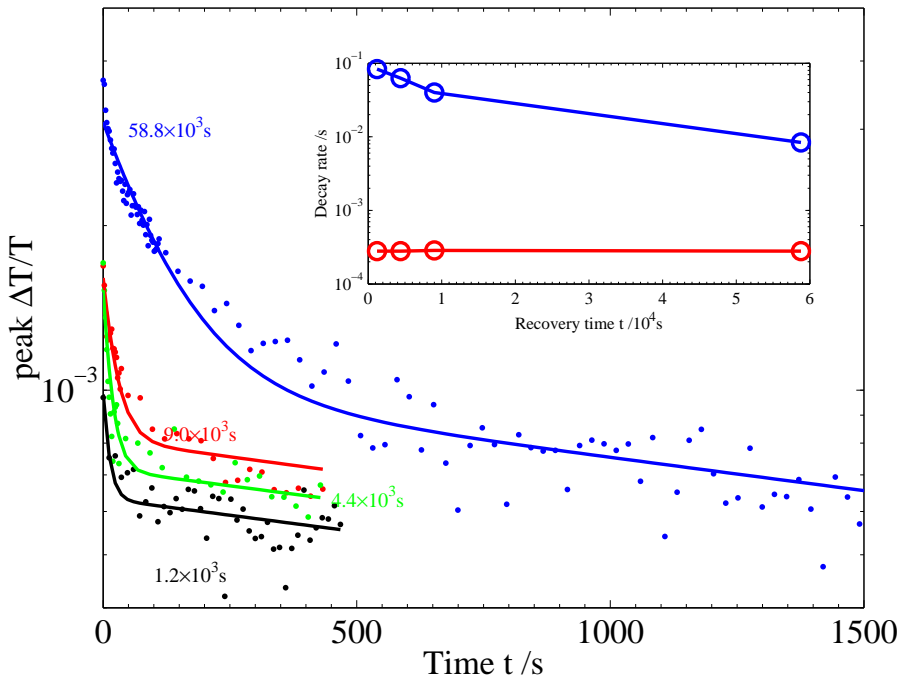


Figure 5.9: Decay in transmission change $\Delta T/T$ for a pFET as a function of measurement time, after different periods where the pFET was left with no gate voltage for (dots, from bottom to top, respectively) 1.2×10^3 s, 9.0×10^3 s, 4.4×10^3 s and 5.9×10^4 s. The transmission change is proportional to the mobile hole density, and can be fit well by a two-exponential decay of the form $n_h = n_1 \exp -t/\tau_1 + n_2 \exp -t/\tau_2$ (solid lines). (**Inset**) The lifetimes τ_1 (red) and τ_2 (blue) of the slow and fast decay as a function of recovery time (see text for discussion).

transmission change indicates a greater difference in hole density between ‘on’ and ‘off’ states, as previously.

5.5.1 Thermal detrapping

The thermal removal of trapped carriers was investigated as follows. A set of transistors was left under vacuum with no V_g applied (and in the dark, with a recorded power < 1 nW at 530 nm, the absorption edge of F8T2) for a set time period. After this time, the gate voltage modulation was switched back on, and the change in THz electric field was recorded, allowing the trapping dynamic to be determined. Figure 5.9 illustrates

the measured decrease in $\Delta T/T$ for a device left to recover for different durations, up to 6×10^4 s. As the device is left to recover for ever longer times, the decay in $\Delta T/T$ becomes more like the decay of a pristine transistor (Section 5.4). However, an additional, faster, decay component is now visible, owing to the higher time resolution of these measurements. The mobile hole density, which is proportional to $\Delta T/T$, can be modelled well via two separate exponential decays, i.e. $n_h = n_1 \exp(-t/\tau_1) + n_2 \exp(-t/\tau_2)$ (solid lines in Figure 5.9): a slow decay τ_1 , as reported above, and a faster decay τ_2 . This may be indicative of the thermal de-trapping of holes from shallow and deep traps, since the probability p_i for thermal excitation out of a trap is highly dependent on its energy barrier Δ : $p_i \propto \exp(-\Delta/k_B T)$.

Interestingly, the lifetime of the fast decay τ_2 increases with the recovery time, as the inset of Figure 5.9 shows, while the slow decay τ_1 remains constant. Since shallow traps should be depopulated more rapidly than deep traps, changes to the fast decay may therefore be tentatively attributed to the population of shallow traps. Assuming that the concentration of traps N_t remains constant, the SRH model (Section 3.1.4) predicts that the cross-section for the fast decay must decrease with recovery time, in order to produce the measured change in $1/\tau_2$. This implies that the creation of trapped holes increases the trapping rate for the shallow (fast decay) traps, perhaps by further deforming the polymer chain.

5.5.2 Above absorption-edge illumination

Additionally, the effect of illumination on THz transmission through a pFET was investigated. The hole traps of pFETs were first saturated, before shining light from various high-power LEDs uniformly onto the polymer. Figure 5.10 indicates that the

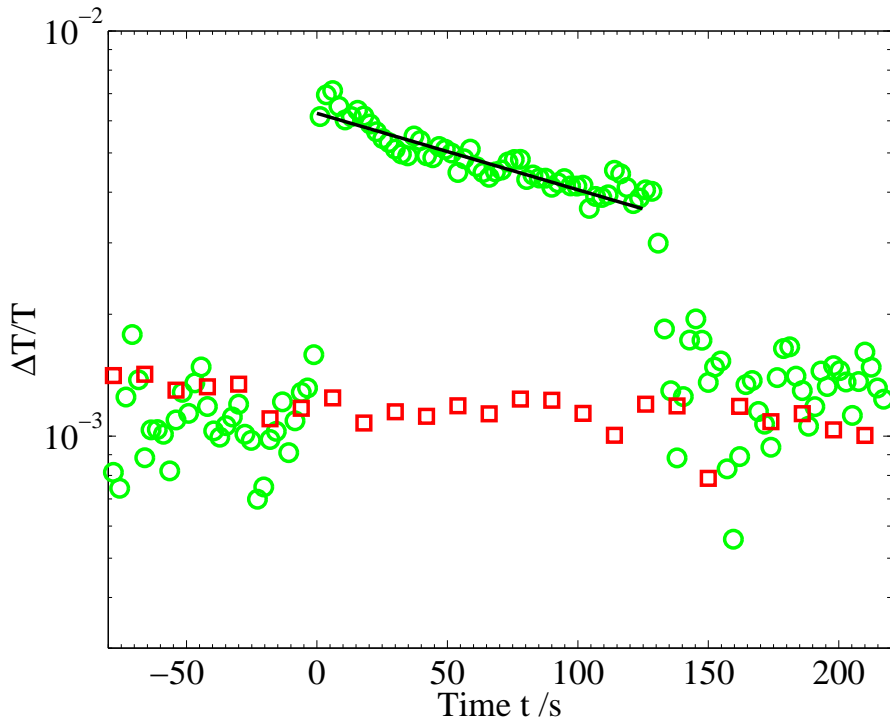


Figure 5.10: The change in transmission ($\Delta T/T$) of the THz electric field through a pFET at a gate voltage $V_g = 0 \leftrightarrow -30$ V. Initially the transmission change is constant, as the trapped hole density has saturated. At zero time the transmission change increases markedly when a high-power green LED is switched on (530nm, circles), while with a red LED of comparable power (655nm, squares) no change is observed.

transmission change $\Delta T/T$ does not alter when light from a red LED (wavelength 655 nm, spectral width ± 30 nm, intensity 1.3 W m^{-2}) is incident on the transistor. However, illumination with a green LED (wavelength 530 nm, spectral width ± 30 nm, intensity 2.6 W m^{-2}), alters the THz transmission: a large step in $\Delta T/T$ is visible at zero time, when the LEDs were switched on. The transmission change $\Delta T/T$ then reduces in magnitude, approximately exponentially, with time constant 230 s. The LED was switched off at 128 s, after which $\Delta T/T$ rapidly returns to its pre-illumination value.

The origins of the various features in the light-induced change in $\Delta T/T$ will now

be discussed. The rapid increase in $\Delta T/T$ at zero time could be a result of the rapid removal of trapped holes, within the 2 s measurement period. The removal of a large fraction of trapped holes would create a large $\Delta T/T$ by decreasing the hole density during the ‘off’ period of the V_g modulation. However, this interpretation is not consistent with the rapid return in $\Delta T/T$ to its initial value when the illumination is removed (within 2 s) – a permanent decrease in the concentration of trapped holes would result in a decay dynamic similar to those in Figure 5.9. An alternative explanation is that the density of holes in the polymer accumulation layer is increased under illumination. As the energy of incident photons is below that required to create carriers directly, excitons are the primary photoexcitation. A mechanism of exciton dissociation into hole and electron polarons is therefore required: possibilities include exciton dissociation at defects, interfaces and under an electric field [157; 158].

The latter possibility, field-induced exciton dissociation, is a plausible candidate. Under a large electric field ($> 10^7 \text{ V m}^{-1}$) the electron and hole of an exciton can be spontaneously separated, forming a geminate pair [158]. This requirement is met for these pFETs: the electric field strength close to the insulator can be calculated from the solution to Poisson’s equation presented in Appendix A.2, and decreases from 10^8 V m^{-1} at the polymer/insulator interface down to 10^7 V m^{-1} by 5 nm into the polymer. A further requirement is that the yield of dissociated excitons must be high enough to produce the measured $\Delta T/T$ change. The photogenerated exciton density in the channel can be estimated by integrating the photon absorption distribution using the absorption coefficient of F8T2 at 530 nm, $\alpha = 1.5 \times 10^6 \text{ cm}^{-1}$. Assuming a typical value for the quantum efficiency of the conversion of excitons to free charges of 10^{-4} , [158] the photogenerated hole and electron density within 5 nm of the insulator

is of the order of 10^{12} cm^{-2} . This is of the necessary size to produce the observed rise in $\Delta T/T$. Within this interpretation, the decay in $\Delta T/T$ (between $t = 0 \text{ s}$ and $t = 128 \text{ s}$, Figure 5.10) can be explained via the formation of geminate pairs, which will screen the applied gate voltage, thus reducing the electric field and the yield of charges. Furthermore, the rapid ($< 2 \text{ s}$) return to the original value of $\Delta T/T$ can be explained as a consequence of the recombination of the geminate pair population, which takes $\sim 1 \text{ ms}$ [159]. Further experiments of the dependence of such $\Delta T/T$ changes on light intensity and applied electric field should reveal whether exciton dissociation, or some other mechanism, is responsible for the light-induced transmission change reported here.

5.6 Dielectric breakdown of transistor

An additional long-term device performance issue faced by both polymer- and silicon-based transistors is the dielectric breakdown of the gate insulator. A small leakage current can flow from the source/drain through the insulator to the gate, and charges can be trapped at defects in the insulator. Over a transistor's lifetime the build-up of trapped charge eventually results in the runaway breakdown of the dielectric, in which large currents heat and weaken the insulator layer until it short-circuits. At sufficiently high electric fields (close to 1 GV m^{-1} in silicon dioxide) dielectric breakdown can occur spontaneously. The degradation and eventual breakdown of insulating thin-films is of critical importance in the drive to produce ever smaller MOSFET devices [171; 172]: oxide layers are approaching nanometre thicknesses, where quantum mechanical tunnelling through the insulator can contribute to the leakage current. Gate insulators

with higher dielectric constants, and lower leakage current, are currently a focus of intense research in the inorganic semiconductor device community [173], in efforts to ensure the continuing minaturisation of the silicon transistor. In this section the consequences of dielectric breakdown on the THz transmission through pFETs are discussed.

The THz radiation transmitted through five transistor devices was measured at a variety of d.c. gate voltage biases V_g in the range -60 V to +60 V. Initially, no change in transmission was recorded in comparison with the transmission when $V_g = 0$ V, and the leakage current flowing through from source/drain to gate was ~ 1 nA. After biasing at $V_g = -60$ V for significant timescales (about three hours), however, the transmitted THz electric field altered noticeably, and the leakage current jumped to ~ 10 mA. These changes are indicative of the time-dependent dielectric breakdown of the insulator, as may be expected since the applied electric field across the 200 nm-thick SiO_2 (0.3 GVm^{-1}) is close to the spontaneous breakdown field.

The spectral amplitude of the transmitted THz electric field after dielectric breakdown is shown in Figure 5.11a, at $V_g = 0$ V and $V_g = -60$ V. On the application of the gate bias an increase in the transmitted THz field can be seen close to 0.2 THz, and a decrease above 1 THz. This can be more clearly seen by plotting the real part of the transmission change, defined as $\Re\{\Delta T/T\} = \Re\{[T(-60 \text{ V}) - T(0 \text{ V})]/T(0 \text{ V})\}$. This was experimentally demonstrated to be a consequence of the resistive heating of the transistor: the large current (~ 10 mA) at $V_g = -60$ V results in the dissipation of roughly 0.6 W of heat in the device. Since measurements were performed in vacuum, and the transistors were thermally isolated, the rate of heat dissipation is low, and the pFET may be expected to reach thermal equilibrium at a higher tem-

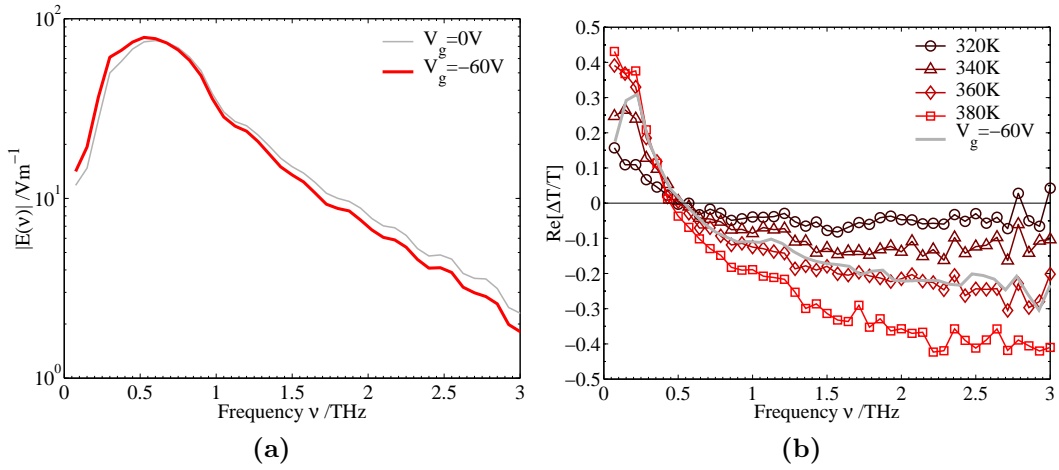


Figure 5.11: (a) Amplitude of THz electric field transmitted through a pFET when $V_g = 0\text{V}$ (thin line) and $V_g = -60\text{V}$ (thick line). (b) Real part of change in transmission between $V_g = -60\text{V}$ and $V_g = 0\text{V}$ (thick grey line, no symbols). Similarly, the change in transmission relative to room temperature is shown for transistor temperatures of $\Theta = 320\text{K}$ (circles), 340K (triangles), 360K (diamonds) and 380K (squares).

perature Θ . The influence of the transistor's temperature on the THz transmission was categorised using a temperature controller consisting of heating resistors and a commercial temperature sensor (LM335). As Figure 5.11b indicates, the change in transmission $\Delta T/T = [T(\Theta) - (296\text{K})]/T(296\text{K})$ matches the change in transmission between $V_g = 0\text{V}$ and $V_g = -60\text{V}$ when $\Theta = 360\text{K}$.

5.7 Summary

In conclusion, the mechanisms for degradation of polymer-based FETs were investigated using a novel THz spectroscopy technique. The observed change in THz transmission on application of a gate bias is caused by a layer of high-mobility electrons that forms in the silicon gate as mirror charges to the lower-mobility hole accumulation layer in the polymer. During the ‘on’ state of the transistor, the plasma frequency of

the electron layer is shifted upwards in frequency, permitting highly sensitive, non-contact probes of the accumulated charge density through THz-TDS. The measurements demonstrate an initial mono-exponential decrease of the THz differential transmission signal with biasing time, owing to an increase in the trapped charge density in the polymer, present also during the ‘off’ state. By being sensitive only to electrons in the silicon gate, the THz-TDS measurements are not influenced by the hole mobility in the polymer. The comparison of the results from THz-TDS with potentiometry measurements (carried out by collaborators at the University of Cambridge) confirms that an increase in trapped-charge density, rather than a decrease in single-carrier mobility, is responsible for the decline in the conductivity of the channel with operation time.

Chapter 6

Conclusion

This thesis reported an investigation into the trapping of charge carriers in semiconductors, undertaken with time-domain spectroscopy techniques in the terahertz region of the electromagnetic spectrum. Two extremes of trapping lifetime were reported: in inorganic semiconductors electron lifetimes ranged from $< 1\text{ ps}$ (for instance in ion-implanted InP) to 48 ns (in semi-insulating $\text{In}_{0.53}\text{Ga}_{0.47}\text{As}$), while in polymer transistors hole lifetimes exceeded 1000 s . In this chapter the key findings reported in this thesis are briefly reviewed, before suggestions are given for future work within this field.

Chapter 2 introduced the technique of terahertz time-domain spectroscopy, and gave examples of its use. The phonon-polariton dispersion created by the TO-phonon mode of the polar crystal CsI was measured, as were the complex refractive index of a free electron plasma in silicon, and the molecular rotational modes of atmospheric water vapour. Additionally, the performance of band-pass filters in the THz range (fabricated from waveguide array plates) was assessed.

The ultra-fast dynamics of photoexcited electrons in semiconductors was investigated via optical-pump terahertz-probe spectroscopy (Chapter 3), and also using

terahertz emission spectroscopy (Chapter 4). The relative photoexcitation times in GaAs, InGaAs and InAs were compared, and related to the intravalley scattering of nonequilibrium carriers. The diffusion of electrons away from the surface allowed the relative influence of surface and bulk recombination to be assessed for GaAs samples in which the surface states were passivated. Materials suitable for ultra-fast optoelectronics were investigated, including low-temperature-grown GaAs, and ion-implanted InP, GaAs and InGaAs. Sub-picosecond lifetimes were observed to produce greater emitted THz power at higher frequencies in the terahertz range, a finding reproduced quantitatively by carrier dynamics simulation work. An enhancement in the power of terahertz radiation emitted from photoconductive switches fabricated on passivated GaAs was reported, and was attributed to the measured conductivity increase.

In Chapter 5 the trapping of holes within the accumulation layer of a polymer transistor was reported, as monitored via a novel charge modulation technique based on terahertz time-domain spectroscopy. High mobility electrons within the silicon gate of a transistor were coupled electrostatically to low mobility holes in the polymer, and altered the transmission of the device to terahertz radiation. A simple transmission model allowed the extraction of the hole density in the polymer, agreeing well with that expected from an analytical solution to Poisson's equation. After a gate voltage was applied to the transistors for many minutes the trapped hole density in the polymer was observed to increase, with a rate indicative of polaronic charge carriers. Finally, the thermal detrapping of carriers and the influence of above-bandgap illumination were studied.

6.1 Future prospects

A number of studies could extend upon the work reported in this thesis. In order to understand better the thermal removal of trapped holes in polymer transistors, a study such as presented in Section 5.5.1 could be carried out at various temperatures. If the temperature dependence of the trapping or detrapping rate were to be obtained, then an Arrhenius plot (Section 3.5.1) ought to yield the activation energy for the fast and slow trap states, providing insights into their placement between the HOMO and LUMO bands. Optical-pump mid-infrared-probe spectroscopy of trapped holes in polymer transistors might reveal the timescale on which illumination with above bandgap energy photons alters the carrier density in the transistor, for instance by the dissociation of excitons.

Further scope exists for the improvement of both the power and frequency range of photoconductive THz emitters. The combination of THz emission studies (from surfaces or photoconductive switches), with conductivity data gleaned from optical-pump THz-probe spectroscopy, ought to enable the optimisation of ion-implantation parameters to create a material with an ideal carrier mobility and lifetime. Alternatively, advanced nanostructured materials, for instance quantum dots embedded in a high mobility substrate, could be investigated. One such initial study has been reported by Prasankumar *et al.* [47]. The overall radiated THz power from photoconductive switches may be enhanced further by an improved surface passivation technique. The Monte Carlo simulation used herein could be extended to include surface recombination effects, providing an accurate model of the influence of surface defects on ultrafast carrier dynamics.

The recent demonstration of a photoconductive detector of THz radiation capable of simultaneously recording orthogonal polarisation states[71] opens up new possibilities for THz spectroscopy. In particular, time- and polarisation-resolved spectroscopy in the far- and mid-infrared ought to yield invaluable insights into the dynamics of charge carriers in biomolecules, polymeric compounds and anisotropic semiconductors.

More generally, the development of time-domain spectrometers that can operate outside the laboratory, for example using Er:fibre-based setups, ought to enable diverse applications of this technique in environments that are otherwise inaccessible. Fibre-coupled spectrometers should enable THz spectroscopy within confined and/or extreme environments, such as within a pulsed magnetic field, an endoscope, or within an experimental fusion reactor.

Appendix A

Electromagnetism

In this appendix a brief overview is given of the key results of electromagnetism utilised in this thesis. The relationship between the complex refractive index, conductivity and wavevector for a material is outlined. Additionally, Poisson's equation is solved at a semiconductor/insulator interface, which is a result used in Chapter 5.

A.1 Linear electromagnetism

Maxwell's equations of electromagnetism within a non-magnetic ($\mu_r = 1$) medium with a linear dielectric function ϵ_r relate the electric \mathbf{E} and magnetic \mathbf{B} fields via:

$$\nabla \cdot \mathbf{E} = \frac{\rho}{\epsilon_r \epsilon_0} \quad (\text{A.1})$$

$$\nabla \cdot \mathbf{B} = 0 \quad (\text{A.2})$$

$$\nabla \times \mathbf{E} = -\frac{\partial \mathbf{B}}{\partial t} \quad (\text{A.3})$$

$$\nabla \times \mathbf{B} = \mu_0 \mathbf{J} + \mu_0 \epsilon_r \epsilon_0 \frac{\partial \mathbf{E}}{\partial t}, \quad (\text{A.4})$$

where ρ is the charge density (per unit volume), and the current density $\mathbf{J} = \sigma \mathbf{E}$ where σ is the conductivity.

Taking $\nabla \times$ (A.3) and using the identity $\nabla \times (\nabla \times \mathbf{E}) = \nabla(\nabla \cdot \mathbf{E}) - \nabla^2 \mathbf{E}$ results in the equation:

$$\nabla^2 \mathbf{E} = \mu_0 \sigma \frac{\partial \mathbf{E}}{\partial t} + \mu_0 \epsilon_r \epsilon_0 \frac{\partial^2 \mathbf{E}}{\partial t^2} + \frac{\nabla \rho}{\epsilon_r \epsilon_0}. \quad (\text{A.5})$$

To solve this equation plane wave solutions propagating in the z direction, of the form $\mathbf{E}(z, t) = \mathbf{E}_0 e^{i(kz - \omega t)}$, can be found. This requires that $\nabla \rho = 0$, which is satisfied for insulating media (where $\rho = 0$), and for other media when $\rho \neq \rho(z)$. The substitution of $\mathbf{E}(z, t)$ in (A.5) produces:

$$k^2 = i\omega \mu_0 \sigma + \epsilon_r \frac{\omega^2}{c^2}, \quad (\text{A.6})$$

where use has been made of the relation $c^2 = 1/\epsilon_0 \mu_0$. In the case of a non-conductive medium $\sigma = 0$, and the dispersion relation $k(\omega) = n\omega/c$ is obtained. If $\sigma \neq 0$, one can define a complex refractive index \tilde{n} such that $k(\omega) = \tilde{n}\omega/c$. Consistency with this complex dispersion relation requires that $\tilde{n} = \sqrt{\epsilon}$, where the complex dielectric function ϵ is:

$$\epsilon = \epsilon_r + i \frac{\sigma}{\epsilon_0 \omega}. \quad (\text{A.7})$$

The definition $\epsilon(\omega \rightarrow \infty) = \epsilon_\infty$ results in:

$$\epsilon = \epsilon_\infty + i \frac{\sigma}{\epsilon_0 \omega}. \quad (\text{A.8})$$

This general relation allows us to relate the electrical conductivity of a medium to its complex refractive index, obtained via transmission or reflection spectroscopy. Writing the complex refractive index $\tilde{n} = n + i\kappa$, the real part is the material's refractive index, and the imaginary part is related to the intensity absorption coefficient $\alpha = 2\omega\kappa/c$.

A.2 Charge density in an accumulation layer

In Chapter 5 the THz transmission through a polymer transistor is related to the electron charge density in the silicon gate. In this section the charge distribution expected in the silicon is calculated by treating the transistor as a metal-insulator-semiconductor structure. In the following Poisson's equation is solved for the electron accumulation layer formed in an n-type semiconductor when a gate voltage V_g is applied to the metal. A similar treatment can be performed for electron or hole accumulation or depletion layers.

The total charge density in a semiconductor is $\rho = q(P - N + N_D - N_A)$, where the concentrations of holes, electrons, donors and acceptors are respectively P , N , N_D and N_A , and $-q$ is the electron charge. For an n-type semiconductor $N_D \gg N_A$, and in equilibrium without significant hole injection $N \gg P$. For charge distributions with an accumulation layer of electrons in the semiconductor (near the boundary with the insulator) one can assume that $N \gg N_D$, and consequently $\rho = -qN$. The electrostatic potential Φ is defined such that $\Phi(x) > 0$, $\Phi(x = 0) = \Phi_s$ at the insulator/semiconductor boundary, and $\Phi(x = x_{acc}) = 0$ at some distance x_{acc} away from this interface. The gradient of the potential is also set to zero at x_{acc} .

In one dimension, substituting the electric field $E = -\nabla\Phi = -d\Phi/dx$ into Equation A.1 produces:

$$\frac{d^2\Phi(x)}{dx^2} = -\frac{\rho}{\epsilon_{Si}\epsilon_0} = \frac{qN_D}{\epsilon_{Si}\epsilon_0} \exp \frac{q\Phi}{k_B T}, \quad (\text{A.9})$$

where the silicon has dielectric constant $\epsilon_{Si} = 11.7$ and donor concentration $N_D = 2.5 \times 10^{15} \text{ cm}^{-3}$ for the transistors in Chapter 5.

Multiplying both sides of Equation A.9 by $2d\Phi/dx$ produces a form that can be

readily integrated from x to x_{acc} to obtain the electric field produced by the charge layer:

$$E(x) = -\frac{\sqrt{2} k_{\text{B}} T}{L_d q} \sqrt{\exp \frac{q\Phi}{k_{\text{B}} T} - 1}, \quad (\text{A.10})$$

where the Debye length L_d characterises the thickness of the accumulation layer, and is defined as:

$$L_d = \sqrt{\frac{\epsilon_{\text{Si}} \epsilon_0 k_{\text{B}} T}{q^2 N_D}}. \quad (\text{A.11})$$

Equation A.10 can be integrated to get the potential Φ , by making use of the substitutions $u = \exp(q\Phi/k_{\text{B}}T)$ and $u = \sec \theta = 1/\cos \theta$, and the boundary conditions for Φ . This results in:

$$\Phi(x) = \frac{2k_{\text{B}} T}{q} \ln \left[\sec \left(C - \frac{x}{\sqrt{2} L_d} \right) \right], \quad (\text{A.12})$$

where $C = \cos^{-1}[\exp(-q\Phi_s/2k_{\text{B}}T)]$. Using the condition that $\Phi = 0$ when $x = x_{\text{acc}}$ in Equation A.12 allows the accumulation layer thickness to be written as $x_{\text{acc}} = \sqrt{2}L_d C$. As Φ_s increases, C tends to a constant ($\pi/2$), and the accumulation layer thickness reaches a maximum value of $x_{\text{acc}}^{\max} = \pi L_d / \sqrt{2} = 180 \text{ nm}$.

The electron distribution can therefore be calculated from $\Phi(x)$ using

$$N = N_D \exp \left(\frac{q\Phi(x)}{k_{\text{B}} T} \right), \quad (\text{A.13})$$

where the only parameter still unknown is Φ_s . This can be determined from the applied gate voltage V_g , which is related to the potential drop across the gate insulator V_{ox} by $V_g = \Phi_s + V_{\text{ox}}$, and the total charge stored by the dielectric per unit area $Q_{\text{acc}} = C_{\text{ox}} V_{\text{ox}}$. The capacitance per unit area of the insulator $C_{\text{ox}} = \epsilon_{\text{ox}} \epsilon_0 / \delta_{\text{ox}} = 1.73 \text{ F m}^{-2}$ for a

200 nm-thick silicon dioxide ($\epsilon_{\text{ox}} = 3.9$) layer. Q_{acc} can be obtained by integrating ρ :

$$\begin{aligned} Q_{\text{acc}} &= \int_0^\infty \rho(x)dx = \epsilon_{\text{Si}}\epsilon_0 E(0) \\ &= -\epsilon_{\text{Si}}\epsilon_0 \frac{\sqrt{2} k_{\text{B}}T}{L_d} \frac{q}{q} \sqrt{\exp\left(\frac{q\Phi_s}{k_{\text{B}}T}\right) - 1}. \end{aligned} \quad (\text{A.14})$$

In the case of a small Φ_s compared with V_{ox} , which is normally satisfied at typical applied gate voltages, an analytical expression for Φ_s can be obtained from $V_g = Q_{\text{acc}}/C_{\text{ox}}$ and Equation A.14:

$$\Phi_s = \frac{k_{\text{B}}T}{q} \ln \left[\left(\frac{C_{\text{ox}}}{\epsilon_{\text{Si}}\epsilon_0} \frac{L_d}{\sqrt{2} k_{\text{B}}T} V_g \right)^2 + 1 \right]. \quad (\text{A.15})$$

In general, a precise value of Φ_s can be obtained self-consistently from the estimate of Equation A.15 by requiring that $V_g = \Phi_s + V_{\text{ox}}$ match the experimentally applied gate voltage. For $V_g = -30$ V, this produces $\Phi_s = 0.24$ V and $V_{\text{ox}} = -30.24$ V, with $Q_{\text{acc}} = -5.2 \times 10^{-7}$ C m⁻², corresponding to a total electron carrier density per unit area of 3.2×10^{12} cm⁻².

Bibliography

- [1] A.G. Davies, E.H. Linfield, and M.B. Johnston. *The development of terahertz sources and their applications*. Phys. Med. Biol., 47:3679–3689, 2002. [1.1](#)
- [2] R. Köhler, A. Tredicucci, F. Beltram, H.E. Beere, E.H. Linfield, A.G. Davies, D.A. Ritchie, R.C. Iotti, and F. Rossi. *Terahertz semiconductor-heterostructure laser*. Nature, 417:156, 2002. [1.1](#), [2.2.4](#)
- [3] H.L. Hartnagel, V. Ichizli, and M. Rodriguez-Girones. *Surface/interface issues in THz electronics*. Appl. Surf. Sci., 190:428–436, 2002. [1.1](#), [3.3.2](#)
- [4] E. Mueller. *Submillimeter wave lasers*. Wiley Encyclopedia of Electrical and Electronics Engineering, 20:597–615, 1999. [1.1](#)
- [5] H.W. Hubers, S.G. Pavlov, and V.N. Shastin. *Terahertz lasers based on germanium and silicon*. Semicond. Sci. Technol., 20:S211–S221, 2005. [1.1](#)
- [6] A. Rogalski. *Infrared detectors: status and trends*. Prog. Quantum Electron., 27:59–210, 2003. [1.1](#)
- [7] Y. C. Shen, P. C. Upadhyay, E. H. Linfield, H. E. Beere, and A. G. Davies. *Ultrabroadband terahertz radiation from low-temperature-grown GaAs photoconductive emitters*. Appl. Phys. Lett., 83:3117, October 2003. [1.2](#), [2.2](#)
- [8] C. Kubler, R. Huber, S. Tubel, and A. Leitenstorfer. *Ultrabroadband detection of multi-terahertz field transients with gaseous electro-optic sensors: Approaching the near infrared*. Appl. Phys. Lett., 85:3360–3362, 2004. [1.2](#), [2.2.4](#)
- [9] C.A. Schmuttenmaer. *Exploring dynamics in the far-infrared with terahertz spectroscopy*. Chem. Rev., 104:1759–1779, 2004. [1](#), [1.3.4](#)
- [10] M. van Exter and D. Grischkowsky. *Carrier dynamics of electrons and holes in moderately doped silicon*. Phys. Rev. B, 41(17):12140–12149, 1990. [1.3.1](#), [2.4.3](#)
- [11] D. Grischkowsky, Søren Keiding, Martin van Exter, and Ch. Fattinger. *Far-infrared time-domain spectroscopy with terahertz beams of dielectrics and semiconductors*. J. Opt. Soc. Am. B, 7(10):2006, October 1990. [1.3.1](#)

- [12] T.-I Jeon, D. Grischkowsky, A. K. Mukherjee, and Reghu Menon. *Electrical characterization of conducting polypyrrole by THz time-domain spectroscopy*. Appl. Phys. Lett., 77(16):2452–2454, 2000. [1.3.1](#), [2.4.3](#)
- [13] T.-I. Jeon, Keun-Ju Kim, A.K. Mukherjee, and Reghu Menon. *Thz time domain spectroscopy of doped poly p-phenylene vinylene (meh-ppv)*. Synth. Met., 150(1):53–56, 2000. [1.3.1](#)
- [14] T.I. Jeon, K.J. Kim, C. Kang, S.J. Oh, J.H. Son, K.H. An, D.J. Bae, and Y.H. Lee. *Terahertz conductivity of anisotropic single walled carbon nanotube films*. Appl. Phys. Lett., 80:3403–3405, 2002. [1.3.1](#)
- [15] T.I. Jeon, K.J. Kim, C. Kang, I.H. Maeng, J.H. Son, K.H. An, J.Y. Lee, and Y.H. Lee. *Optical and electrical properties of preferentially anisotropic single-walled carbon-nanotube films in terahertz region*. J. Appl. Phys., 95:5736–5740, 2004. [1.3.1](#)
- [16] T.I. Jeon, J.H. Son, K.H. An, Y.H. Lee, and Y.S. Lee. *Terahertz absorption and dispersion of fluorine-doped single-walled carbon nanotube*. J. Appl. Phys., 98:034316, 2005. [1.3.1](#)
- [17] M.A. Gilmore, S. Kamal, D.M. Broun, and J.S. Dodge. *Determination of electron-phonon interaction parameters from time-domain terahertz spectroscopy*. Appl. Phys. Lett., 88:141910, 2006. [1.3.1](#), [2.4.3](#)
- [18] E. Hendry, F. Wang, J. Shan, T.F. Heinz, and M. Bonn. *Electron transport in TiO_2 probed by THz time-domain spectroscopy*. Phys. Rev. B, 69:081101, 2004. [1.3.1](#)
- [19] R. Huber, B.A. Schmid, Y.R. Shen, D.S. Chemla, and R.A. Kaindl. *Stimulated terahertz emission from intraexcitonic transitions in cu₂o*. Phys. Rev. Lett., 96:017402, 2006. [1.3.1](#)
- [20] S. Kojima, N. Tsumura, M.W. Takeda, and S. Nishizawa. *Far-infrared phonon-polariton dispersion probed by terahertz time-domain spectroscopy*. Phys. Rev. B, 67:035102, 2003. [1.3.1](#), [2.4.1](#)
- [21] J. Gomez Rivas, M. Kuttge, P. Haring Bolivar, H. Kurz, and J. A. Sanchez-Gil. *Propagation of surface plasmon polaritons on semiconductor gratings*. Phys. Rev. Lett., 93(25):256804, 2004. [1.3.1](#)
- [22] J.G. Rivas, M. Kuttge, H. Kurz, P.H. Bolivar, and J.A. Sanchez-Gil. *Low-frequency active surface plasmon optics on semiconductors*. Appl. Phys. Lett., 88:082106, 2006. [1.3.1](#)

- [23] R. Huber, C. Kubler, S. Tubel, A. Leitenstorfer, Q.T. Vu, H. Haug, F. Kohler, and M.C. Amann. *Femtosecond formation of coupled phonon-plasmon modes in InP: Ultrabroadband THz experiment and quantum kinetic theory*. Phys. Rev. Lett., 94:027401, 2005. [1.3.1](#), [2.4.3](#)
- [24] R. Huber et al. *How many-particle interactions develop after ultrafast excitation of an electron-hole plasma*. Nature, 414:286, 2001. [1.3.2](#)
- [25] A. Leitenstorfer, R. Huber, F. Tauser, A. Brodschelm, M. Bichler, and G. Abstreiter. *Femtosecond buildup of Coulomb screening in a photoexcited electron-hole plasma*. Physica B, 314:248, 2002. [1.3.2](#)
- [26] Q.T. Vu and H. Haug. *Time-dependent screening of the carrier-phonon and carrier-carrier interactions in nonequilibrium systems*. Phys. Rev. B, 62(11):7179–7185, Sep 2000. [1.3.2](#)
- [27] R.A. Kaindl, D. Hagele, M.A. Carnahan, R. Lovenich, and D.S. Chemia. *Exciton dynamics studied via internal THz transitions*. Phys. Stat. Sol. B, 238:451, 2003. [1.3.2](#)
- [28] R.A. Kaindl, M.A. Carnahan, D. Hagele, R. Lovenich, and D.S. Chemia. *Ultrafast terahertz probes of transient conducting and insulating phases in an electron-hole gas*. Nature, 423:734, 2003. [1.3.2](#)
- [29] C. Kittel. *Introduction to Solid State Physics*, chapter 10, pages 270–273. Wiley, 1996. [2](#), [1](#)
- [30] M. C. Nuss, K. W. Goossen, J. P. Gordon, P. M. Mankiewich, M. L. O’Malley, and M. Bhushan. *Terahertz time-domain measurement of the conductivity and superconducting band gap in niobium*. J. Appl. Phys., 70:2238, 1991. [1.3.2](#)
- [31] R. Kaindl et al. *Far-infrared optical conductivity gap in superconducting MgB₂ films*. Phys. Rev. Lett., 88:027003, 2002. [1.3.2](#)
- [32] F. Gao et al. *Terahertz transmission of a Ba_{1-x}K_xBiO₃ film probed by coherent time-domain spectroscopy*. Physical Review B, 52:3607, 1995. [1.3.2](#)
- [33] M.C. Nuss and J. Orenstein. *Millimeter and submillimeter wave spectroscopy of solids*, chapter 2, pages 7–50. Springer, 1998. [1.3.2](#), [1.3.4](#), [4.2](#)
- [34] J.F. Federici et al. *Direct picosecond measurement of photoinduced Cooper-pair breaking in lead*. Phys. Rev. B, 46:11153, 1992. [1.3.2](#)
- [35] R.D. Averitt. Far-infrared carrier dynamics in superconducting MgB₂. In R.D. Miller, editor, *Ultrafast Phenomena XIII*, page 319. Springer, 2003. [1.3.2](#)

- [36] R.A. Kaindl, M.A. Carnahan, D.S. Chemla, S. Oh, and J.N. Eckstein. *Dynamics of cooper pair formation in bi2sr2cacu2o8+delta*. Phys. Rev. B, 72:060510, 2005. [1.3.2](#), [3.3.3](#)
- [37] E. Hendry, J.M. Schins, L. P. Candeias, L. D. A. Siebbeles, and M. Bonn. *Efficiency of exciton and charge carrier photogeneration in a semiconducting polymer*. Phys. Rev. Lett., 92(19):196601, 2004. [1.3.2](#)
- [38] E. Hendry, M. Koeberg, J. M. Schins, H. K. Nienhuys, V. Sundstrom, L. D. A. Siebbeles, and M. Bonn. *Interchain effects in the ultrafast photophysics of a semiconducting polymer: THz time-domain spectroscopy of thin films and isolated chains in solution*. Phys. Rev. B, 71(12):125201, 2005. [1.3.2](#)
- [39] O. Ostroverkhova, D.G. Cooke, S. Shcherbyna, R.F. Egerton, F.A. Hegmann, R.R. Tykwiński, and J.E. Anthony. *Bandlike transport in pentacene and functionalized pentacene thin films revealed by subpicosecond transient photoconductivity measurements*. Phys. Rev. B, 71:035204, 2005. [1.3.2](#), [3.3.3](#)
- [40] O. Ostroverkhova, S. Shcherbyna, D.G. Cooke, R.F. Egerton, F.A. Hegmann, R.R. Tykwiński, S.R. Parkin, and J.E. Anthony. *Optical and transient photoconductive properties of pentacene and functionalized pentacene thin films: Dependence on film morphology*. J. Appl. Phys., 98:033701, 2005. [1.3.2](#)
- [41] O. Ostroverkhova, D.G. Cooke, F.A. Hegmann, J.E. Anthony, V. Podzorov, M.E. Gershenson, O.D. Jurchescu, and T.T.M. Palstra. *Ultrafast carrier dynamics in pentacene, functionalized pentacene, tetracene, and rubrene single crystals*. Appl. Phys. Lett., 88:162101, 2006. [1.3.2](#)
- [42] M.C. Beard, G.M. Turner, J.E. Murphy, O.I. Micic, M.C. Hanna, A.J. Nozik, and C.A. Schmuttenmaer. *Electronic coupling in InP nanoparticle arrays*. Nano Lett., 3:1695–1699, 2003. [1.3.2](#)
- [43] D.G. Cooke, A.N. MacDonald, A. Hryciw, J. Wang, Q. Li, A. Meldrum, and F.A. Hegmann. *Transient terahertz conductivity in photoexcited silicon nanocrystal films*. Phys. Rev. B, 73:193311, 2006. [1.3.2](#)
- [44] M.C. Beard, G.M. Turner, and C.A. Schmuttenmaer. *Size-dependent photoconductivity in CdSe nanoparticles as measured by time-resolved terahertz spectroscopy*. Nano Lett., 2:983–987, 2002. [1.3.2](#)
- [45] E. Hendry, M. Koeberg, F. Wang, H. Zhang, C.D. Donega, D. Vanmaekelbergh, and M. Bonn. *Direct observation of electron-to-hole energy transfer in CdSe quantum dots*. Phys. Rev. Lett., 96:057408, 2006. [1.3.2](#)

- [46] D.G. Cooke, F.A. Hegmann, Y.I. Mazur, W.Q. Ma, X. Wang, Z.M. Wang, G.J. Salamo, M. Xiao, T.D. Mishima, and M.B. Johnson. *Anisotropic photoconductivity of InGaAs quantum dot chains measured by terahertz pulse spectroscopy*. Appl. Phys. Lett., 85:3839–3841, 2004. [1.3.2](#), [3.3.3](#)
- [47] R.P. Prasankumar, A. Scopatz, D.J. Hilton, A.J. Taylor, R.D. Averitt, J.M. Zide, and A.C. Gossard. *Carrier dynamics in self-assembled ErAs nanoislands embedded in GaAs measured by optical-pump terahertz-probe spectroscopy*. Appl. Phys. Lett., 86(20):201107, 2005. [1.3.2](#), [6.1](#)
- [48] X.L. Xu, L. Song, Y.L. Shi, Y.P. Yang, S.S. Xie, and W. Li. *Light-induced dielectric transparency in single-walled carbon nanotube films*. Chem. Phys. Lett., 410:298–301, 2005. [1.3.2](#)
- [49] D.D. Arnone. *Applications of terahertz technology to medical imaging*. Proc. SPIE Terahertz Spectroscopy Applicat. II, 3823:209, 1999. [1.3.3](#)
- [50] G.M. Turner M.C. Beard and C.A. Schmuttenmaer. *Progress towards two-dimensional biomedical imaging with THz spectroscopy*. Phys. Med. Biol., 47:3481, 2002. [1.3.3](#)
- [51] As being developed by Teraview Ltd. <http://www.teraview.co.uk>. [1.3.3](#)
- [52] D.M. Mittleman, R.H. Jacobsen, and M.C. Nuss. *T-ray imaging*. IEEE Journal of Selected Topics in Quantum Electronics, 2:679, 1996. [1.3.3](#)
- [53] D.M. Mittleman, S. Hunsche, L. Boivin, and M.C. Nuss. *T-ray tomography*. Opt. Lett., 22:904, 1997. [1.3.3](#)
- [54] O. Mitrofanov, M. Lee, J.W.P. Hsu, I. Brener, R. Harel, J.F. Federici, J.D. Wynn, L.N. Pfeiffer, and K.W. West. *Collection-mode near-field imaging with 0.5 THz pulses*. IEEE Journal on Selected Topics in Quantum Electronics, 7:600, 2001. [1.3.3](#)
- [55] J.F. Federici and O. Mitrofanov. *Terahertz near-field imaging*. Phys. Med. Biol., 47:3727, 2002. [1.3.3](#)
- [56] H.-T. Chen, R. Kersting, and G.C. Cho. *Terahertz imaging with nanometer resolution*. Appl. Phys. Lett., 83:3009, 2003. [1.3.3](#)
- [57] F. Buersgens, R. Kersting, and H.T. Chen. *Terahertz microscopy of charge carriers in semiconductors*. Appl. Phys. Lett., 88:112115, 2006. [1.3.3](#)
- [58] J. Shan, A. Nahata, and T.F. Heinz. *Terahertz time-domain spectroscopy based on nonlinear optics*. Journal of Nonlinear Optical Physics & Materials, 11:31, 2002. [1.3.4](#), [2.2.2](#)

- [59] M. Tani, M. Herrman, and K. Sakai. *Generation and detection of terahertz pulsed radiation with photoconductive antennas and its application to imaging*. Meas. Sci. Technol., 13:1739, 2002. [1.3.4](#)
- [60] M.C. Beard, G.M. Turner, and C.A. Schmuttenmaer. *Terahertz spectroscopy*. J. Phys. Chem. B, 106:7146, 2002. [1.3.4](#)
- [61] C. F. Klingshirn. *Semiconductor Optics*. Springer, 1st edition, 1997. [2.1.1](#), [2.1.1](#)
- [62] C. Spielmann, P.F. Curley, T. Brabec, and F. Krausz. *Ultrabroadband femtosecond lasers*. IEEE J. Quantum Electron., 30:1100–1114, 1994. [2.2.1](#)
- [63] A. Stingl, M. Lenzner, C. Spielmann, F. Krausz, and R. Szipocs. *Sub-10-fs mirror-dispersion-controlled ti-sapphire laser*. Opt. Lett., 20:602–604, 1995. [2.2.1](#), [2.2.1](#)
- [64] T. Loffler, M. Kress, M. Thomson, T. Hahn, N. Hasegawa, and H.G. Roskos. *Comparative performance of terahertz emitters in amplifier-laser-based systems*. Semicond. Sci. Technol., 20:S134–S141, 2005. [2.2.2](#)
- [65] B.B. Hu, X.C. Zhang, D.H. Auston, and P.R. Smith. *Free-space radiation from electro-optic crystals*. Appl. Phys. Lett., 56:506–508, 1990. [2.2.2](#)
- [66] R. Huber et al. *Generation and field-resolved detection of femtosecond electromagnetic pulses tunable up to 41 THz*. App. Phys. Lett., 76:3191, 2000. [2.2.2](#)
- [67] E. Castro-Camus, J. Lloyd-Hughes, and M. B. Johnston. *Three-dimensional carrier-dynamics simulation of terahertz emission from photoconductive switches*. Phys. Rev. B, 71:195301, 2005. [2.3](#), [4.2.1](#), [4.2.2](#)
- [68] M. B. Johnston, D. M. Whittaker, A. Corchia, A. G Davies, and E. H. Linfield. *Simulation of terahertz generation at semiconductor surfaces*. Phys. Rev. B, 65(16):165301, March 2002. [2.3](#), [2.2.2](#), [4.2.1](#), [4.2.2](#), [4.3](#), [4.3](#), [4.4.2](#)
- [69] X.C. Zhang, J.T. Darrow, B.B. Hu, D.H. Auston, M.T. Schmidt, P. Tham, and E.S. Yang. *Optically induced electromagnetic-radiation from semiconductor surfaces*. Appl. Phys. Lett., 56:2228–2230, 1990. [2.2.2](#)
- [70] D.H. Auston. *Picosecond optoelectronic switching and gating in silicon*. Appl. Phys. Lett., 26:101, 1975. [2.2.2](#)
- [71] E. Castro-Camus, J. Lloyd-Hughes, M. B. Johnston, M. D. Fraser, H. H. Tan, and C. Jagadish. *Polarization-sensitive terahertz detection by multicontact photoconductive receivers*. Appl. Phys. Lett., 86:254102, June 2005. [2.2.3](#), [4.4](#), [6.1](#)
- [72] Q. Wu and X.C. Zhang. *Free-space electro-optic sampling of terahertz beams*. Appl. Phys. Lett., 67:3523–3525, 1995. [2.2.3](#)

- [73] A. Leitenstorfer, S. Hunsche, J. Shah, M.C. Nuss, and W.H. Knox. *Detectors and sources for ultrabroadband electro-optic sampling: Experiment and theory*. Appl. Phys. Lett., 74:1516, 1999. [2.2.3](#), [2.2.4](#)
- [74] M. Fox. *Optical Properties of Solids*. Oxford University Press, 1st edition, 2001. [2.2.3](#), [5.1.1](#)
- [75] G. Zhao, R. N. Schouten, N. van der Valk, W. Th. Wenckebach, and P. C. M. Planken. *Design and performance of a THz emission and detection setup based on a semi-insulating GaAs emitter*. Review of Scientific Instruments, 73(4):1715–1719, 2002. [2.2.3](#), [4.5](#)
- [76] A. Bartels, A. Thoma, C. Janke, T. Dekorsy, A. Dreyhaupt, S. Winnerl, and M. Helm. *High-resolution thz spectrometer with khz scan rates*. Opt. Express, 14:430–437, 2006. [2.2.3](#), [2.4.2](#)
- [77] M. Hangyo, T. Nagashima, and S. Nashima. *Spectroscopy by pulsed terahertz radiation*. Measurement Science and Technology, 13(11):1727–1738, 2002. [2.3](#)
- [78] E. Hecht. *Optics*, chapter 4, page 112. Addison Wesley, 1998. [2.3](#)
- [79] L. Duvillaret, F. Garet, and J.L. Coutaz. *Highly precise determination of optical constants and sample thickness in terahertz time-domain spectroscopy*. Appl. Optics, 38:409–415, 1999. [2.3](#)
- [80] L. Duvillaret, F. Garet, and J.L. Coutaz. *A reliable method for extraction of material parameters in terahertz time-domain spectroscopy*. IEEE J. Select. Topics Quantum Electron., 2:739–746, 1996. [2.3](#)
- [81] T.D. Dorney, R.G. Baraniuk, and D.M. Mittleman. *Material parameter estimation with terahertz time-domain spectroscopy*. J. Opt. Soc. Am. A-Opt. Image Sci. Vis., 18:1562–1571, 2001. [2.3](#)
- [82] P. Y. Yu and M. Cardona. *Fundamentals of Semiconductors*. Springer, 3rd edition, 2003. [2.4.1](#), [2.4.1](#), [2.4.1](#), [2.4.3](#), [3.1.2](#), [3.3.1](#), [3.3.3](#)
- [83] C. H. Henry and J. J. Hopfield. *Raman scattering by polaritons*. Phys. Rev. Lett., 15(25):964–966, Dec 1965. [2.4.1](#), [2.4.1](#)
- [84] N.S. Stoyanov, D.W. Ward, T. Feurer, and K.A. Nelson. *Terahertz polariton propagation in patterned materials*. Nat. Mater., 1:95–98, 2002. [2.4.1](#)
- [85] M. van Exter, C. Fattinger, and D. Grischkowsky. *Terahertz time-domain spectroscopy of water vapour*. Opt. Lett., 14(20):1128, October 1989. [2.4.2](#), [2.7](#)
- [86] W. Zhang, Abul K. Azad, and D. Grischkowsky. *Terahertz studies of carrier dynamics and dielectric response of n-type, freestanding epitaxial gan*. Appl. Phys. Lett., 82(17):2841–2843, 2003. [2.4.3](#)

- [87] M.C. Beard, G.M. Turner, and C.A. Schmuttenmaer. *Subpicosecond carrier dynamics in low-temperature grown GaAs as measured by time-resolved terahertz spectroscopy*. J. Appl. Phys., 90(12):5915–5923, 2001. [2.4.3](#)
- [88] R. Huber, F. Tauser, A. Brodschelm, M. Bichler, G. Abstreiter, and A. Leitenstorfer. *How many-particle interactions develop after ultrafast excitation of an electron-hole plasma*. Nature, 414:286, 2001. [2.4.3](#)
- [89] T.-R. Tsai, C.-C. Chi, and S.-F. Horng. *Terahertz responses of high-resistivity *ybc* thin films*. Physica C, 391:281, September 2003. [2.4.3](#)
- [90] W.W.M. Allison, V. Blackmore, G. Doucas, B. Ottewell, C. Perry, P. G. Huggard, J. Lloyd Hughes, E. Castro-Camus, M. B. Johnston, M.F. Kimmitt, B. Redlich, and A. van der Meer. *Longitudinal electron bunch profile diagnostics at 45-50mev using coherent smith-purcell radiation*. Unpublished, 2006. [2.4.4](#)
- [91] C. Winnewisser, F. Lewen, J. Weinzierl, and H. Helm. *Transmission features of frequency-selective components in the far infrared determined by terahertz time-domain spectroscopy*. Appl. Optics, 38:3961–3967, 1999. [2.4.4](#)
- [92] Wen-Chung Chen and C. S. Chang. *Structures and defects in arsenic-ion-implanted GaAs films annealed at high temperatures*. J. Appl. Phys., 81(11):7295, 1997. [3.1](#), [3.1.3](#), [4.4.2](#)
- [93] D.D. Nolte. *Semi-insulating semiconductor heterostructures: Optoelectronic properties and applications*. J. Appl. Phys., 85:6259–6289, 1999. [3.1.1](#)
- [94] I.S. Gregory, C. Baker, W.R. Tribe, M.J. Evans, H.E. Beere, E.H. Linfield, A.G. Davies, and M. Missous. *High resistivity annealed low-temperature GaAs with 100 fs lifetimes*. Appl. Phys. Lett., 83:4199–4201, 2003. [3.1.2](#), [3.2.3](#)
- [95] A. Krotkus, S. Marcinkevicius, J. Jasinski, M. Kaminska, H. H. Tan, and C. Jagadish. *Picosecond carrier lifetime in GaAs implanted with high doses of As ions: An alternative material to low-temperature GaAs for optoelectronic applications*. Appl. Phys. Lett., 66(24):3304, 1995. [3.1.3](#), [3.1.3](#), [4.4.3](#)
- [96] C. Carmody, H. H. Tan, C. Jagadish, A. Gaarder, and S. Marcinkevicius. *Ion-implanted In_{0.53}Ga_{0.47}As for ultrafast optoelectronic applications*. Appl. Phys. Lett., 82(22):3913–3915, 2003. [3.1.3](#), [4.5](#)
- [97] C. Carmody, H. H. Tan, C. Jagadish, A. Gaarder, and S. Marcinkevicius. *Ultrafast carrier trapping and recombination in highly resistive ion implanted inp*. J. Appl. Phys., 94(2):1074–1078, 2003. [3.1.3](#), [3.5](#), [3.5.1](#)
- [98] R. Williams. *Modern GaAs Processing Methods*. Artech House, 2nd edition, 1990. [3.1.3](#)

- [99] J. F. Ziegler and J. P. Biersack. SRIM 2003 software. Available online at <http://www.srim.org>. [3.2](#), [3.1.3](#), [3.5](#), [4.4.2](#)
- [100] S. Marcinkevicius, C. Jagadish, H. H. Tan, M. Kaminska, K. Korona, R. Adomavicius, and A. Krotkus. *Influence of annealing on carrier dynamics in as ion-implanted epitaxially lifted-off GaAs layers*. Appl. Phys. Lett., 76(10):1306–1308, 2000. [3.1.3](#), [4.4.3](#)
- [101] G. R. Lin, W. C. Chen, C. S. Chang, S. C. Chao, K. H. Wu, T. M. Hsu, W. C. Lee, and C. L. Pan. *Material and ultrafast optoelectronic properties of furnace-annealed arsenic-ion-implanted GaAs*. IEEE J. Quantum Electron., 34(9):1740–1748, September 1998. [3.1.3](#)
- [102] W. Shockley and W. T. Read. *Statistics of the recombinations of holes and electrons*. Phys. Rev., 87(5):835–842, Sep 1952. [3.1.4](#)
- [103] S.S. Prabhu, S.E. Ralph, M.R. Melloch, and E.S. Harmon. *Carrier dynamics of low-temperature-grown GaAs observed via THz spectroscopy*. Appl. Phys. Lett., 70:2419–2421, 1997. [3.1.4](#)
- [104] H. Nemec, A. Pashkin, P. Kuzel, M. Khazan, S. Schnull, and I. Wilke. *Carrier dynamics in low-temperature grown GaAs studied by terahertz emission spectroscopy*. J. Appl. Phys., 90:1303–1306, 2001. [3.1.4](#)
- [105] I. S. Gregory. *The Development of a Continuous-Wave Terahertz Imaging System*. PhD thesis, University of Cambridge, 2004. [3.1.4](#), [3.2.3](#)
- [106] J. Shah. *Ultrafast Spectroscopy of Semiconductors and Semiconductor Nanostructures*. Springer, 1st edition, 1996. [3.2.3](#)
- [107] Bernard Valeur. *Molecular Fluorescence - Principles and Applications*. Wiley-VCH, 1st edition, 2002. [3.2.3](#)
- [108] M.H. Chang, F.J.M. Hoeben, P. Jonkheijm, A.P.H.J. Schenning, E.W. Meijer, C. Silva, and L.M. Herz. *Influence of mesoscopic ordering on the photoexcitation transfer dynamics in supramolecular assemblies of oligo-p-phenylenevinylene*. Chem. Phys. Lett., 418:196–201, 2006. [3.2.3](#)
- [109] S.S. Prabhu and A.S. Vengurlekar. *Dynamics of the pump-probe reflectivity spectra in GaAs and gan*. J. Appl. Phys., 95:7803–7812, 2004. [3.2.3](#)
- [110] B.R. Bennett, R.A. Soref, and J.A. Del Alamo. *Carrier-induced change in refractive index of inp, GaAs and ingaasp*. IEEE J. Quantum Electron., 26:113–122, 1990. [3.2.3](#)

- [111] J. A. Kash, J. C. Tsang, and J. M. Hvam. *Subpicosecond time-resolved raman spectroscopy of lo phonons in gaas.* Phys. Rev. Lett., 54(19):2151–2154, May 1985. [3.2.3](#), [3.3.1](#), [3.3.1](#)
- [112] M. C. Nuss, D. H. Auston, and F. Capasso. *Direct subpicosecond measurement of carrier mobility of photoexcited electrons in gallium arsenide.* Phys. Rev. Lett., 58(22):2355–2358, 1987. [3.3.1](#)
- [113] C.J. Sandroff, R.N. Nottenburg, J.C. Bischoff, and R. Bhat. *Dramatic enhancement in the gain of a GaAs/AlGaAs heterostructure bipolar-transistor by surface chemical passivation.* Appl. Phys. Lett., 51:33–35, 1987. [3.3.2](#), [3.3.2](#)
- [114] E. Yablonovitch, C.J. Sandroff, R. Bhat, and T. Gmitter. *Nearly ideal electronic-properties of sulfide coated GaAs-surfaces.* Appl. Phys. Lett., 51:439–441, 1987. [3.3.2](#), [3.3.2](#)
- [115] S. Kamiyama, Y. Mori, Y. Takahashi, and K. Ohnaka. *Improvement of catastrophic optical-damage level of AlGaInP visible laser-diodes by sulfur treatment.* Appl. Phys. Lett., 58:2595–2597, 1991. [3.3.2](#)
- [116] M.G. Mauk, S. Xu, D.J. Arent, R.P. Mertens, and G. Borghs. *Study of novel chemical surface passivation techniques on GaAs pn junction solar-cells.* Appl. Phys. Lett., 54:213–215, 1989. [3.3.2](#)
- [117] M.C. Beard, G.M. Turner, and C.A. Schmuttenmaer. *Transient photoconductivity in GaAs as measured by time-resolved terahertz spectroscopy.* Phys. Rev. B, 62:15764–15777, 2000. [3.3.2](#)
- [118] NSM semiconductor archive, <http://www.ioffe.rssi.ru/sva/nsm/semicond/>. [3.3.3](#), [4.1](#)
- [119] H. Ehrenreich. *Screening effects in polar semiconductors.* J. Phys. Chem. Solids, 8:130, January 1959. [3.3.3](#)
- [120] J. Lloyd-Hughes, E. Castro-Camus, and M. B. Johnston. *Simulation and optimisation of terahertz emission from InGaAs and InP photoconductive switches.* Sol. Stat. Comm., 136(11-12):595, December 2005. [4.2.2](#)
- [121] J. Lloyd-Hughes, E. Castro-Camus, M. D. Fraser, C. Jagadish, and M. B. Johnston. *Carrier dynamics in ion-implanted GaAs studied by simulation and observation of terahertz emission.* Phys. Rev. B, 70:235330, December 2004. [4.2.2](#), [4](#)
- [122] M. B. Johnston, A. Dowd, R. Driver, A. G. Davies, and E. H. Linfield amd D. M. Whittaker. *Emission of collimated THz pulses from photo-excited semiconductors.* Semicond. Sci. Technol., 19:S449–S451, April 2004. [4.2.2](#)

- [123] P.C. Upadhyay, W.-H. Fan, A. Burnett, J. Cunningham, A.G. Davies, E.H. Linfield, J. Lloyd-Hughes, E. Castro-Camus, M.B. Johnston, and H. Beere. *Optimization of broadband terahertz ($> 6.0 \text{ THz}$) generation in asymmetrically-excited photoconductive antenna structures*. Unpublished, 2006. [4.2.2](#)
- [124] I. Vurgaftman, J. R. Meyer, and L. R. Ram-Mohan. *Band parameters for III-V compound semiconductors and their alloys*. Journal of Applied Physics, 89(11):5815–5875, 2001. [4.1](#)
- [125] J. Groenen, R. Carles, G. Landa, C. Guerret-Picourt, C. Fontaine, and M. Gendry. *Optical-phonon behavior in $\text{Ga}_{1-x}\text{In}_x\text{As}$: The role of microscopic strains and ionic plasmon coupling*. Phys. Rev. B, 58(16):10452–10462, 1998. [4.1](#)
- [126] S. Zollner, S. Gopalan, and M. Cardona. *Microscopic theory of intervalley scattering in GaAs: k dependence of deformation potentials and scattering rates*. J. Appl. Phys., 68(4):1682, 1990. [4.1](#)
- [127] P. Gu, M. Tani, S. Kono, K. Sakai, and X.C. Zhang. *Study of terahertz radiation from inas and insb*. J. Appl. Phys., 91:5533–5537, 2002. [4.3](#), [4.6.1](#)
- [128] Y. C. Shen, P. C. Upadhyay, E. H. Linfield, H. E. Beere, and A. G. Davies. *Terahertz generation from coherent optical phonons in a biased GaAs photoconductive emitter*. Phys. Rev. B, 69(23):235325, 2004. [4.3](#)
- [129] G. R. Lin and C. L. Pan. *Characterization of optically excited terahertz radiation from arsenic-ion-implanted GaAs*. Appl. Phys. B: Lasers Opt., 72:151, 2001. [4.4](#)
- [130] Tze-An Liu, Masahiko Tani, and Ci-Ling Pan. *THz radiation emission properties of multienergy arsenic-ion-implanted GaAs and semi-insulating GaAs based photoconductive antennas*. J. Appl. Phys., 93(5):2996, 2003. [4.4](#)
- [131] Tze-An Liu, Masahiko Tani, Makoto Nakajima, Masanori Hangyo, and Ci-Ling Pan. *Ultrabroadband terahertz field detection by photoconductive antennas based on multi-energy arsenic-ion-implanted GaAs and semi-insulating GaAs*. Appl. Phys. Lett., 83(7):1322–1324, 2003. [4.4](#)
- [132] E. Castro-Camus, J. Lloyd-Hughes, M. D. Fraser, H. H. Tan, C. Jagadish, and M. B. Johnston. Detecting the full polarization state of terahertz transients. volume 6120, page 61200Q. SPIE, 2006. [4.4](#)
- [133] M. Kaminska, E. R. Weber, and C. Jagadish. *Defects in non-stoichiometric III-IV compounds*. Proceedings of the 8th Conference on Semi-insulating III-IV Materials, June 1994. [4.4.2](#)
- [134] B. K. Ridley. *Quantum Processes in Semiconductors*, chapter 4.3. Clarendon Press, Oxford, 1999. [4.4.2](#)

- [135] L. Giniunas, R. Danielius, H. H. Tan, C. Jagadish, R. Adomavicius, and A. Krotkus. *Electron and trap dynamics in as-ion-implanted and annealed GaAs*. Appl. Phys. Lett., 78(12):1667–1669, 2001. [4.4.3](#)
- [136] G. Gallot, Jiangquan Zhang, R. W. McGowan, Tae-In Jeon, and D. Grischkowsky. *Measurements of the THz absorption and dispersion of ZnTe and their relevance to the electro-optic detection of THz radiation*. Appl. Phys. Lett., 74(23):3450, 1999. [4.4.4](#)
- [137] G. Gallot and D. Grischkowsky. *Electro-optic detection of terahertz radiation*. J. Opt. Soc. Am. B, 16(8):1204, August 1999. [4.4.4](#)
- [138] D. Côté, J. E. Sipe, and H. M. van Driel. *Simple method for calculating the propagation of terahertz radiation in experimental geometries*. J. Opt. Soc. Am. B, 20(6):1374, June 2003. [4.4.4](#)
- [139] A. Hussain and S.R. Andrews. *Dynamic range of ultrabroadband terahertz detection using GaAs photoconductors*. Appl. Phys. Lett., 88:143514, 2006. [4.5](#)
- [140] J. Bromage, I.A. Walmsley, and C.R. Stroud. *Dithered-edge sampling of terahertz pulses*. Appl. Phys. Lett., 75:2181–2183, 1999. [4.5](#)
- [141] C.K. Chiang, C.R. Fincher, Y.W. Park, A.J. Heeger, H. Shirakawa, E.J. Louis, S.C. Gau, and A.G. MacDiarmid. *Electrical conductivity in doped polyacetylene*. Phys. Rev. Lett., 39(17):1098–1101, Oct 1977. [5.1](#), [5.1.1](#), [5.1.1](#)
- [142] J.H. Burroughes, D.D.C. Bradley, A.R. Brown, R.N. Marks, K. Mackay, R.H. Friend, P.L. Burns, and A.B. Holmes. *Light-emitting-diodes based on conjugated polymers*. Nature, 347:539–541, 1990. [5.1](#)
- [143] F. Garnier, R. Hajlaoui, A. Yassar, and P. Srivastava. *All-polymer field-effect transistor realized by printing techniques*. Science, 265:1684–1686, 1994. [5.1](#), [5.1.2](#)
- [144] As being developed by companies such as Philips, Seiko-Epson, Cambridge Design Technology and PlasticLogic. [5.1](#)
- [145] M. Bernius, M. Inbasekaran, E. Woo, W.S. Wu, and L. Wujkowski. *Fluorene-based polymers-preparation and applications*. J. Mater. Sci.-Mater. Electron., 11:111–116, 2000. [5.1.1](#)
- [146] L.L. Chua, J. Zaumseil, J.F. Chang, E.C.W. Ou, P.K.H. Ho, H. Sirringhaus, and R.H. Friend. *General observation of n-type field-effect behaviour in organic semiconductors*. Nature, 434(7030):194, 2005. [5.1.1](#), [5.1.2](#)

- [147] C. Silva, A.S. Dhoot, D.M. Russell, M.A. Stevens, A.C. Arias, J.D. MacKenzie, N.C. Greenham, R.H. Friend, S. Setayesh, and K. Mullen. *Efficient exciton dissociation via two-step photoexcitation in polymeric semiconductors.* Phys. Rev. B, 6412:125211, 2001. [2](#)
- [148] K. Lee, S. Cho, S. Heum Park, A.J. Heeger, C.-W. Lee, and S.-H. Lee. *Metallic transport in polyaniline.* Nature, 441:65–68, 2006. [5.1.1](#)
- [149] G. Horowitz. *Organic field-effect transistors.* Adv. Mat., 10:365–377, 1998. [5.1.2](#)
- [150] H. Sirringhaus. *Device physics of solution-processed organic field-effect transistors.* Adv. Mat., 17(20):2411, 2005. [5.1.2](#), [5.1.3](#)
- [151] A. Salleo, M.L. Chabinyc, M.S. Yang, and R.A. Street. *Polymer thin-film transistors with chemically modified dielectric interfaces.* Appl. Phys. Lett., 81:4383–4385, 2002. [5.1.3](#)
- [152] A. Salleo and R.A. Street. *Light-induced bias stress reversal in polyfluorene thin-film transistors.* J. Appl. Phys., 94:471–479, 2003. [5.1.3](#), [5.5](#)
- [153] R.A. Street, A. Salleo, and M.L. Chabinyc. *Bipolaron mechanism for bias-stress effects in polymer transistors.* Phys. Rev. B, 68:085316, 2003. [5.1.3](#), [5.4](#)
- [154] A. Salleo and R.A. Street. *Kinetics of bias stress and bipolaron formation in polythiophene.* Phys. Rev. B, 70:235324, 2004. [5.1.3](#), [5.4](#)
- [155] A. Salleo, F. Endicott, and R.A. Street. *Reversible and irreversible trapping at room temperature in poly(thiophene) thin-film transistors.* Appl. Phys. Lett., 86:263505, 2005. [5.1.3](#), [5.5](#)
- [156] K.P. Pernstich, S. Haas, D. Oberhoff, C. Goldmann, D.J. Gundlach, B. Batlogg, A.N. Rashid, and G. Schitter. *Threshold voltage shift in organic field effect transistors by dipole monolayers on the gate insulator.* J. Appl. Phys., 96:6431–6438, 2004. [5.1.3](#)
- [157] R. Schmeichel and H. von Seggern. *Electronic traps in organic transport layers.* Phys. Status Solidi A-Appl. Res., 201:1215–1235, 2004. [5.1.3](#), [5.5.2](#)
- [158] V.I. Arkhipov, E.V. Emelianova, S. Barth, and H. Bassler. *Ultrafast on-chain dissociation of hot excitons in conjugated polymers.* Phys. Rev. B, 61:8207–8214, 2000. [3](#), [5.5.2](#)
- [159] V.R. Nikitenko, D. Hertel, and H. Bassler. *Dispersive geminate recombination in a conjugated polymer.* Chem. Phys. Lett., 348:89–94, 2001. [3](#), [5.5.2](#)
- [160] L. Burgi, T.J. Richards, R.H. Friend, and H. Sirringhaus. *Close look at charge carrier injection in polymer field-effect transistors.* J. Appl. Phys., 94:6129–6137, 2003. [5.1.4](#), [5.1.4](#)

- [161] L. Burgi, H. Sirringhaus, and R.H. Friend. *Noncontact potentiometry of polymer field-effect transistors.* Appl. Phys. Lett., 80:2913–2915, 2002. [5.1.4](#)
- [162] V. Palermo, M. Palma, and P. Samori. *Electronic characterization of organic thin films by kelvin probe force microscopy.* Adv. Mater., 18:145–164, 2006. [5.1.4](#)
- [163] L. Burgi, T. Richards, M. Chiesa, R.H. Friend, and H. Sirringhaus. *A microscopic view of charge transport in polymer transistors.* Synth. Met., 146(3):297–309, November 2004. [5.1.4](#), [5.5](#)
- [164] This will be discussed in detail in a forthcoming paper by the Cambridge group. [5.1.4](#)
- [165] K. E. Ziemelis, A. T. Hussain, D. D. C. Bradley, R. H. Friend, J. Ruhe, and G. Wegner. *Optical spectroscopy of field-induced charge in poly(3-hexyl thiophene) metal-insulator-semiconductor structures: Evidence for polarons.* Phys. Rev. Lett., 66(17):2231–2234, 1991. [5.2](#)
- [166] H. C. F. Martens, O. Hilt, H. B. Brom, P. W. M. Blom, and J. N. Huiberts. *Voltage-modulated millimeter-wave spectroscopy on a polymer diode: Mesoscopic charge transport in conjugated polymers.* Phys. Rev. Lett., 87(8):086601, 2001. [5.2](#)
- [167] P.Y. Han, M. Tani, M. Usami, S. Kono, R. Kersting, and X.C. Zhang. *A direct comparison between terahertz time-domain spectroscopy and far-infrared fourier transform spectroscopy.* J. Appl. Phys., 89:2357–2359, 2001. [5.2](#)
- [168] L. Burgi, R. H. Friend, and H. Sirringhaus. *Formation of the accumulation layer in polymer field-effect transistors.* Appl. Phys. Lett., 82(9):1482–1484, 2003. [5.2.1](#)
- [169] C. Tanase, E. J. Meijer, P. W. M. Blom, and D. M. de Leeuw. *Local charge carrier mobility in disordered organic field-effect transistors.* Org. El., 4(1):33–37, 2003. [5.3](#)
- [170] M.C. Hamilton, S. Martin, and J. Kanicki. *Thin-film organic polymer phototransistors.* IEEE Trans. Electron Devices, 51:877–885, 2004. [5.5](#)
- [171] C.M. Garner, G. Kloster, G. Atwood, L. Mosley, and A.C. Palanduz. *Challenges for dielectric materials in future integrated circuit technologies.* Micro. Rel., 45(5-6):919, 2005. [5.6](#)
- [172] J. Suñé, M. Nafría, E. Miranda, X. Oriols, R. Rodríguez, and X. Aymerich. *Failure physics of ultra-thin SiO₂ gate oxides near their scaling limit.* Semicond. Sci. Technol., 15(5):445, 2000. [5.6](#)
- [173] G. D. Wilk, R. M. Wallace, and J. M. Anthony. *High-kappa gate dielectrics: Current status and materials properties considerations.* J. Appl. Phys., 89(10):5243–5275, 2001. [5.6](#)

Definition of symbols

The following is a definition of the symbols used throughout this thesis.

α	Absorption coefficient.	\tilde{n}	Complex refractive index.
B	Magnetic flux density.	n_e, n_h	Density of electrons or holes per unit area.
C_{ox}	Capacitance per unit area.	N	Concentration of electrons.
δ	Absorption depth ($= 1/\alpha$).	N_{sim}	Concentration of vacancies (simulated using SRIM).
D	Diffusion coefficient.	N_t	Concentration of traps.
D_{ij}	Intervalley deformation potential.	N_{vac}	Concentration of vacancies.
ϵ	Dielectric function.	ϕ	Phase.
E	Electric field.	Φ	Electrostatic potential.
E_γ	Incident photon energy.	r_{ij}	Fresnel reflection coefficient from medium i into j .
E_Γ	Direct Γ -valley bandgap energy.	σ	Conductivity.
E_i	Incident electric field of THz pulse.	τ	Carrier lifetime.
$E_{\text{off}}, E_{\text{on}}$	THz electric field transmitted through sample when the pump beam is off or on.	t_{ij}	Fresnel transmission coefficient from medium i into j .
E_r	Reference THz electric field.	T	Average transmitted THz electric field $= (E_{\text{off}} + E_{\text{on}})/2$.
E_s	Sample THz electric field.	ΔT	Change in electric field T of transmitted THz pulse.
E_{THz}	Terahertz electric field strength.	T_{ann}	Annealing temperature.
f, ν	Frequency.	Θ	Temperature of crystal lattice.
f_{peak}	Frequency of peak emitted THz power.	v_{th}	Thermal velocity of carriers.
FP_{ijk}	Fabry-Perot term.	V_g	Transistor gate voltage.
Γ	Scattering rate.	V_{pin}	Surface pinning potential.
J	Current density.	V_t	Threshold voltage of transistor action.
k	Wavenumber.	$\omega_{\text{TO}}, \omega_{\text{LO}}$	Angular frequency of TO- or LO-phonon mode.
k_B	Boltzmann's constant.	ω_p	Angular frequency of free-carrier plasma.
λ	Wavelength.	x_{acc}	Accumulation layer thickness.
$\Delta\lambda$	Spectral width.	Σ	Scattering cross-section.
m_e	Electron mass.		
m^*	Effective mass.		
μ	Carrier mobility.		
μ_F	Carrier field-effect mobility.		
μ_0	Permeability of free space.		